

SYNTHESIS AND CHARACTERIZATION OF BULK
AMORPHOUS/NANOCRYSTALLINE SOFT MAGNETIC MATERIALS

A THESIS SUBMITTED TO
THE GRADUATE SCHOOL OF APPLIED AND NATURAL SCIENCES
OF
MIDDLE EAST TECHNICAL UNIVERSITY

BY

MEDİHA MERVE KARATAŞ

IN PARTIAL FULFILLMENT OF THE REQUIREMENTS
FOR
THE DEGREE OF MASTER OF SCIENCE
IN
METALLURGICAL AND MATERIALS ENGINEERING

JULY 2016

Approval of the thesis:

**SYNTHESIS AND CHARACTERIZATION OF BULK
AMORPHOUS/NANOCRYSTALLINE SOFT MAGNETIC MATERIALS**

submitted by **MEDİHA MERVE KARATAŞ** in partial fulfillment of the requirements for the degree of **Master of Science in Metallurgical and Materials Engineering Department, Middle East Technical University** by,

Prof. Dr. M. Gülbin Dural Ünver _____
Dean, Graduate School of **Natural and Applied Sciences**

Prof. Dr. Cemil Hakan Gür _____
Head of Department, **Metallurgical and Materials Eng., METU**

Prof. Dr. M. Vedat Akdeniz _____
Supervisor, **Metallurgical and Materials Eng. Dept., METU**

Prof. Dr. Amdulla O. Mekhrabov _____
Co-Supervisor, **Metallurgical and Materials Eng. Dept., METU**

Examining Committee Members:

Prof. Dr. Macit Özenbaş _____
Metallurgical and Materials Engineering Dept., METU

Prof. Dr. M. Vedat Akdeniz _____
Metallurgical and Materials Engineering Dept., METU

Prof. Dr. Amdulla O. Mekhrabov _____
Metallurgical and Materials Engineering Dept., METU

Prof. Dr. Şükrü Talaş _____
Metallurgical and Materials Engineering Dept., Afyon Kocatepe University

Assist. Prof. Dr. Mert Efe _____
Metallurgical and Materials Engineering Dept., METU

Date: 28.07.2016

I hereby declare that all information in this document has been obtained and presented in accordance with academic rules and ethical conduct. I also declare that, as required by these rules and conduct, I have fully cited and referenced all material and results that are not original to this work.

Name, Last Name: Mediha Merve Karataş

Signature:

ABSTRACT

SYNTHESIS AND CHARACTERIZATION OF BULK AMORPHOUS/NANOCRYSTALLINE SOFT MAGNETIC MATERIALS

Karataş, Mediha Merve

M.Sc., Department of Metallurgical and Materials Engineering

Supervisor: Prof. Dr. M. Vedat Akdeniz

Co-Supervisor: Prof Dr. Amdulla O. Mekhrabov

July 2016, 134 pages

The aim of the study is to reach non-equilibrium cooling conditions and produce bulk glassy $(\text{Fe}_{36}\text{Co}_{36}\text{B}_{19.2}\text{Si}_{4.8}\text{Nb}_4)_{99.25}\text{Cu}_{0.75}$ rod which has a good soft magnetic property and high electrical resistivity and to investigate its crystallization kinetics.

The bulk metallic glass formation was achieved by arc melting and suction casting and it was confirmed by scanning electron microscopy (SEM), x-ray diffraction (XRD) and thermal analysis techniques. After characterizations, by isochronal and isothermal differential scanning calorimeter (DSC) analyses, crystallization kinetics of the alloy was investigated.

From isochronal DSC analyses, activation energies for glass transition and crystallization events were determined by using different analytical methods such as Kissinger and Ozawa. The critical cooling rate was calculated from two approaches called Barandiaran and Colmenero and Liu et al. and results were compared. Numerous glass forming ability parameters such as T_{rg} , ΔT_x , and γ were estimated for the samples. High majority of parameters showed that the alloy is a good bulk glass former.

The isothermal crystallization kinetics of the alloy was studied at temperatures chosen in above the first crystallization temperature. There were no crystallization signals detected in the isothermal DSC scans except for 585 °C at 5 min holding. Although SEM showed featureless matrix, α -(FeCo) crystallites were distinguished in the XRD pattern and size of these crystallites was estimated by Scherrer equation.

The magnetic and mechanical properties of the as cast and annealed alloys were compared. According to the obtained results, annealed alloys have higher saturation magnetization, lower coercive force and higher microhardness values than as cast alloys due to the presence of α -(FeCo) nanocrystalline structures within amorphous matrix.

Keywords: Bulk glassy alloy, Nanocrystallization, Soft magnetic property, High saturation magnetization

ÖZ

AMORF/NANOKRİSTAL MANYETİK MALZEMELERİN SENTEZİ VE KARAKTERİZASYONU

Karataş, Mediha Merve

Yüksek Lisans, Metalurji ve Malzeme Mühendisliği Bölümü

Tez Yöneticisi: Prof. Dr. M. Vedat Akdeniz

Ortak Tez Yöneticisi: Prof Dr. Amdulla O. Mekhrabov

Temmuz 2016, 134 sayfa

Bu çalışmanın amacı, denge olmayan soğuma şartlarına ulaşmak ve iyi bir yumuşak manyetik özelliğe ve yüksek elektriksel dirence sahip iri hacimli $(\text{Fe}_{36}\text{Co}_{36}\text{B}_{19.2}\text{Si}_{4.8}\text{Nb}_4)_{99.25}\text{Cu}_{0.75}$ camsı çubuk üretmek ve bu çubuğun kristalleşme kinetiğini incelemektir.

İri hacimli metalik cam oluşumu ark eritme ve emme döküm ile başarılmış, taramalı elektron mikroskobu, x ışınları kırınımı ve termal analiz teknikleri ile camsı yapının

varlığı kanıtlanmıştır. Bu karakterizasyonlardan sonra, alaşımın kristalleşme kinetiği eş zamanlı ve eş ısılı diferansiyel taramalı kalorimetre analizleri ile incelenmiştir.

Bu eş zamanlı termal analizlerden, Kissinger ve Ozawa gibi farklı analitik metotlar kullanılarak camsı geçiş ve kristalleşme aktivasyon enerjileri belirlenmiştir. Kritik soğuma hızı Barandiaran-Colmenero ve Liu et al. denilen iki yaklaşımla hesaplanmış ve sonuçlar karşılaştırılmıştır. T_{rg} , ΔT_x , and γ gibi çok sayıda cam oluşturma kabiliyeti parametresi hesaplanmıştır. Bu parametrelerin büyük bir kısmı alaşımın iyi bir hacimli cam oluşturduğunu göstermiştir.

Alaşımın eş ısılı kristalleşme kinetiği ilk kristalleşme sıcaklığının üstünde seçilen sıcaklıklarda çalışılmıştır. 585 °C de 5 dakika bekletme dışında yapılan tüm eş ısılı termal analizlerde kristalleşme piki gözlemlenmemiştir. Taramalı elektron mikroskobu özelliği olmayan bir matriks gösterse de, x ışınları kırınımında α -(FeCo) kristalleri fark edilip Scherrer formülü ile kristallerin boyutları hesaplanmıştır.

Alaşımın ilk döküldüğü hâli ve ısıtılmış hâlinin manyetik ve mekanik özellikleri karşılaştırılmıştır. Alınan sonuçlara göre, ısıtılmış alaşımlar α -(FeCo) nanokristal yapılarından dolayı ilk döküldüğü hâlindeki alaşımlardan daha yüksek doyum manyetizasyonuna, daha düşük koersif kuvvete ve daha yüksek mikro sertlik değerlerine sahiptir.

Anahtar Kelimeler: İri Hacimli Camsı Alaşım, Nanokristalleşme, Yumuşak Manyetik Özellik, Yüksek Doyum Manyetizasyonu

ACKNOWLEDGEMENTS

I would like to thank my supervisor Prof. Dr. M. Vedat Akdeniz and my co-supervisor Prof. Dr. Amdulla O. Mekhrabov for their support and encouragement during this study. They gave me the chance of doing independent research.

I gratefully thank my family for their support and belief in me during this study.

I would like to thank all my friends from the Novel Alloys Design and Development Laboratory (NOVALAB) for their friendships.

I would like to thank Middle East Technical University (METU) Metallurgical and Materials Engineering Department for providing facilities for my research.

TABLE OF CONTENTS

ABSTRACT	v
ÖZ	vii
ACKNOWLEDGEMENTS	ix
TABLE OF CONTENTS	xi
LIST OF TABLES	xv
LIST OF FIGURES	xvii

CHAPTERS

1. INTRODUCTION	1
2. THEORY.....	3
2.1 History of Metallic Glasses	3
2.2 Basic Concepts of Metallic Glasses.....	4
2.2.1 Glass transition.....	4
2.2.2 Glass formation.....	5
2.2.2.1 Thermodynamics of glass formation.....	5
2.2.2.2 Kinetics of glass formation.....	5
2.3 Glass Forming Ability Criteria For Bulk Metallic Glasses.....	7
2.3.1 Supercooled Liquid Region (ΔT_x).....	7
2.3.2 Reduced Glass Transition Temperature (T_{rg}).....	7
2.3.3 K_{gl} Parameter.....	8
2.3.4 S Parameter.....	8
2.3.5 ϕ Parameter.....	9
2.3.6 γ Parameter.....	9
2.3.7 γ_m Parameter.....	10

2.3.8 δ Parameter.....	10
2.3.9 α and β Parameters.....	11
2.3.10 ω Parameter.....	11
2.3.11 T_{rx} Parameter.....	12
2.3.12 New β parameter.....	12
2.3.13 r_c parameter.....	12
2.4 Production Methods of Bulk Metallic Glasses.....	13
2.4.1 Copper Mold Casting.....	13
2.4.2 Arc Melting.....	14
2.4.3 Suction Casting.....	15
2.4.4 Centrifugal Casting.....	15
2.5 Crystallization of Bulk Metallic Glasses.....	16
2.5.1 Crystallization Kinetics.....	16
2.5.1.1 Isothermal Crystallization Kinetics: JMAK Method.....	17
2.5.1.2 Non-Isothermal Crystallization Kinetics: Kissinger and Ozawa Method.....	19
2.5.2 Critical Cooling Rate Calculations.....	20
2.6 Properties and Applications of Bulk Metallic Glasses.....	22
2.6.1 Properties of BMGs.....	22
2.6.1.1 Mechanical Properties of BMGs.....	22
2.6.1.2 Magnetic Properties of BMGs.....	24
2.6.1.2.1 Hard magnetic BMGs.....	25
2.6.1.2.2 Soft magnetic BMGs.....	25
2.6.1.3 Chemical Properties of BMGs.....	29
2.6.2 Applications of BMGs.....	31
3. EXPERIMENTAL PROCEDURE.....	33
3.1. Raw Materials	33
3.2. Fabrication of the Samples	33
3.2.1. Arc Melting	34
3.2.2. Rapid Solidification by Suction Casting	35

3.3. Characterization of Samples	35
3.3.1. X-Ray Diffractometry	36
3.3.2 Scanning Electron Microscopy.....	36
3.3.3. Differential Scanning Calorimetry.....	36
3.3.4. Vibrating Sample Magnetometry.....	37
3.3.5. MicroHardness Measurement	38
3.3.6 Four Point Probe Measurement.....	38
4. RESULTS AND DISCUSSIONS.....	39
4.1. Production and Characterization of As Cast Alloys	39
4.2 Crystallization Kinetics of the Bulk Glassy Alloys.....	54
4.2.1 Isochronal DSC Analyses.....	54
4.2.2 Isothermal DSC Analyses.....	73
5. CONCLUSIONS	91
REFERENCES	93
APPENDICES	
A. EDS ANALYSES	105
B. PHASE DIAGRAMS.....	117
C. OPTICAL MICROSCOPE IMAGES.....	123
D. SEM IMAGES AND MAPPING MICROGRAPHS.....	125

LIST OF TABLES

TABLES

Table 2.1 Interpretation of Avrami exponents.....	18
Table 2.2 Effect of Annealing on the Magnetic Properties of Different Glassy Alloys Systems.....	29
Table 2.3 Application areas of BMGs.....	31
Table 3.1 Purity Grades of Alloying Elements.....	33
Table 4.1 Glass transition and crystallization temperatures of the bulk glassy $(\text{Fe}_{36}\text{Co}_{36}\text{B}_{19.2}\text{Si}_{4.8}\text{Nb}_4)_{99.25}\text{Cu}_{0.75}$ alloy obtained from DSC pattern.....	46
Table 4.2 Transition temperatures of the bulk glassy $(\text{Fe}_{36}\text{Co}_{36}\text{B}_{19.2}\text{Si}_{4.8}\text{Nb}_4)_{99.25}\text{Cu}_{0.75}$ alloy obtained from DSC pattern at 40 °C/min....	51
Table 4.3 Calculated E_a values of the bulk glassy $(\text{Fe}_{36}\text{Co}_{36}\text{B}_{19.2}\text{Si}_{4.8}\text{Nb}_4)_{99.25}\text{Cu}_{0.75}$ alloy obtained from Kissinger and Ozawa plots for 10,20,40 °C/min.....	67
Table 4.4 Transition temperatures of 1st heating paths of the bulk glassy $(\text{Fe}_{36}\text{Co}_{36}\text{B}_{19.2}\text{Si}_{4.8}\text{Nb}_4)_{99.25}\text{Cu}_{0.75}$ alloy obtained from isochronal DSC analysis at different heating rates.....	68
Table 4.5 Transition temperatures of 1st cooling paths of the bulk glassy $(\text{Fe}_{36}\text{Co}_{36}\text{B}_{19.2}\text{Si}_{4.8}\text{Nb}_4)_{99.25}\text{Cu}_{0.75}$ alloy obtained from isochronal DSC analysis at different heating rates.....	69

Table 4.6 Enthalpy values of 1st cooling paths of the bulk glassy $(\text{Fe}_{36}\text{Co}_{36}\text{B}_{19.2}\text{Si}_{4.8}\text{Nb}_4)_{99.25}\text{Cu}_{0.75}$ alloy obtained from isochronal DSC analysis at different heating rates.....	70
Table 4.7 Transition temperatures of 2nd cooling paths of the bulk glassy $(\text{Fe}_{36}\text{Co}_{36}\text{B}_{19.2}\text{Si}_{4.8}\text{Nb}_4)_{99.25}\text{Cu}_{0.75}$ alloy obtained from isochronal DSC analysis at different heating rates.....	71
Table 4.8 Calculated GFA parameters of the bulk glassy $(\text{Fe}_{36}\text{Co}_{36}\text{B}_{19.2}\text{Si}_{4.8}\text{Nb}_4)_{99.25}\text{Cu}_{0.75}$ alloy obtained from isochronal DSC analysis at different heating rates.....	72
Table 4.9 T_ℓ and T_{xc} values of the bulk glassy $(\text{Fe}_{36}\text{Co}_{36}\text{B}_{19.2}\text{Si}_{4.8}\text{Nb}_4)_{99.25}\text{Cu}_{0.75}$ alloy obtained from isochronal DSC analysis at different heating rates.....	75
Table 4.10 γ_m and R_c values of the bulk glassy $(\text{Fe}_{36}\text{Co}_{36}\text{B}_{19.2}\text{Si}_{4.8}\text{Nb}_4)_{99.25}\text{Cu}_{0.75}$ alloy at different heating rates. R_c was calculated by Liu et al. approach.....	76
Table 4.11 α -(Fe,Co) crystallite sizes estimated by Scherrer formula for annealed bulk glassy $(\text{Fe}_{36}\text{Co}_{36}\text{B}_{19.2}\text{Si}_{4.8}\text{Nb}_4)_{99.25}\text{Cu}_{0.75}$ alloy at different holding times.....	81
Table 4.12 H_c , B_s and B_r values of annealed $(\text{Fe}_{36}\text{Co}_{36}\text{B}_{19.2}\text{Si}_{4.8}\text{Nb}_4)_{99.25}\text{Cu}_{0.75}$ alloys at 535 °C for different holding times.....	96
Table 4.13 H_c , B_s and B_r values of annealed $((\text{Fe}_{36}\text{Co}_{36}\text{B}_{19.2}\text{Si}_{4.8}\text{Nb}_4)_{99.25}\text{Cu}_{0.75})$ alloys at 585 °C for different holding times.....	98
Table 4.14 Vickers microhardness values of the as cast and annealed $(\text{Fe}_{36}\text{Co}_{36}\text{B}_{19.2}\text{Si}_{4.8}\text{Nb}_4)_{99.25}\text{Cu}_{0.75}$ alloys.....	101

LIST OF FIGURES

FIGURES

Figure 2.1 Variation of properties of crystalline and non-crystalline materials with temperature (reproduced after Ref. [22]).....	4
Figure 2.2 Viscosity comparison of different glass-forming liquids [16].....	6
Figure 2.3 The equipment for copper mold casting in a wedge shape form.....	14
Figure 2.4 The schematic of arc melting technique.....	15
Figure 2.5 The schematic of suction casting.....	16
Figure 2.6 The schematic TTT diagram for a hypothetical alloy.....	20
Figure 2.7 Typical strengths and elastic limits for various materials.....	23
Figure 2.8 Elastic limit σ_y vs Young's Modulus E for over 1507 metals, alloys, metal matrix composites and metallic glasses. The contours show the yield strain σ_y/E and the resilience σ_y^2/E	24
Figure 2.9 Coercivity H_c and electrical resistivity ρ of different types of magnetic alloys. Both the Co-based and Fe-based BMG alloys have the desirable combination of low coercivity and high electrical resistivity.....	26

Figure 2.10 DSC curve of a) $(\text{Fe}_{0.75}\text{B}_{0.2}\text{Si}_{0.05})_{96}\text{Nb}_4$ alloy with one stage crystallization. b) $\text{Fe}_{62.8}\text{Co}_{10}\text{B}_{13.5}\text{Si}_{10}\text{Nb}_3\text{Cu}_{0.7}$ alloy with two stages crystallization. This helps the precipitation of crystalline α -Fe phase in glassy matrix.....	28
Figure 2.11 Comparison of corrosion rates of amorphous Fe-Cr-13P-7C alloys and crystalline Fe-Cr alloys in 1N NaCl at 30°C.....	30
Figure 3.1 Copper heart and arc melting.....	34
Figure 3.2 Suction casting unit and rod shaped specimen.....	35
Figure 3.3 DSC used in isochronal thermal analysis.....	37
Figure 3.4 VSM used for magnetic measurements.....	38
Figure 4.1 Cutting of the produced rod shaped bulk glassy $(\text{Fe}_{36}\text{Co}_{36}\text{B}_{19.2}\text{Si}_{4.8}\text{Nb}_4)_{99.25}\text{Cu}_{0.75}$ alloy.....	40
Figure 4.2 XRD patterns of as cast samples from different parts of the bulk glassy $(\text{Fe}_{36}\text{Co}_{36}\text{B}_{19.2}\text{Si}_{4.8}\text{Nb}_4)_{99.25}\text{Cu}_{0.75}$ alloy.....	41
Figure 4.3 Secondary electron image (left) and back scattered electron image (right) of the bulk amorphous $(\text{Fe}_{36}\text{Co}_{36}\text{B}_{19.2}\text{Si}_{4.8}\text{Nb}_4)_{99.25}\text{Cu}_{0.75}$ alloy.....	42
Figure 4.4 Investigated part of the bulk glassy $(\text{Fe}_{36}\text{Co}_{36}\text{B}_{19.2}\text{Si}_{4.8}\text{Nb}_4)_{99.25}\text{Cu}_{0.75}$ alloy for homogeneity.....	43
Figure 4.5 XRD pattern of the part of bulk glassy $(\text{Fe}_{36}\text{Co}_{36}\text{B}_{19.2}\text{Si}_{4.8}\text{Nb}_4)_{99.25}\text{Cu}_{0.75}$ alloy shown in Figure 4.4.....	43
Figure 4.6 Back scattered electron image of dendrites (left) and eutectics (right) the part of bulk glassy $(\text{Fe}_{36}\text{Co}_{36}\text{B}_{19.2}\text{Si}_{4.8}\text{Nb}_4)_{99.25}\text{Cu}_{0.75}$ alloy shown in Figure 4.4.....	44
Figure 4.7 Secondary electron image of dendrites after etching of the part of bulk glassy $(\text{Fe}_{36}\text{Co}_{36}\text{B}_{19.2}\text{Si}_{4.8}\text{Nb}_4)_{99.25}\text{Cu}_{0.75}$ alloy shown in Figure 4.4.....	44
Figure 4.8 Secondary electron image of eutectics after etching of the part of bulk glassy $(\text{Fe}_{36}\text{Co}_{36}\text{B}_{19.2}\text{Si}_{4.8}\text{Nb}_4)_{99.25}\text{Cu}_{0.75}$ alloy shown in Figure 4.4.....	45

Figure 4.9 DSC trace of the bulk glassy $(\text{Fe}_{36}\text{Co}_{36}\text{B}_{19.2}\text{Si}_{4.8}\text{Nb}_4)_{99.25}\text{Cu}_{0.75}$ alloy on heating at 40 °C/min rate.....	46
Figure 4.10 Comparison of 1st (black) and 2nd (red) a) heating paths b) cooling paths of bulk glassy $(\text{Fe}_{36}\text{Co}_{36}\text{B}_{19.2}\text{Si}_{4.8}\text{Nb}_4)_{99.25}\text{Cu}_{0.75}$ alloy at 40 °C/min.....	47
Figure 4.11 Comparison of 1st (black) and 2nd (red) a) heating paths b) cooling paths of head part of the bulk glassy $(\text{Fe}_{36}\text{Co}_{36}\text{B}_{19.2}\text{Si}_{4.8}\text{Nb}_4)_{99.25}\text{Cu}_{0.75}$ alloy at 40 °C/min.....	50
Figure 4.12 Hysteresis loop of the bulk glassy $(\text{Fe}_{36}\text{Co}_{36}\text{B}_{19.2}\text{Si}_{4.8}\text{Nb}_4)_{99.25}\text{Cu}_{0.75}$ alloy. Inset shows the region around zero field strength.....	52
Figure 4.13 R vs I and V vs I graphs for obtaining electrical resistivity value of the bulk glassy $(\text{Fe}_{36}\text{Co}_{36}\text{B}_{19.2}\text{Si}_{4.8}\text{Nb}_4)_{99.25}\text{Cu}_{0.75}$ alloy. Inset shows the region of change of R where is close to zero.....	53
Figure 4.14 1st heating paths of bulk glassy $(\text{Fe}_{36}\text{Co}_{36}\text{B}_{19.2}\text{Si}_{4.8}\text{Nb}_4)_{99.25}\text{Cu}_{0.75}$ alloy at different heating rates.....	56
Figure 4.15 Comparison of low temperature regions of 1st heating paths of bulk glassy $(\text{Fe}_{36}\text{Co}_{36}\text{B}_{19.2}\text{Si}_{4.8}\text{Nb}_4)_{99.25}\text{Cu}_{0.75}$ alloy at different heating rates.....	57
Figure 4.16 Comparison of high temperature regions of 1st heating paths of bulk glassy $(\text{Fe}_{36}\text{Co}_{36}\text{B}_{19.2}\text{Si}_{4.8}\text{Nb}_4)_{99.25}\text{Cu}_{0.75}$ alloy at different heating rates.....	58
Figure 4.17 1st cooling paths of bulk glassy $(\text{Fe}_{36}\text{Co}_{36}\text{B}_{19.2}\text{Si}_{4.8}\text{Nb}_4)_{99.25}\text{Cu}_{0.75}$ alloy at different heating rates.....	59
Figure 4.18 2nd heating paths of bulk glassy $(\text{Fe}_{36}\text{Co}_{36}\text{B}_{19.2}\text{Si}_{4.8}\text{Nb}_4)_{99.25}\text{Cu}_{0.75}$ alloy at different heating rates.....	60
Figure 4.19 2nd cooling paths of bulk glassy $(\text{Fe}_{36}\text{Co}_{36}\text{B}_{19.2}\text{Si}_{4.8}\text{Nb}_4)_{99.25}\text{Cu}_{0.75}$ alloy at different heating rates.....	61
Figure 4.20 a) Kissinger b) Ozawa plots of bulk glassy $(\text{Fe}_{36}\text{Co}_{36}\text{B}_{19.2}\text{Si}_{4.8}\text{Nb}_4)_{99.25}\text{Cu}_{0.75}$ alloy for 10, 20, 40 °C/min.....	62

Figure 4.21 Barandiaran-Colmenero plots of the bulk glassy $(\text{Fe}_{36}\text{Co}_{36}\text{B}_{19.2}\text{Si}_{4.8}\text{Nb}_4)_{99.25}\text{Cu}_{0.75}$ alloy for 10, 20, 40 °C/min. T_{xc} values obtained from a) second and b) first cooling paths.....	70
Figure 4.22 Comparison of Barandiaran-Colmenero plots for first and second cooling paths of the bulk glassy $(\text{Fe}_{36}\text{Co}_{36}\text{B}_{19.2}\text{Si}_{4.8}\text{Nb}_4)_{99.25}\text{Cu}_{0.75}$ alloy for 10, 20 and 40 °C/min.....	71
Figure 4.23 R_c calculated by Liu et al. approach vs γ_m plots of the bulk glassy $(\text{Fe}_{36}\text{Co}_{36}\text{B}_{19.2}\text{Si}_{4.8}\text{Nb}_4)_{99.25}\text{Cu}_{0.75}$ alloy for different heating rates.....	72
Figure 4.24 Isothermal DSC traces of the bulk amorphous $(\text{Fe}_{36}\text{Co}_{36}\text{B}_{19.2}\text{Si}_{4.8}\text{Nb}_4)_{99.25}\text{Cu}_{0.75}$ alloy at 535 °C and 585 °C for all holding times. 5 min annealing at 585 °C shows an exothermic peak but for all other holding times no exothermic peaks were appeared for both 535 °C and 585 °C.....	74
Figure 4.25 XRD patterns of the bulk glassy $(\text{Fe}_{36}\text{Co}_{36}\text{B}_{19.2}\text{Si}_{4.8}\text{Nb}_4)_{99.25}\text{Cu}_{0.75}$ alloy at 535 °C for different holding times.....	75
Figure 4.26 XRD patterns of the bulk glassy $(\text{Fe}_{36}\text{Co}_{36}\text{B}_{19.2}\text{Si}_{4.8}\text{Nb}_4)_{99.25}\text{Cu}_{0.75}$ alloy at 585 °C for different holding times.....	76
Figure 4.27 Changes of crystalite size vs time graph of the bulk glassy $(\text{Fe}_{36}\text{Co}_{36}\text{B}_{19.2}\text{Si}_{4.8}\text{Nb}_4)_{99.25}\text{Cu}_{0.75}$ alloy at 535 °C and 585 °C.....	77
Figure 4.28 Back scattered electrons images of the bulk amorphous $(\text{Fe}_{36}\text{Co}_{36}\text{B}_{19.2}\text{Si}_{4.8}\text{Nb}_4)_{99.25}\text{Cu}_{0.75}$ alloy at 535 °C (left) and 585 °C (right).....	78
Figure 4.29 SEM images and mapping micrographs of the annealed $(\text{Fe}_{36}\text{Co}_{36}\text{B}_{19.2}\text{Si}_{4.8}\text{Nb}_4)_{99.25}\text{Cu}_{0.75}$ alloy at a) 535 °C b) at 585 °C.....	79
Figure 4.30 B-H loops of the as cast alloy and annealed $(\text{Fe}_{36}\text{Co}_{36}\text{B}_{19.2}\text{Si}_{4.8}\text{Nb}_4)_{99.25}\text{Cu}_{0.75}$ alloys at 535 °C for different holding times. While upper inset shows change of B_s , below inset shows the region around zero field strength.....	82

Figure 4.31 Changes of H_c and B_s vs time graph of the annealed $(Fe_{36}Co_{36}B_{19.2}Si_{4.8}Nb_4)_{99.25}Cu_{0.75}$ alloy at 535 °C.....	83
Figure 4.32 B-H loops of the as cast alloy and annealed $(Fe_{36}Co_{36}B_{19.2}Si_{4.8}Nb_4)_{99.25}Cu_{0.75}$ alloys at 585 °C for different holding times. While upper inset shows change of B_s , below inset shows the region around zero field strength.....	84
Figure 4.33 Changes of H_c and B_s vs time graph of the annealed $(Fe_{36}Co_{36}B_{19.2}Si_{4.8}Nb_4)_{99.25}Cu_{0.75}$ alloy at 585 °C.....	85
Figure 4.34 B-H loops of the as cast alloy and annealed $(Fe_{36}Co_{36}B_{19.2}Si_{4.8}Nb_4)_{99.25}Cu_{0.75}$ alloy at 585 °C for 5 min. Inset shows the region around zero field strength.....	86
Figure 4.35 Vickers hardness and Young's modulus for some bulk metallic glasses.....	87
Figure 4.36 Followed pattern of $(Fe_{36}Co_{36}B_{19.2}Si_{4.8}Nb_4)_{99.25}Cu_{0.75}$ alloy for Vickers microhardness measurements.....	88
Figure 4.37 Vickers microhardness vs followed pattern graph for $(Fe_{36}Co_{36}B_{19.2}Si_{4.8}Nb_4)_{99.25}Cu_{0.75}$ alloy.....	89
Figure A.1 EDS analysis of bulk amorphous $(Fe_{36}Co_{36}B_{19.2}Si_{4.8}Nb_4)_{99.25}Cu_{0.75}$ alloy.....	105
Figure A.2 EDS analysis of dendrites stated as dark for the head part of the bulk amorphous $(Fe_{36}Co_{36}B_{19.2}Si_{4.8}Nb_4)_{99.25}Cu_{0.75}$ alloy.....	106
Figure A.3 EDS analysis of dendrites stated as light for the head part of the bulk amorphous $(Fe_{36}Co_{36}B_{19.2}Si_{4.8}Nb_4)_{99.25}Cu_{0.75}$ alloy.....	107
Figure A.4 EDS analysis of dendrites stated as gray for the head part of the bulk amorphous $(Fe_{36}Co_{36}B_{19.2}Si_{4.8}Nb_4)_{99.25}Cu_{0.75}$ alloy.....	108

Figure A.5 EDS analysis of eutectics stated as dark for the head part of the bulk amorphous $(\text{Fe}_{36}\text{Co}_{36}\text{B}_{19.2}\text{Si}_{4.8}\text{Nb}_4)_{99.25}\text{Cu}_{0.75}$ alloy.....	109
Figure A.6 EDS analysis of eutectics stated as light for the head part of the bulk amorphous $(\text{Fe}_{36}\text{Co}_{36}\text{B}_{19.2}\text{Si}_{4.8}\text{Nb}_4)_{99.25}\text{Cu}_{0.75}$ alloy.....	110
Figure A.7 EDS analysis of eutectics stated as gray for the head part of the bulk amorphous $(\text{Fe}_{36}\text{Co}_{36}\text{B}_{19.2}\text{Si}_{4.8}\text{Nb}_4)_{99.25}\text{Cu}_{0.75}$ alloy.....	111
Figure A.8 EDS analysis of white region in both dendrites and eutectics for the head part of the bulk amorphous $(\text{Fe}_{36}\text{Co}_{36}\text{B}_{19.2}\text{Si}_{4.8}\text{Nb}_4)_{99.25}\text{Cu}_{0.75}$ alloy.....	112
Figure A.9 EDS analysis of the dendrites for $(\text{Fe}_{36}\text{Co}_{36}\text{B}_{19.2}\text{Si}_{4.8}\text{Nb}_4)_{99.25}\text{Cu}_{0.75}$ alloy annealed isothermally at 535 °C.....	113
Figure A.10 EDS analysis of the surroundings of the dendrites for $(\text{Fe}_{36}\text{Co}_{36}\text{B}_{19.2}\text{Si}_{4.8}\text{Nb}_4)_{99.25}\text{Cu}_{0.75}$ alloy annealed isothermally at 535 °C.....	114
Figure A.11 EDS analysis of the dendrites for $(\text{Fe}_{36}\text{Co}_{36}\text{B}_{19.2}\text{Si}_{4.8}\text{Nb}_4)_{99.25}\text{Cu}_{0.75}$ alloy annealed isothermally at 585 °C.....	115
Figure A.12 EDS analysis of the surroundings of the dendrites for $(\text{Fe}_{36}\text{Co}_{36}\text{B}_{19.2}\text{Si}_{4.8}\text{Nb}_4)_{99.25}\text{Cu}_{0.75}$ alloy annealed isothermally at 585 °C.....	116
Figure B.1 Co-Fe Phase Diagram.....	117
Figure B.2 Fe-Si Phase Diagram.....	118
Figure B.3 Fe-B Phase Diagram.....	119
Figure B.4 Nb-Si Phase Diagram.....	120
Figure B.5 B-Nb Phase Diagram.....	121
Figure C.1 Optic microscope image of the $(\text{Fe}_{36}\text{Co}_{36}\text{B}_{19.2}\text{Si}_{4.8}\text{Nb}_4)_{99.25}\text{Cu}_{0.75}$ alloy annealed isothermally at 535 °C.....	123
Figure C.2 Optic microscope image of the $(\text{Fe}_{36}\text{Co}_{36}\text{B}_{19.2}\text{Si}_{4.8}\text{Nb}_4)_{99.25}\text{Cu}_{0.75}$ alloy annealed isothermally at 585 °C.....	124

Figure D.1-D.5 SEM images and mapping micrographs of the annealed (Fe ₃₆ Co ₃₆ B _{19.2} Si _{4.8} Nb ₄) _{99.25} Cu _{0.75} alloy at 535 °C.....	125
Figure D.6-D11 SEM images and mapping micrographs of the annealed (Fe ₃₆ Co ₃₆ B _{19.2} Si _{4.8} Nb ₄) _{99.25} Cu _{0.75} alloy at 585 °C.....	129

CHAPTER 1

INTRODUCTION

Materials science dealt mostly with crystalline materials and their physics and chemistry due to symmetrical nature of crystalline materials and less challenging calculations made on them. Today, however, amorphous materials have become popular field because of their unclear nature. Amorphous materials have random atomic arrangements and superior properties compared to their crystalline counterparts [1-6]. Among these materials, Fe-based amorphous alloys have drawn much attention due to their outstanding soft magnetic behavior [7, 8], excellent corrosion resistance [9, 10], and good mechanical properties [11, 12] for potential structural applications such as transformers and magnetic sensors.

Typically, amorphous alloys are produced by rapid solidification from liquid state which kinetically suppresses crystallization. In this way, purely metallic and metal-metalloid glasses were developed to investigate their metallurgical formation which is different from oxide or polymeric glasses. Metallic glasses are non-equilibrium structures, thus, when they heated moderately, they become structural changes from the as cast state to the metastable structurally relaxed state and finally to the crystalline state. Due to these structural changes, physical, chemical, and mechanical properties of the metallic glasses are significantly affected. Therefore, the study of crystallization behaviour of metallic glasses, to understand structure property relationships and the mechanism of nanocrystallization are very important due to the fact that crystallization parameters of an amorphous phase show the stability of it against the thermal treatments.

In the light of these informations, in this thesis, $(\text{Fe}_{36}\text{Co}_{36}\text{B}_{19.2}\text{Si}_{4.8}\text{Nb}_4)_{99.25}\text{Cu}_{0.75}$ bulk amorphous alloy having a high glass forming ability (GFA) and soft magnetic property has been synthesized and attempts have been made on understanding the crystallization behaviour of the amorphous $(\text{Fe}_{36}\text{Co}_{36}\text{B}_{19.2}\text{Si}_{4.8}\text{Nb}_4)_{99.25}\text{Cu}_{0.75}$ alloy by using thermo-analytical methods and annealing experiments. This alloy was chosen because by former studies in our laboratory (NOVALAB), it was confirmed that $(\text{Fe}_{36}\text{Co}_{36}\text{B}_{19.2}\text{Si}_{4.8}\text{Nb}_4)_{99.25}\text{Cu}_{0.75}$ alloy can be produced as a bulk amorphous form and has a good soft magnetic property [13]. First of all, $\text{Fe}_{36}\text{Co}_{36}\text{B}_{19.2}\text{Si}_{4.8}\text{Nb}_4$ alloy was produced as bulk amorphous alloy by centrifugal casting method. Then, different amount of Cu was added. In $(\text{Fe}_{36}\text{Co}_{36}\text{B}_{19.2}\text{Si}_{4.8}\text{Nb}_4)_{100-x}\text{Cu}_x$ composition x was changed like $x= 0, 0.25, 0.5, 0.75, 1$. After characterizations of the alloys, it was proved that $(\text{Fe}_{36}\text{Co}_{36}\text{B}_{19.2}\text{Si}_{4.8}\text{Nb}_4)_{99.25}\text{Cu}_{0.75}$ alloy showed the best GFA and soft magnetic properties. However, the crystallization kinetics of this alloy has not been studied in detail so far. Thus, this study aims investigating the crystallization kinetics of $(\text{Fe}_{36}\text{Co}_{36}\text{B}_{19.2}\text{Si}_{4.8}\text{Nb}_4)_{99.25}\text{Cu}_{0.75}$ alloy and its effect on soft magnetic property of it by means of the experimental and analytical methods. $(\text{Fe}_{36}\text{Co}_{36}\text{B}_{19.2}\text{Si}_{4.8}\text{Nb}_4)_{99.25}\text{Cu}_{0.75}$ alloy was produced by suction casting into copper mold in the form of cylindrical rod with diameter of 3 mm. Then, it was characterized by X-ray diffractions, thermal and magnetic analysis and microstructural investigations. Kinetic analyses of the sample were performed to obtain the critical parameters for mechanisms and suppression of the crystallization.

The literature review of this study was given in Chapter Two. Experimental procedure details were presented in Chapter Three. The results of the experiments and discussions were given in Chapter Four. Conclusions that have fundamental points which were achieved during this study were given in Chapter Five.

CHAPTER 2

THEORY

2.1 HISTORY OF METALLIC GLASSES

The first metallic glass was reported by Duwez and his colleagues at the California Institute of Technology (CalTech) in 1960. In their study, Au₇₅Si₂₅ alloy was rapidly solidified at rates of about 10⁶ K/s and nucleation and growth processes of crystallization could be kinetically bypassed [14]. In 1970s and 1980s the researches about metallic glasses have increased the attention due to their importance in fundamental scientific significance and potential engineering applications [15, 16]. The work of Turnbull group showed similarities between between metallic glasses and other conventional glasses. According to their studies, metallic glasses also show glass transition temperature. This study is one of the crucial contributions in the field of metallic glass [17, 18]. During late 1980's, synthesis of centimeter level bulk metallic glasses was successfully produced by Turnbull and coworkers [19, 20] for Pd–Ni–P alloy system with cooling rates as low as 10 K/s. These metallic glasses larger than millimeter scale were the first bulk metallic glasses (BMGs). Following 1990s, many researches on the BMGs were done to find new alloy compositions and investigate their physical, structural, mechanical and magnetic properties. These materials provide new opportunities for both fundamental studies and commercial applications. Owing to the relative ease of fabricating metallic glasses into bulk forms with other unique properties, BMGs are attractive for possible applications in aerospace, naval, armor systems, electronic packaging, and biomedical devices. Based on the recent developments, new applications of the bulk metallic glasses can be expected in the near future [1, 21].

2.2.2 Glass Formation

Glass formation of metallic alloys can be interpreted by considering thermodynamic and kinetic aspects.

2.2.2.1 Thermodynamics of Glass Formation

Thermodynamic is one of the most fundamental approaches to determine the relative stability of phases and limitations of glass forming. The Gibbs free energy (ΔG) is the term which shows the stability of any phases.

$$\Delta G = \Delta H_{tr} - T\Delta S_{tr} \quad \text{and} \quad (\Delta G = G_{\text{glass}} - G_{\text{crystal}}) \quad (2.1)$$

where ΔH_{tr} is enthalpy of transformation and ΔS_{tr} is entropy of transformation

According to Eq. 2.1, when ΔG value is the lowest, system becomes more stable. As the Gibbs free energy becomes negative the glass formation becomes more favorable. In order to obtain negative ΔG , either ΔH_{tr} term should be lowered or ΔS_{tr} term should be increased.

The entropy of the system represents the measure of arrangement of constituent atoms. In metallic glasses with high number of constituent elements, entropy increases because of the diversity of arrangement possibilities. This increase in ΔS_{tr} of atoms of metallic glasses leads to the decrease of ΔH_{tr} . As a result, the solid/liquid interfacial energy will increase [24]. In this way, production of multicomponent BMGs is much easier and requires lower cooling rates than binary alloy systems.

2.2.2.2 Kinetics of Glass Formation

In the kinetic approach, viscosity has an important influence on metallic glasses and glass forming abilities. The variation of viscosity of a liquid as a function of undercooling is used for categorizing and characterizing the liquids since it reveals

the change of mobility of atom during supercooling. Viscosity can be determined from Vogel-Fulcher-Tammann (VFT) relation [25]:

$$\eta = \eta_0 \exp \left[\frac{DT_0}{T - T_0} \right] \quad (2.2)$$

where T_0 is Vogel-Fulcher temperature and D is the fragility parameter.

Previous studies showed that the liquid which forms BMGs behaves like the silicate melts kinetically. In Figure 2.2, the viscosities of common non-metallic liquids were compared with metallic glasses. SiO_2 shows high melt viscosity and the strongest glass formability with fragility parameter around 100. In accordance with the plot, BMG forming liquids could be classified as strong liquids like silica glasses. The melt viscosities of the BMG former liquids have fragility parameters around 20 [16].

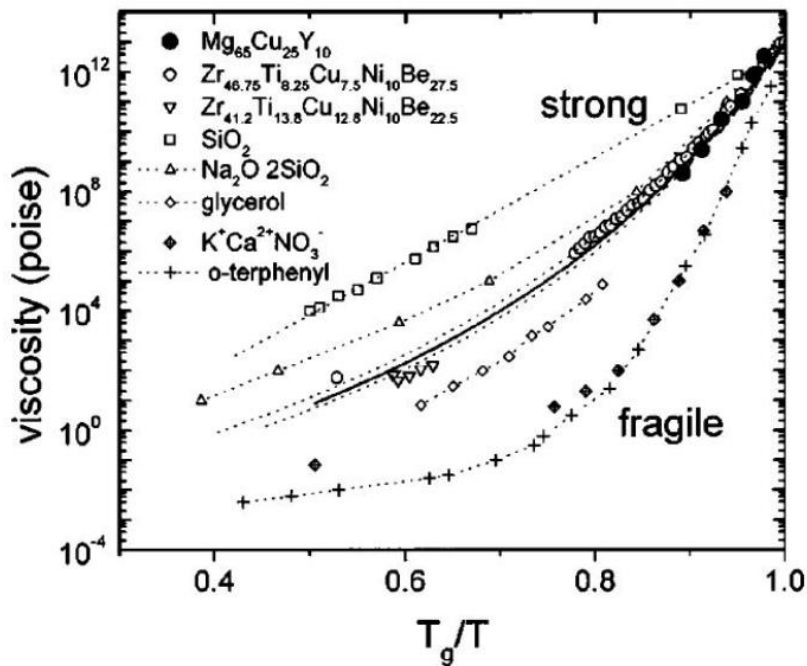


Figure 2.2 Viscosity comparison of different glass-forming liquids [16].

2.3 GLASS FORMING ABILITY CRITERIA FOR BULK METALLIC GLASSES

In order to design new alloys, understanding of glass forming ability (GFA) is important. The GFA can be defined as the ability of the alloy to transform into amorphous state. Since the first discovery of bulk metallic glasses there has been a lot of studies on the development of a universal criterion in estimating GFA. However, these studies still remain at the empirical level. Inoue [26] states three empirical rules for obtaining glass formation in metallic alloy systems;

- (1) Alloy consists of more than three elements,
- (2) Atomic size mismatches are required to be above 12% among the main constituent elements
- (3) Negative heats of mixing among the main elements is necessary.

The other several approaches in literature are also stated in the following sections.

2.3.1 Supercooled Liquid Region (ΔT_x)

Supercooled liquid region ΔT_x ($\Delta T_x = T_x - T_g$) is the region between the glass transition (T_g) and the crystallization temperatures (T_x). It is regarded as a measure of GFA since ΔT_x represents how stable is a liquid against crystallization upon heating above T_g . The value of ΔT_x can be different depending on the alloy system and is usually in the range of 40–90 K. Supercooled liquid region becomes wider glassy phase is more stable and shows more resistance to crystallization [1, 24, 27].

2.3.2 Reduced Glass Transition Temperature (T_{rg})

When a liquid alloy is cooled down to a temperature below T_g , the viscosity of the melt increases and glass is formed. Since the viscosity is constant at T_g as 10^{12} Pa.s, Turnbull, based on kinetics of crystal nucleation and the viscosity of melts, suggested that the ratio of the glass transition temperature T_g to the liquidus temperature of the alloy T_l is a good indicator of the GFA of the alloy. The higher

this value, the higher is the viscosity and therefore the alloy melt could be easily solidified into the glassy state at a low critical cooling rate (R_c). In other words, an alloy composition with as high a value of T_g and as low a value of T_l as possible promote easy glass formation. This ratio is called as reduced glass transition temperature T_{rg} . That is, $T_{rg} = T_g/T_l$. Based on the nucleation theory, Turnbull showed that at $T_{rg} \geq 2/3$, homogeneous nucleation of the crystalline phase is completely suppressed.

The minimum value of $T_{rg} \cong 0.4$ is necessary for an alloy to become a glass, but the higher the T_{rg} value, glass formation is easier. Most of the alloys indicate T_{rg} in the range of 0.6-0.69 [24, 28, 29].

2.3.3 K_{gl} Parameter

Another parameter which is a numerical measure of the GFA is the K_{gl} parameter proposed by Hruby [30]. K_{gl} is defined by

$$K_{gl} = \frac{(T_x - T_g)}{(T_m - T_x)} \quad (2.3)$$

This criterion expresses the thermal stability of a glass on subsequent reheating and it is directly proportional to the ease of glass formation.

2.3.4 S Parameter

The stability parameter S is developed by Saad and Poulain [31]. It can be expressed by

$$S = \frac{(T_p - T_x)(T_x - T_g)}{T_g} \quad (2.4)$$

where T_p is the crystallization peak temperature. This parameter describes the effect of temperature difference between T_p and the onset crystallization temperature together with the position of T_g and crystallization exotherm.

2.3.5 ϕ Parameter

Fan et al. [32] developed a new GFA criteria using the nucleation theory and the fragility concept. They stated that overestimation of GFA due to the usage of T_{rg} parameter could be corrected by introducing ΔT_x . The new criteria is expressed by

$$\Phi = T_{rg} \left(\frac{\Delta T_x}{T_g} \right)^a \quad (2.5)$$

where a is a constant. They tested the validation of the ϕ parameter in different type of glasses by plotting the R_c vs ϕ graphs. ϕ parameter showed a good correlation with R_c .

2.3.6 γ Parameter

γ parameter was developed based on the information on TTT diagrams. Lu and Liu [33] developed γ parameter by considering the two kinds of stability of BMGs. First one is the thermodynamically stability, lower the T_l higher the stability of liquid, and the other one is the resistance to crystallization, determined by the value of the T_g . From the combination of these γ is defined as

$$\gamma = \frac{T_x}{T_g + T_l} \quad (2.6)$$

Liu et al. [34] also studied the relation between the γ values and the critical cooling rate (R_c) for glass formation for some metallic glasses. A linear interrelationship is

expressed by $R_c = R_0 \exp [(-\ln R_0 / \gamma_0) \gamma]$ where R_0 and γ_0 are constants, R_c in K/s and γ is dimensionless. They stated that for metallic glass with the least dimension of 1 mm, the alloy should have γ value of 0.362 or higher.

2.3.7 γ_m Parameter

Du et. al. [35] enhanced γ_m parameter by including the stability of supercooled liquid region because wider ΔT_x more stable liquid against crystallization. They extended the parameter as

$$\gamma_m = \frac{2T_x - T_g}{T_l} \quad (2.7)$$

Authors also found a linear relationship between γ_m and R_c such as $\log_{10} R_c = 14.99 - 19.441 \gamma_m$.

2.3.8 δ Parameter

Chen et al. [36, 37] stated that the GFA of alloys should be inversely proportional to the rates of nucleation and growth. They noted that GFA is proportional to $T_g / (T_l - T_g)$. Further, examining the dependency of GFA on the viscosity of the melt, they also noticed that GFA is proportional to T_x / T_g . Combining these two they proposed a parameter δ for determining GFA. δ parameter is

$$\delta = \frac{T_x}{T_l - T_g} \quad (2.8)$$

Chen et al. have also conducted a statistical analysis of the T_{rg} , γ , and δ parameters against the maximum section diameter of the glassy alloys. Among other parameters, δ was found to have the strongest ability to reflect the GFA.

2.3.9 α and β Parameters

Mondal and Murty [38] derived two parameter to assess the GFA of BMGs. Low T_1 could be an indicator of the high stability of the liquid and high T_x was of a high thermal stability. They combined these effects into one parameter α defined as

$$\alpha = \frac{\Delta T_x}{T_1} + \frac{T_g}{T_1} = \frac{T_x}{T_1} \quad (2.9)$$

Mondal and Murty [38] also proposed that another parameter β , by combining two aspects of glass formation namely the ability to form a glass during cooling of the melt expressed by $T_{rg} = T_g/T_1$, and stability of glass expressed by T_x/T_g . Then, β parameter is

$$\beta = \frac{T_x}{T_g} + \frac{T_g}{T_1} \quad (2.10)$$

If a glass does not exhibit T_g during the heating of it, T_x can be taken as T_g and then, β parameter is written as

$$\beta = 1 + \frac{T_x}{T_1} = 1 + \alpha \quad (2.11)$$

2.3.10 ω Parameter

Long et. al. [39] proposed another parameter which covers the thermodynamic properties of BMG systems based on the analysis of the TTT diagrams using fragility concept. This parameter is

$$\omega = \frac{T_g}{T_x} - \frac{2T_g}{T_g+T_1} \quad (2.12)$$

2.3.11 T_{rx} Parameter

Kim et al. [40] defined a parameter T_{rx} as $T_{rx} = T_x/T_s$ where T_s represents the onset temperature of solidification. T_x value can be obtained from reheating of glassy alloy in DSC or DTA. T_s value can be obtained as the solidification start temperature during cooling of the liquid at a cooling rate R , lower than the critical cooling rate, R_c . During continuous heating, from the point of intersection of the TTT curve with the heating rate curve T_x can be obtained. Thus, T_{rx} is dependent both heating and cooling rates.

2.3.12 New β parameter

Yuan et al. [41] conducted a new different criterion called new β parameter defined as;

$$\text{New } \beta = \frac{T_x \times T_g}{(T_l - T_x)^2} \quad (2.13)$$

They stated that the new β parameter has the strongest ability to represent the GFA because correlation coefficient is the highest among all the other parameters. However, they had plotted t_{max} values instead of their logarithmic values to calculate the correlation coefficients. They also stated that the new β parameter has a very wide range, while the other parameters have a very narrow range for different critical diameters of BMGs.

2.3.13 γ_c parameter

Sheng and Liu [42] derived a new GFA parameter γ_c considering the relationship between the cooling and heating processes. γ_c defined as;

$$\gamma_c = \frac{3T_x - 2T_g}{T_l} \quad (2.14)$$

They stated that the new parameter has clear physical interpretation and good correlation with the critical cooling rate. They also proposed that γ_c replace with γ_m as the best characteristic temperature-based GFA criterion.

2.4 PRODUCTION METHODS OF BULK METALLIC GLASSES

Bulk metallic glasses require rapid solidification techniques to obtain high cooling rates and to suppress the crystallization reaction. A number of different techniques have been developed to synthesize BMG alloys [24]. Some of them are copper mold casting, arc melting, suction casting and centrifugal casting.

2.4.1 Copper Mold Casting

Copper mold casting is the most common and popular method to produce BMGs. In this method, the molten alloy is poured into a copper mold where it solidifies rapidly due to the quick heat extraction by the mold. The casting can be done in air or vacuum, inert atmosphere, or under argon, if oxidation has to be avoided. The mold used can take different forms. The most common form of the mold is cylindrical or rod-shaped cavity which has different internal diameters. Thus, in these molds, for obtaining fully glassy state maximum diameter of the sample should be determined. On the other hand, by using wedge shape mold, using of molds of different internal diameters could not be necessary. The advantage of wedge shape mold is to get specimens of different diameters in one experiment. This provides in determining the maximum diameter of the rod that could be produced in the glassy state in one single experiment [24, 43, 44]. Figure 2.3 shows the equipment for copper mold casting in a wedge shape form.

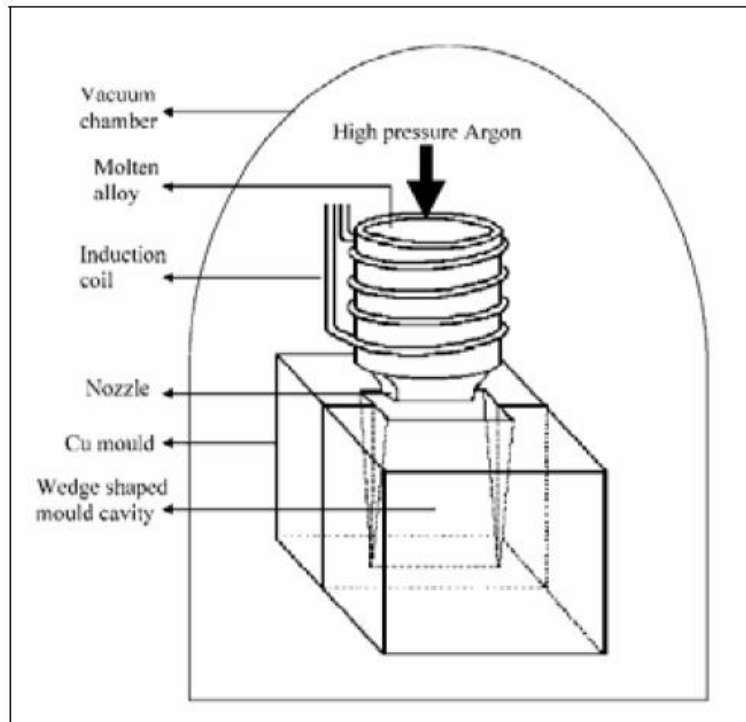


Figure 2.3 The equipment for copper mold casting in a wedge shape form [43].

2.4.2 Arc Melting

Arc melting is the method to obtain glassy phases in alloy systems that require a low critical cooling rate for glass formation. In this method, the alloy on a copper hearth is arc melted. When the alloy is melted, the copper hearth acts like a heat sink and extracts the heat from the melt. Figure 2.4 shows the schematic drawing of this technique. However, in this method it is difficult to completely suppress the precipitation of crystalline phase due to the ease of heterogeneous nucleation by incomplete melting of the alloy at the bottom side contacted with the copper hearth [24, 45].

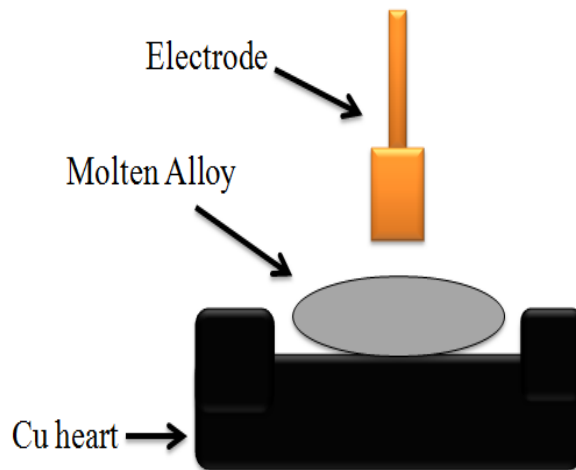


Figure 2.4 The schematic drawing of arc melting technique.

2.4.3 Suction Casting

Suction casting is another popular method to produce BMGs. Figure 2.5 shows the schematic drawing of this technique. First, the alloy is arc melted. Then, molten alloy is sucked into the copper mold by using pressure difference between the melting chamber and the casting chamber. Suction casting is used for casting of materials with diameters smaller than 6 mm. Cooling rates can be controlled by the adjustable pressure difference between the chambers [24, 46-48].

2.4.4 Centrifugal Casting

Centrifugal casting is one of the methods used for producing BMGs in Novel Alloys Design and Development Laboratory (NOVALAB) [49, 50]. In this technique, production of alloys is almost same in industry. First, alloys are arc melted and then, casted into copper mold by centrifugal force. This conventional route provides mass production of BMGs and reduces their costs.

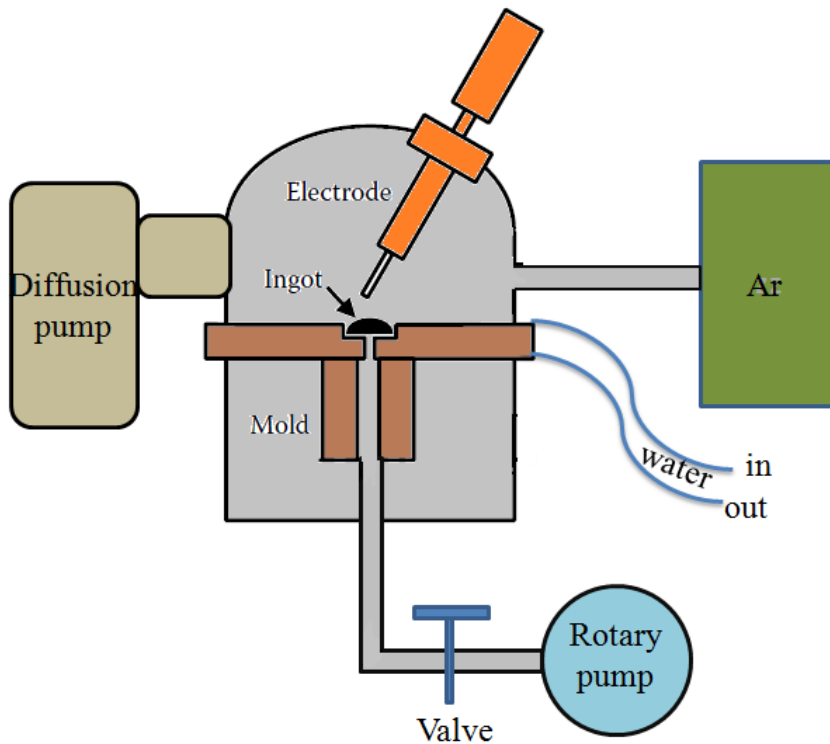


Figure 2.5 The schematic drawing of suction casting.

2.5 CRYSTALLIZATION OF BULK METALLIC GLASSES

2.5.1 Crystallization Kinetics

The crystallization studies of alloys are important for both scientific and technological aspects. From the scientific point of view, crystallization of metallic glasses occurs by a nucleation and growth process thus, the growth of crystals into an isotropic medium can be studied. From the technological point of view, the crystallization of metallic glasses provides variation of their important properties such as magnetic properties [13]. For investigating crystallization kinetics, thermal analysis method such as differential scanning calorimeter (DSC) is quite popular. By using DSC, kinetic parameters that reflect the crystallization behaviours are determined from theories called Johnson-Mehl-Avrami-Kolmogorov (JMAK) [51-53] and Kissinger [54] or Ozawa [55]. JMAK model are generally used to

describe the isothermal transformation kinetics of amorphous alloys. Kissinger or Ozawa is usually used for non-isothermal crystallization.

2.5.1.1 Isothermal Crystallization Kinetics: JMAK Method

JMAK equation was derived based on following assumptions [56, 57]:

- (1) Homogeneous or heterogeneous nucleation at randomly dispersed second phase particles,
- (2) Growth rate of new phase controlled by temperature and independent on time,
- (3) Low anisotropy of growing crystals.

The equation is [53];

$$X(t) = 1 - \exp(-k(t-t_0)^n) \quad (2.15)$$

where; $X(t)$: transformed fraction at time t , k : rate constant,

n : Avrami exponent,

t_0 : incubation time.

Rearranging the JMAK relation yields [58, 59];

$$\ln(-\ln(1 - X(t))) = \ln k + n \ln (t-t_0) \quad (2.16)$$

For analyzing the equation (2.15) and crystallization kinetics, $\ln(-\ln(1 - X(t)))$ vs $\ln(t-t_0)$ is plotted. This plot should give a straight line having the slope n and the intercept $\ln k$ [58, 59].

Avrami exponent (n) provides useful information on the mechanism and geometry of growing precipitates. It can be interpreted by;

Table 2.1 Interpretation of Avrami exponents [60].

Interface controlled growth	Avrami Exponent
Increasing nucleation rate	> 4
Constant nucleation rate	4
Decreasing nucleation rate	3-4
Zero nucleation rate	3
Grain edge nucleation after site saturation	2
Grain boundary nucleation after site saturation	1

Diffusion controlled growth of precipitates	Avrami Exponent
All shapes growing from small dimensions with increasing nucleation rate	$> 2\frac{1}{2}$
All shapes growing from small dimensions with constant nucleation rate	$2\frac{1}{2}$
All shapes growing from small dimensions with decreasing nucleation rate	$1\frac{1}{2} - 2\frac{1}{2}$
All shapes growing from small dimensions with zero nucleation rate	$1\frac{1}{2}$
Growth of precipitates with appreciable initial volume	$1 - 1\frac{1}{2}$
Needles and plates of finite dimensions	1
Thickening of very large plates after complete edge impingement	$\frac{1}{2}$
Thickening of needles after complete end impingement	1
Precipitation on dislocations very early stage	$\frac{2}{3}$

Furthermore, it is possible to estimate the activation energies for a phase transformation using the classical JMAK theory. Imposing an Arrhenius temperature dependence of the rate constant k , different isothermal temperatures can be employed to obtain an overall the activation energy (E_a) employing the relation;

$$k = k_0 \exp\left(-\frac{E_a}{RT}\right) \quad (2.17)$$

and by constructing $\ln k$ vs. $1/T$ plots where the slope is $-E_a/R$, k_0 is a constant and E_a is the activation energy for crystallization. The value of k and n are obtained from JMAK plots for different annealing temperatures [58, 59].

The local activation energy, $E_a(X)$ can also be calculated using equation (2.18) for each transformed fraction by utilizing an Arrhenius thermal dependence of time required to attain a chosen transformed fraction at different isotherms, by taking the slopes $\ln(1/t)$ vs. $(1/T)$ plots [58, 59].

$$\frac{1}{t(X(t))} = A \exp\left(-\frac{E_a(X)}{RT}\right) \quad (2.18)$$

2.5.1.2 Non-Isothermal Crystallization Kinetics: Kissinger and Ozawa Method

Kissinger [54] proposed a method for determining the activation energy of a simple decomposition reaction regardless of reaction order by making differential analysis patterns at different heating rates. He related the heating rate of a reaction to the peak temperature recorded by thermal analysis by an expression:

$$\ln\left(\frac{\beta}{T_p^2}\right) = -\frac{E_a}{RT_p} + C \quad (2.19)$$

where β is the heating rate, T_p is the peak temperature, R is the gas constant, E_a is the activation energy for the corresponding transition, and C is a constant.

Plotting $\ln\left(\frac{\beta}{T_p^2}\right)$ vs $1/T_p$ yields a straight line whose slope gives $-E_a/R$ for crystallization. From this E_a can be calculated.

Another widely used non-isothermal method is the Ozawa [55] method;

$$\ln(\beta) = -1.0516 \frac{E_a}{RT_p} + C \quad (2.20)$$

where β is the heating rate and E_a is the activation energy. The plot of $\ln\beta$ versus $1/T_p$ gives a straight line with a slope of $-1.0516 E_a/R$.

2.5.2 Critical Cooling Rate Calculations

Determination of the critical cooling rate (R_c) is very important in studying crystallization kinetics because it is the minimum rate to suppress detectable crystal nuclei. The best way to determine R_c is to construct time-temperature-transformation (TTT) diagrams. Figure 2.6 shows a schematic TTT diagram for a hypothetical alloy [24, 61].

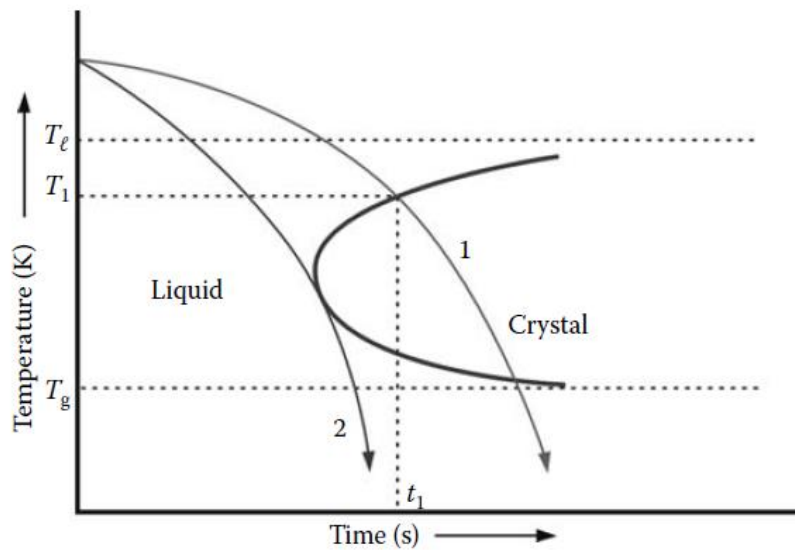


Figure 2.6 The schematic TTT diagram for a hypothetical alloy [24].

TTT curve shows the time required for formation of crystalline phase. When the alloy is cooled from the liquid state under equilibrium conditions, product of solidification would be a crystalline solid. If the alloy is solidified at a higher solidification rate represented by curve 1 the product is still a crystalline solid. However, if the liquid alloy is solidified at a rate faster than the cooling rate represented by curve 2, then crystal formation will not take place.

The cooling rate represented by curve 2 is called the critical cooling rate (R_c). The significance of this value is that above this rate, glass can be formed provided that the supercooled liquid is cooled to a temperature below T_g . If the alloy melt is cooled at a rate lower than R_c , a homogeneous glassy phase will not form. For glass formation, the liquid alloy should be cooled at a rate faster than R_c and to a temperature below T_g [24, 61].

Critical cooling rates (R_c) for different alloys systems can be calculated by isothermal crystallization kinetics. If T_n and t_n are temperature and time at the nose of the curve, and T_1 is the liquidus temperature, R_c [62] can be defined as;

$$R_c \cong \frac{T_1 - T_n}{t_n} \quad (2.21)$$

However, this expression overestimates R_c , since it assumes that the crystallization rate corresponds to the nose of the TTT curve throughout the whole temperature interval of T_1 to T_n , and therefore results in a value somewhat higher than the experimentally determined value [63].

The equation (2.21) is valid only for isothermal processes but in reality, glass formation occurs under continuous cooling conditions. Therefore, the equation (2.21) was modified for continuous cooling transformations [63-65]. By performing the calculations, Barandiaran and Colmenero [64] derived an equation for the critical cooling rate for glass formation, R_c is defined as;

$$\ln R = A - \frac{B}{(T_{\ell} - T_{xc})^2} \quad (2.22)$$

where R is the cooling rate, A and B are constants, T_{ℓ} is the offset temperature of fusion and T_{xc} is the onset temperature of solidification upon cooling at a rate R .

The undercooling $\Delta T_c (= T_{\ell} - T_{xc})$ varies with the cooling rate. When ΔT_c increases to infinity, no crystallization occurs and $A = \ln R_c$. The critical cooling rate, R_c will be obtained by an extrapolation of the fitting of experimental values with equation (2.22) [66]. Apart from these equations, R_c has also been estimated using different equations [67] based on the thermal behavior of the liquid solidifying into the glass.

2.6 PROPERTIES AND APPLICATIONS OF BULK METALLIC GLASSES

2.6.1 Properties of BMGs

The lack of crystallinity and lack of microstructural features such as grain boundaries are the main characteristics of metallic glasses. BMGs have superior properties compared to conventional metallic materials [68]. Some of these properties are stated in the following sections.

2.6.1.1 Mechanical Properties of BMGs

Metallic glasses are known for their outstanding mechanical strength. A comparison of mechanical strengths of various materials is indicated in Figure 2.7.

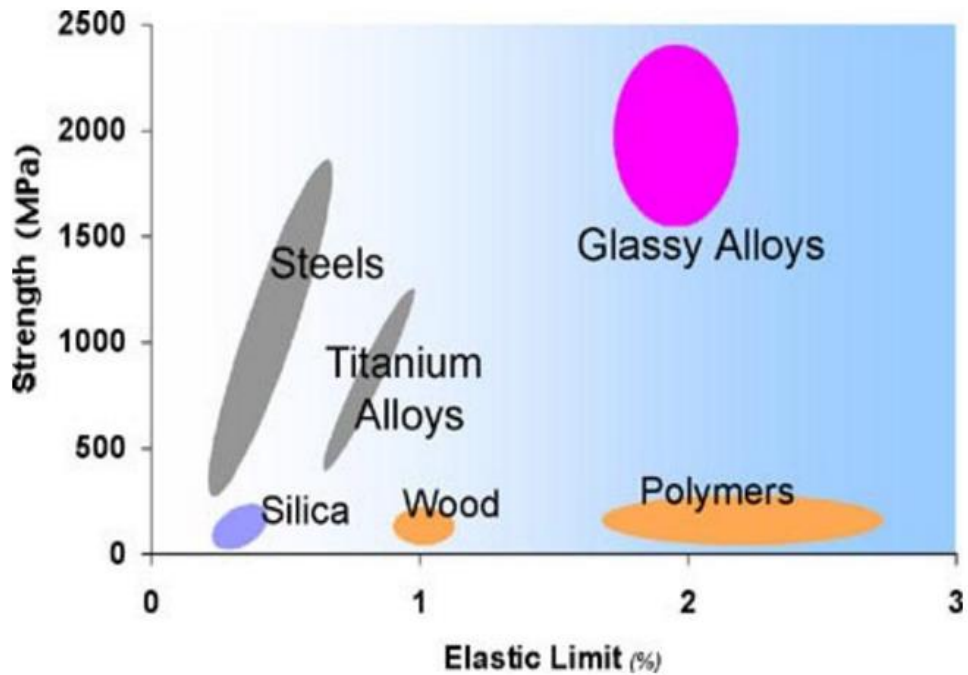


Figure 2.7 Typical strengths and elastic limits for various materials [69].

There is enough data available on BMGs for the quantitative comparison of their properties with conventional engineering materials. Figure 2.8 shows elastic limit σ_y and Young's Modulus E for over 1500 metals, alloys and metal-matrix composites. The ellipses enclose the range of values associated with given materials and material groups. The metallic glasses lie on the upper part of the populated region [68].

The contours shown in Figure 2.8 give the material indices σ_y/E and σ_y^2/E which are the yield strain and the resilience, a measure of the ability of a material to store elastic energy, respectively. According to Figure 2.8, metallic glasses have larger yield strength and storing more elastic energy per unit volume than other materials [68].

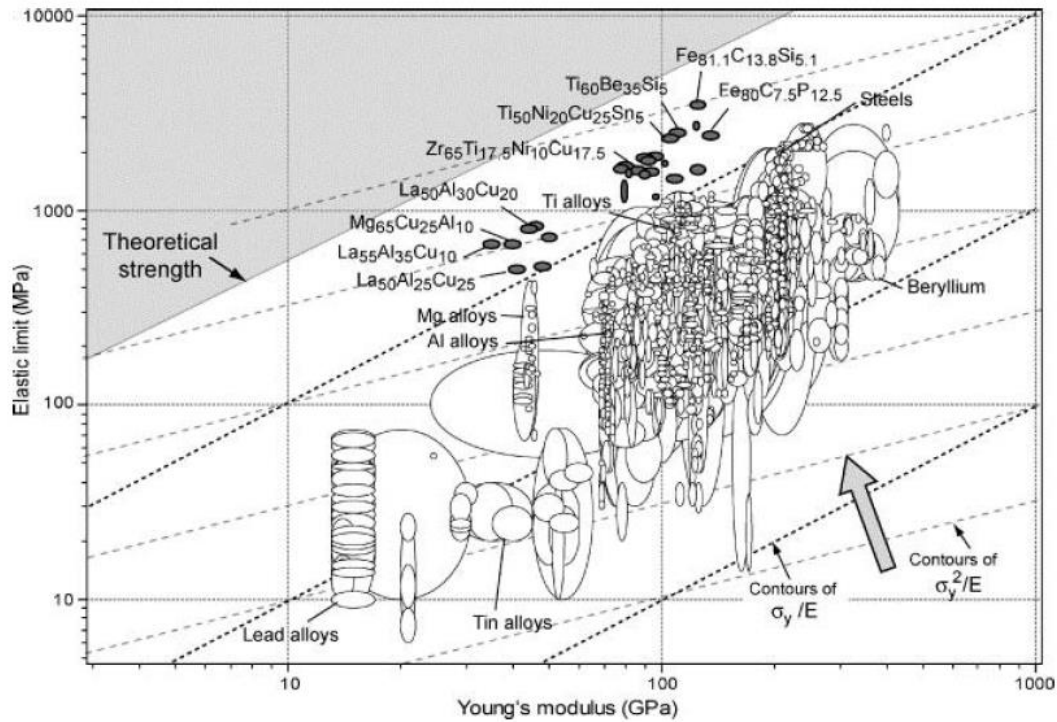


Figure 2.8 Elastic limit σ_y vs Young's Modulus E for over 1507 metals, alloys, metal matrix composites and metallic glasses. The contours show the yield strain σ_y/E and the resilience σ_y^2/E [68].

2.6.1.2 Magnetic Properties of BMGs

BMGs show different magnetic behavior. These are hard magnetic and soft magnetic. Magnetic properties are important for several applications in the electrical and electronic industries. But, the most important application is in transformer. Therefore, there are a lot of researches on magnetic properties of BMG alloys.

Inoue and Gook synthesized the first Fe-based ribbon alloy which is $\text{Fe}_{72}\text{Al}_5\text{Ga}_2\text{P}_{11}\text{C}_6\text{B}_4$ in 1995 [70]. This discovery was immediately followed with the synthesis of another Fe-based BMGs and a few investigations have also been reported on Co-based BMGs.

Some magnetic properties of melt-spun ribbons and bulk rods have minor differences such as magnetostriction and coercivity but saturation magnetization of the alloys is not any different whether measured on ribbons or bulk rods of different diameters [71,72].

2.6.1.2.1 Hard magnetic BMGs

Hard magnetic properties were obtained from Fe-Nd-B systems. Due to Nd-Fe clusters, coercivity is very high. Nd-Al-Fe systems which are only bulk form also show hard magnetic behavior. By changing diameter, coercivity can be changed [73-75].

2.6.1.2.2 Soft magnetic BMGs

The term soft means that the response of the magnetization to an applied field is high and this is a desirable property for such applications as transformers and inductors. Good soft magnetic properties of the material require high saturation magnetization, low coercivity, and high electrical resistivity. Inoue proposed that Fe-based amorphous alloys have good soft magnetic properties and Co-based amorphous alloys have also good soft magnetic properties and high stability of supercooled liquid against crystallization. The effect of annealing on soft magnetic properties was also investigated. By annealing, controlled formation of nanocrystals which are mainly α -(Fe,Co), soft magnetic properties of these alloy systems increased heavily [76-78]. In BMGs, alloying elements may also affect magnetic properties. Alloying additions may come down the saturation magnetization. If the alloying elements are maintained at a low level, the saturation magnetization can be increased but GFA of the alloy is decreased.

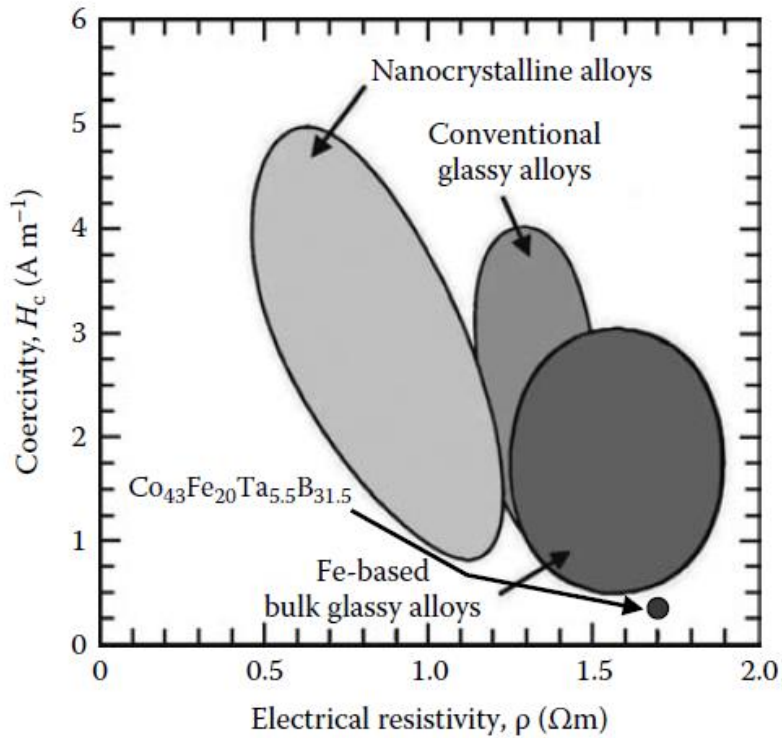


Figure 2.9 Coercivity H_c and electrical resistivity ρ of different types of magnetic alloys. Both the Co-based and Fe-based BMG alloys have the desirable combination of low coercivity and high electrical resistivity [24].

Effect of Alloying Elements

Different alloying elements are used to improve the GFA of alloys because good GFA provides producing rods with larger diameter. Co is one of the alloying elements. It is added from 0 to 20 at.% to Fe-based $Fe_{70-x}Co_xHf_5Mo_7B_{15}Y_3$ BMGs prepared from commercially pure raw materials. By copper mold casting technique, three-millimeter diameter rods were cast. With Co addition, GFA of the alloy increased and a fully glassy phase was obtained up to 12 at.% Co additions. However, Co addition was increased to 20 at.%, a crystalline phase appeared. This means that Co addition increased the GFA of the alloy in a limited composition range [79]. On the other hand, magnetic properties of the alloys showed a mixed trend. The fully glassy alloys showed a low coercivity (H_c) value in the range of 1–4

Oe. The saturation magnetization (B_s) decreased initially with Co addition, up to about 8 at.%, and then started to increase on further addition up to 20 at.%. The glass+crystal alloys showed higher values of both saturation magnetization and coercivity.

Addition of Co to Fe-based magnetic alloys is expected to decrease the B_s value because of the smaller magnetic moment of Co but at higher Co contents due to short-range order (SRO) in the glassy phase, B_s increased [80]. At 20 at.% Co, B_s was the highest because of the precipitation of α -(Fe,Co) phase which is strongly ferromagnetic phases. A similar phenomenon was also reported in FeCoNiZrMoB system [81].

Nb is another element added to Fe and Co-based alloys for improving their GFA [12-83]. Since Fe–B–Si alloys exhibit good soft magnetic properties, about 4 at.% Nb was added to the $(\text{Fe}_{1-x}\text{Ni}_x)_{0.75}\text{B}_{0.2}\text{Si}_{0.05}$ system [84]. While the GFA of the alloy improved, the saturation magnetization, B_s came down from 1.1 to 0.8 T.

Addition of Fe to Co-based BMG alloys improves not only the GFA but also the magnetic properties. In the $[(\text{Co}_{1-x}\text{Fe}_x)_{0.75}\text{B}_{0.2}\text{Si}_{0.05}]_{96}\text{Nb}_4$ system, B_s increased from 0.71 to 0.97 T with increasing Fe content from $x = 0.1$ to 0.4. The H_c value increased from 0.7 to 1.8 $\text{A}\cdot\text{m}^{-1}$ and the μ_e value decreased from 32,500 to 14,800. The large fractions of metalloid and nonmagnetic refractory elements can be responsible for the low saturation magnetization observed in the multicomponent alloys [85].

Effect of Annealing

Annealing of the fully glassy alloy enhance the soft magnetic properties of the alloys. Based on this concept, in the late 1980s FINEMET alloy was developed [86]. FINEMET alloys have low coercivity, low saturation magnetostriction, and low core losses in comparison with the fully glassy alloys.

Annealing of Fe–Si–B–M glassy alloys containing small amounts of up to 1.5 at.% of M (= Cu, Nb, Mo, W, Ta, etc.) have precipitation of fine α -Fe(Si, B) crystalline

particles. Cu and Fe have a positive heat of mixing, so they form Fe-rich and Cu-rich and Nb-rich regions. Fe-rich regions are the nuclei for the α -Fe. Cu-rich and Nb-rich regions do not crystallize due to their higher crystallization temperature. Therefore, the microstructure consists of fine α -Fe grains dispersed in a glassy matrix. This grains can be achieved only BMGs exhibit at least two stages of crystallization. In other words, BMGs which show a single stage of crystallization can not show such a microstructure. For example, Inoue et al. [87] added a small amount of Cu and slightly reduced the B content in the Fe–Si–B–Nb system to a composition of $\text{Fe}_{72.5}\text{Si}_{10}\text{B}_{12.5}\text{Nb}_4\text{Cu}_1$. Cu-free alloy showed one crystallization peak but the Cu-containing alloy showed multiple crystallization peaks. They annealed the glassy alloy at a temperature beyond the first crystallization peak, the BCC α -Fe precipitated out from the glassy matrix. The magnetic properties of such alloy are much better than those of the fully glassy alloy and these properties are also comparable with those of FINEMET and NANOPERM alloys.

Similar types of investigations have been reported for different Fe-based alloys. Chang et al. [84] reported that in the $(\text{Fe}_{0.75}\text{B}_{0.2}\text{Si}_{0.05})_{96}\text{Nb}_4$ glassy alloy crystallization takes place in one stage (Figure 2.10a). Shen and Inoue [72] reported that with the addition of 0.7 at.% Cu to an Fe–Co–Si–B–Nb alloy, crystallization takes place in two stages (Figure 2.10b).

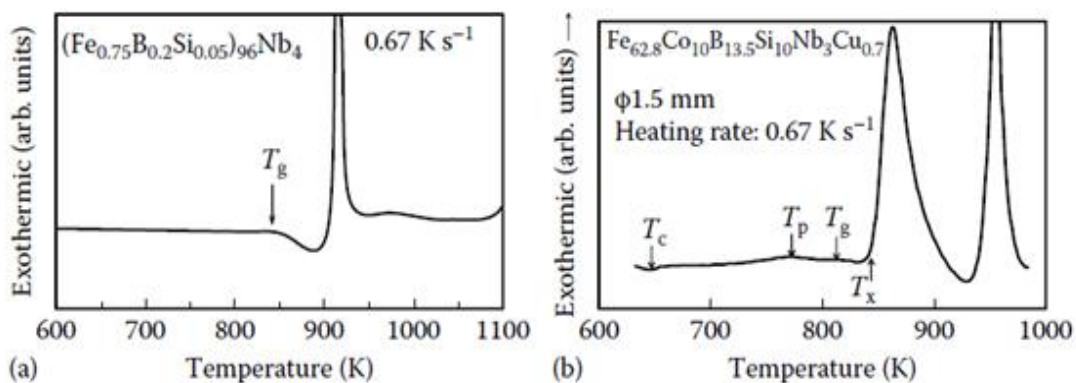


Figure 2.10 DSC curve of a) $(\text{Fe}_{0.75}\text{B}_{0.2}\text{Si}_{0.05})_{96}\text{Nb}_4$ alloy with one stage crystallization. b) $\text{Fe}_{62.8}\text{Co}_{10}\text{B}_{13.5}\text{Si}_{10}\text{Nb}_3\text{Cu}_{0.7}$ alloy with two stages crystallization.

This helps the precipitation of crystalline α -Fe phase in glassy matrix [24].

Table 2.2 Effect of Annealing on the Magnetic Properties of Different Glassy Alloys Systems [24].

Alloy	Sample	Annealing Conditions	Structure	I_s (T)	H_c (A m ⁻¹)	μ_0
(Fe _{0.75} Si _{0.1} B _{0.15}) ₉₆ Nb ₄	1.5 mm rod	—	Glassy	1.47	2.9	17,000
Fe _{72.5} Si ₁₀ B _{12.5} Nb ₄ Cu ₁	40 μ m ribbon	883 K/5 min	α -Fe in glass	1.23	0.7	80,000
Fe _{72.5} Si ₁₀ B _{12.5} Nb ₄ Cu ₁	0.5 mm rod	883 K/5 min	α -Fe in glass	1.21	1.8	32,000
Fe _{73.5} Si _{13.5} B ₉ Nb ₃ Cu ₁ (FINEMET)	18 μ m ribbon	823 K/1 h	α -Fe in glass	1.24	0.53	100,000
Fe ₈₆ Zr ₇ B ₆ Cu ₁ (NANOPERM)	21 μ m ribbon	873 K/1 h	α -Fe in glass	1.52	3.2	41,000

Nanocrystalline Alloys

In FINEMET and other alloys, the volume fraction of the nanocrystalline phase can reach almost 90%. Since a glassy precursor is a prerequisite to achieve this microstructure, Fe content should be as high as possible and the other metal and metalloid contents should be minimum. The presence of metals like Cu, Nb, Mo, W, and Ta is also necessary for obtaining large volume fraction of the nanocrystalline phase but these nonmagnetic metals can reduce saturation magnetization and they are quite expensive. To overcome these difficulties, Makino et al. [88,89] have developed novel Fe-based alloys which contain only metalloids. Their composition is Fe_{83.3-84.3}Si₄B₈P₃₋₄Cu_{0.7} and is based on the Fe₈₂Si₉B₉ alloy. In the modified alloy composition, P substitutes for B and Cu for Fe. The large concentration of Fe provides a high saturation magnetization and small amount of Cu is necessary for nanocrystallization. The absence of the metallic elements other than Fe shows that they are not expensive.

2.6.1.3 Chemical Properties of BMGs

Although it is not expected that local corrosion susceptibility of amorphous metals is lower than that of crystalline metals, the corrosion resistance of metallic glasses is

high. This is attributed to absence of defects which act as chemically active sites [90].

Chemical reactivity of the amorphous metals can be changed by controlling the alloy compositions. The compositional dependence of the chemical corrosion behaviors is shown in Figure 2.11. According to graph, the corrosion rate of the amorphous Fe-P-C alloy without Cr content is much higher than that of the crystalline pure Fe by several orders of magnitude. However, the addition of Cr to the amorphous Fe-P-C alloy reduces the corrosion rate drastically [90].

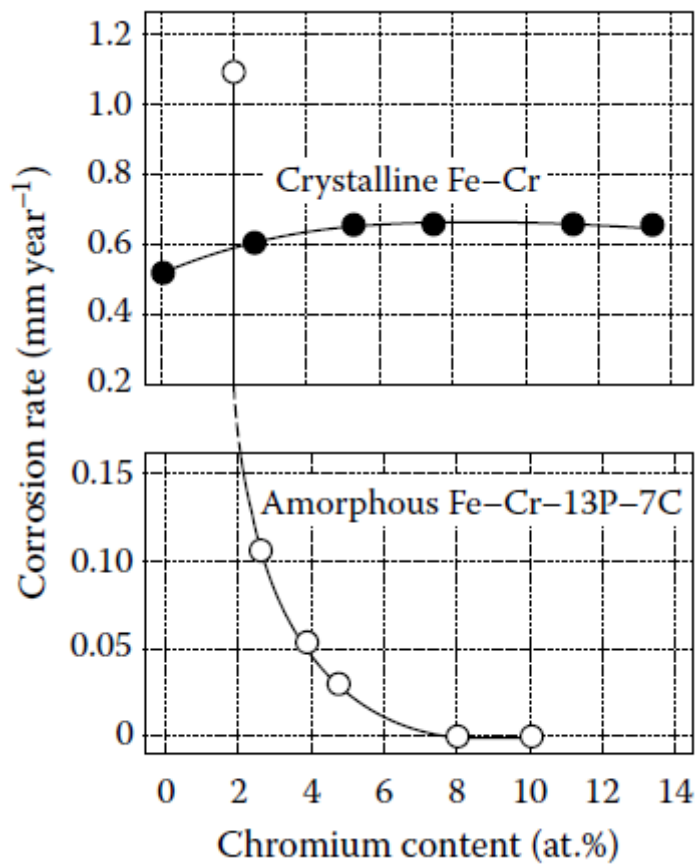


Figure 2.11 Comparison of corrosion rates of amorphous Fe-Cr-13P-7C alloys and crystalline Fe-Cr alloys in 1N NaCl at 30°C [90].

The catalytic properties of BMGs are also important. They showed higher stability compared to crystalline alloys. This property and other unique properties make them as attractive materials in catalysis. They can be used as catalyst precursors and several efficient catalysts can be prepared by various treatments of the metallic glasses [90].

2.6.2 Applications of BMGs

BMGs have a combination of a lot of properties. They exhibit excellent mechanical properties, very high strength, large elastic elongations, low Young's modulus, good corrosion resistance, and the ability to be easily formed in the supercooled liquid state. The soft magnetic properties of BMGs are also one of the properties. They have a low coercivity and very high permeability at high frequencies. The saturation magnetization can also be adjusted by optimizing the chemical composition. Thus, BMGs have large application area [24, 91]. Table 2.2 shows some of these areas.

Table 2.3 Application areas of BMGs [91].

1. Structural	14. Information Data Storage
2. Sensor	15. Biomedical
3. Precision Machinery	16. Medical Instrument
4. Optical	17. Fuel- Cell Separator
5. Ornamental	
6. Spring	
7. Sporting Goods	
8. Wear - Resistant Coating	
9. Precision Nozzle	
10. Corrosion Resistant	
11. Magnetic	
12. Micro- Technology	
13. Nano- Technology	

CHAPTER 3

EXPERIMENTAL PROCEDURE

3.1 RAW MATERIALS

In this thesis, high purity elements were obtained from Alfa Aesar. Purity grades of alloying elements were given in Table 3.1. The precision of the composition and amount of the impurities are important for BMGs. Thus, all constituent elements were weighted up to fourth decimal.

Table 3.1 Purity Grades of Alloying Elements

Element	Grade (%)
Fe	99.97
Co	99.9
Nb	99.6
B	99.5
Si	98.5
Cu	99.9

3.2 FABRICATION OF SAMPLES

Sample was produced by first arc melting and then suction casting methods. After that, it was cut by using wire erosion machine.

3.2.1 Arc Melting

The alloy was prepared by Edmund Buhler GmbH Arc Melter device using a water-cooled copper hearth (Fig. 3.1) and non-consumable tungsten electrode under high purity argon atmosphere. During melting process, Zr was used as an oxygen getter. In addition, rotary and diffusion pumps can provide an ideal and oxygen free melting atmosphere which is vital for avoid the detrimental effect of oxygen on GFA of metallic glasses. The stainless steel chamber is evacuated up to 10^{-5} mbar and rinsed with high purity argon gas prior to every casting. This process removes any undesired gas and is repeated three times just to ensure the attainment of perfect melting conditions. The alloy was melted four times and each time it was flipped for complete homogeneity.



Figure 3.1 Copper heart and arc melting.

3.2.2 Rapid Solidification by Suction Casting

Suction casting was used to produce sample and to achieve high cooling rates necessary for glass formation in FeCoBSiNbCu alloy. The suction casting unit is equipped into Edmund Buhler GmbH Arc Melting device. The same procedure in arc melting was followed for the casting in terms of oxygen free atmosphere and homogenization of the alloys. Finally, alloy was produced in the form of cylindrical rods with a diameter of 3 mm and length of 150 mm by suction casting into a water cooled copper mold (Fig. 3.2).



Figure 3.2 Suction casting unit and rod shaped specimen.

3.3 CHARACTERIZATION OF SAMPLES

In this study, various characterization tools were used to get detailed information about microstructural evolution, precipitation and crystallization phenomena, thermal characteristics, magnetic properties and hardness of sample.

3.3.1 X-Ray Diffractometry

Structural characterization of sample was carried out by X Ray Diffraction (XRD) using Bruker D8 Advance. Cu-K α radiation of wavelength 1.540562 Å and diffraction angle range $2\theta = 5^\circ - 110^\circ$ with scanning rate of $2^\circ/\text{min}$ were used. XRD patterns were analyzed by using qualitative analysis software.

3.3.2 Scanning Electron Microscopy

Microstructural investigations were done by using FEI Nova Nano430 Scanning Electron Microscope (SEM) and the composition of sample was verified by Energy Dispersive Spectroscopy (EDS). Both the back-scattered mode and secondary electron mode were used. In back-scattered mode, existence of phases were investigated. In secondary electron mode, differences between solidification microstructures were determined.

3.3.3 Differential Scanning Calorimetry

Isochronal thermal analyses of sample were performed by Differential Scanning Calorimeter (DSC) with Setaram Setsys 16/18 (Fig. 3.3) under argon atmosphere. Isothermal annealing processes were performed by Setaram DSC131 under argon atmosphere. DSC was used to observe thermal behaviour and material's response to different heating and cooling rates as well as critical cooling rate of the sample. DSC instrument measures heat release or absorption rate as a function of temperature.



Figure 3.3 DSC used in isochronal thermal analysis.

3.3.4 Vibrating Sample Magnetometry

Magnetic monitoring of sample was carried out using an ADE Magnetics EV/9 Vibrating Sample Magnetometer (VSM) (Fig. 3.4) under a maximum applied field of 18000 Oe. Measurements were performed at room temperature.



Figure 3.4 VSM used for magnetic measurements.

3.3.5 Microhardness Measurement

Vickers microhardness measurement of sample was done by Shimadzu Microhardness Tester with a load of 9.8 N. The measurements were performed on both as cast and heat treated samples.

3.3.6 Four Point Probe Measurement

Electrical resistivity of sample was measured by four point probe method. In this method, current passes through two outer probes and voltage is measured through the inner probes. The apparatus used is Jandel universal with 1 mm probe spacing. Current is measured by Keithley 238 Current Source measure unit and voltage is measured by Keithley 2182A Nanovoltmeter.

CHAPTER 4

RESULTS AND DISCUSSIONS

4.1 PRODUCTION AND CHARACTERIZATION OF AS CAST ALLOYS

Production of As Cast Alloy

(Fe₃₆Co₃₆B_{19.2}Si_{4.8}Nb₄)_{99.25}Cu_{0.75} system is worth to study due to its high GFA, as it is compositionally derivative of Finemet alloys and good soft magnetic properties as well as being a precursor for bulk nanocrystalline alloys. This study aims producing a BMG to study the glass formation phenomenon and combining those results with nanocrystallization of the BMG yielding a bulk nanocrystal alloy showing good soft magnetic properties. For producing (Fe₃₆Co₃₆B_{19.2}Si_{4.8}Nb₄)_{99.25}Cu_{0.75} BMG, the non equilibrium condition which is necessary was reached by arc melting and suction casting. (Fe₃₆Co₃₆B_{19.2}Si_{4.8}Nb₄)_{99.25}Cu_{0.75} alloy was produced by first arc melting and then suction casting into copper mold in the form of cylindrical rod with diameter of 3 mm and length of 150 mm in argon atmosphere. Produced specimen was cut by wire erosion 3 mm to 3 mm. A schematic drawing of a slice is given in Figure 4.1.

Characterization of As Cast Alloy

The parts of the specimen contacted the copper mold cooled faster from other parts. Furthermore, through the bottom of the specimen, cooling rate increases and finally at the bottom of the sample contacted the water-cooled copper hearth of the arc melting device has the highest cooling rate. Therefore, different microstructural

features can be observed along the specimen. For investigating these differences, different parts of sample were examined. Sample was numbered from 1 to 12 from its bottom. In this way, region 1 has the highest cooling rate and region 12 has the lowest cooling rate. These numbered regions were investigated by XRD and SEM.

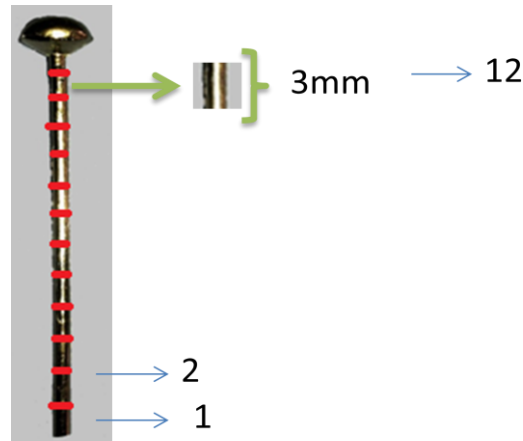


Figure 4.1 Cutting of the produced rod shaped bulk glassy $(\text{Fe}_{36}\text{Co}_{36}\text{B}_{19.2}\text{Si}_{4.8}\text{Nb}_4)_{99.25}\text{Cu}_{0.75}$ alloy.

According to XRD results of as cast samples given in Figure 4.2, presence of a broad diffuse peak indicating amorphous structure confirms that an glassy rod with critical diameter of 3 mm can be produced for $(\text{Fe}_{36}\text{Co}_{36}\text{B}_{19.2}\text{Si}_{4.8}\text{Nb}_4)_{99.25}\text{Cu}_{0.75}$ alloy. It was found that a fully amorphous structure exists in upper sections of the rod, a partially amorphous structure exists in down sections of the rod due to short range order or medium range order in the structure.

SEM micrograph of the alloys was given in Figure 4.3. Formation of fully glassy $(\text{Fe}_{36}\text{Co}_{36}\text{B}_{19.2}\text{Si}_{4.8}\text{Nb}_4)_{99.25}\text{Cu}_{0.75}$ BMGs are characterized by featureless electron micrographs. Both back scattered and secondary electron modes were used. Secondary electron mode was used for showing differences between solidification microstructures. Back-scattered mode was used for examining the different phase compositions. In addition, compositional homogeneity in amorphous matrix can be seen from EDS analysis provided in Appendix A, Figure 1.

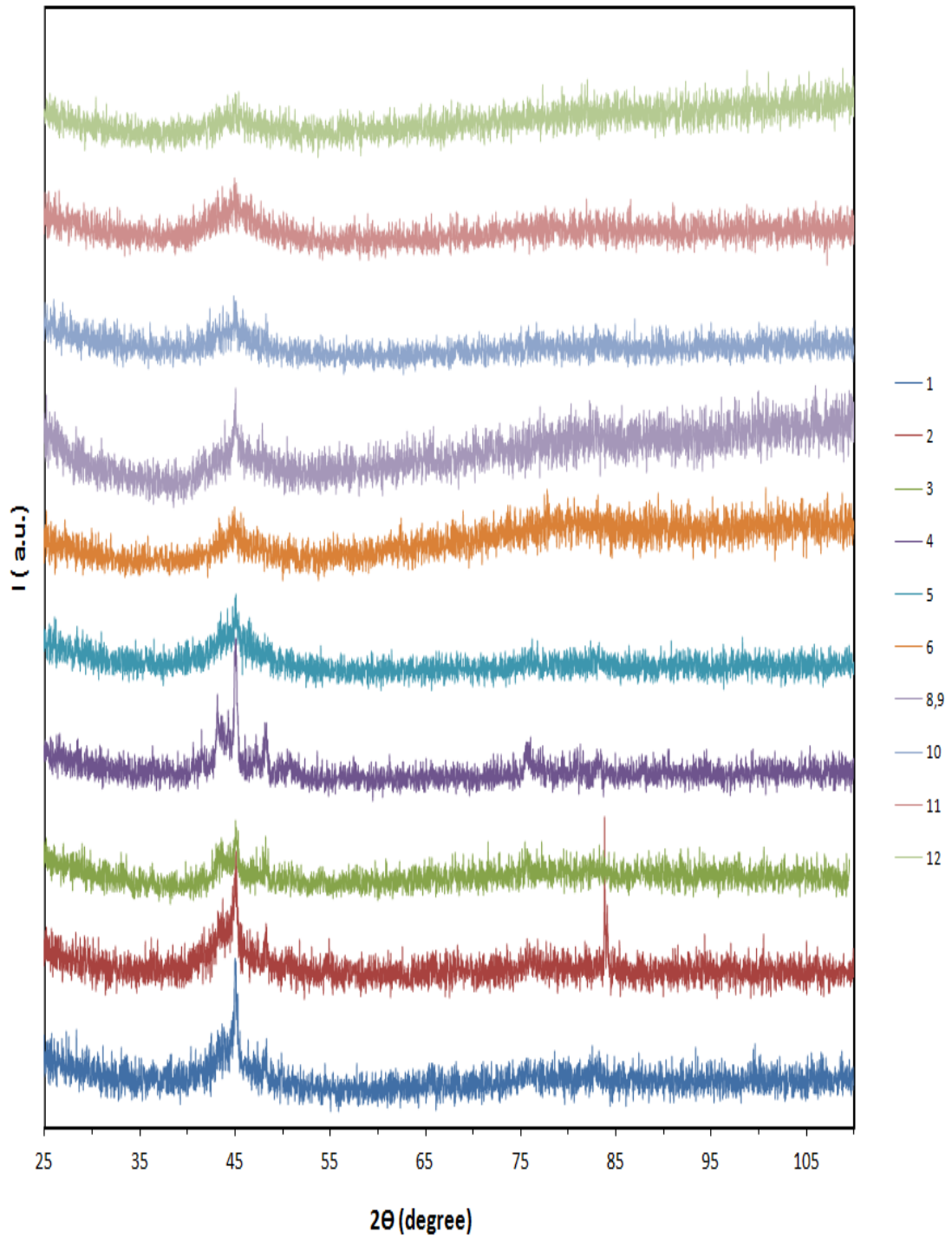


Figure 4.2 XRD patterns of as cast samples from different parts of the bulk glassy $(\text{Fe}_{36}\text{Co}_{36}\text{B}_{19.2}\text{Si}_{4.8}\text{Nb}_4)_{99.25}\text{Cu}_{0.75}$ alloy.

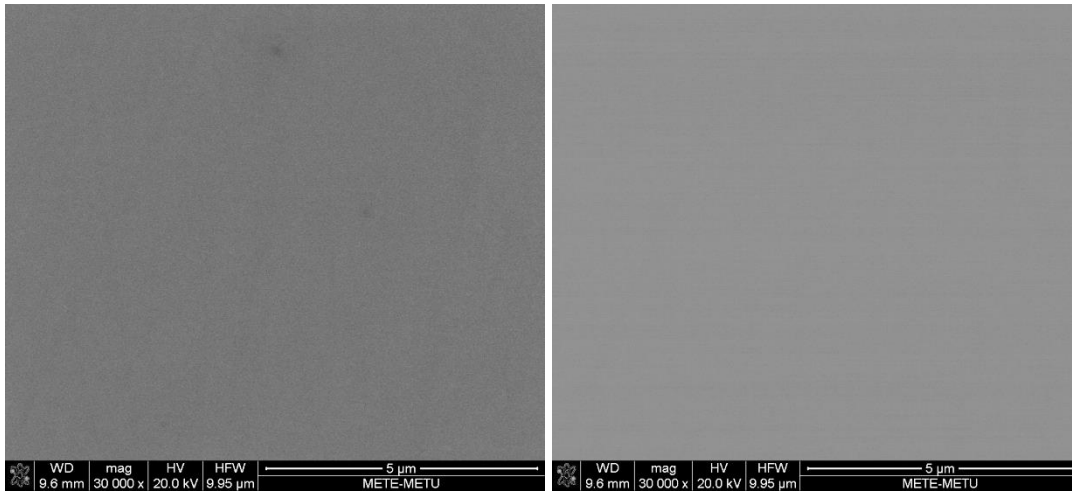


Figure 4.3 Secondary electron image (left) and back scattered electron image (right) of the bulk amorphous $(\text{Fe}_{36}\text{Co}_{36}\text{B}_{19.2}\text{Si}_{4.8}\text{Nb}_4)_{99.25}\text{Cu}_{0.75}$ alloy.

For producing $(\text{Fe}_{36}\text{Co}_{36}\text{B}_{19.2}\text{Si}_{4.8}\text{Nb}_4)_{99.25}\text{Cu}_{0.75}$ alloy, highly pure elements were melted more than once to obtain a homogeneous structure. For investigating this homogeneity, the head part of the specimen shown in Figure 4.4 was investigated by XRD and SEM. XRD results of the sample was given in Figure 4.5 and precipitated phases can be seen from these results.

SEM micrograph of the sample was shown in Figure 4.6. First of all, as-polished specimen was investigated by using backscattered electrons. In this way, dendrites can be seen clearly. These dendrites have three different areas. These are stated as dark, gray and light. According to EDS analysis given in Appendix A, Figure 2, in dark areas are composed of only Fe-Co. When this result was compared with the XRD results, it can be said that the dark contrasted phase in these regions is mainly $\alpha\text{-Fe}(\text{Co})$. In gray and light areas are composed of mostly Fe-Co, but they also include Nb and Si. For these areas, although Fe and Co quantities are approximately equal, Si and Nb quantities are quite different. EDSs of light and gray areas were also given in Appendix A, Figure 3 and 4. Figure 4.7 shows these dendrites after etching.

SEM micrograph of inner part of the same sample was shown in Figure 4.6. In this part, eutectic like structure can be observed. Moving to the more slowly cooled regions where the cooling rate was smaller the eutectic structure started to be observed. This implies that the eutectic reaction was suppressed as the cooling rate was increased. EDS of the eutectic like structure was given in Appendix A, Figure 5-7. Figure 4.8 shows the eutectics after etching.

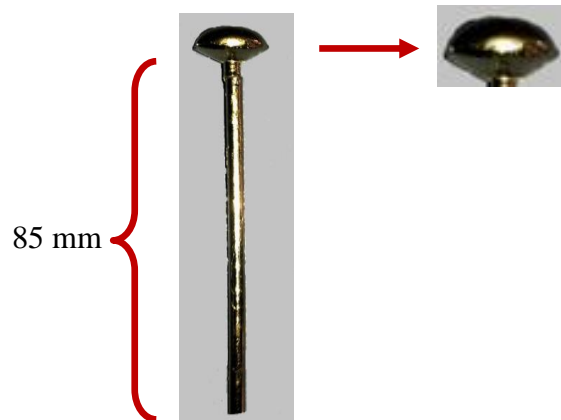


Figure 4.4 Investigated head part of the bulk glassy $(\text{Fe}_{36}\text{Co}_{36}\text{B}_{19.2}\text{Si}_{4.8}\text{Nb}_4)_{99.25}\text{Cu}_{0.75}$ alloy for homogeneity.

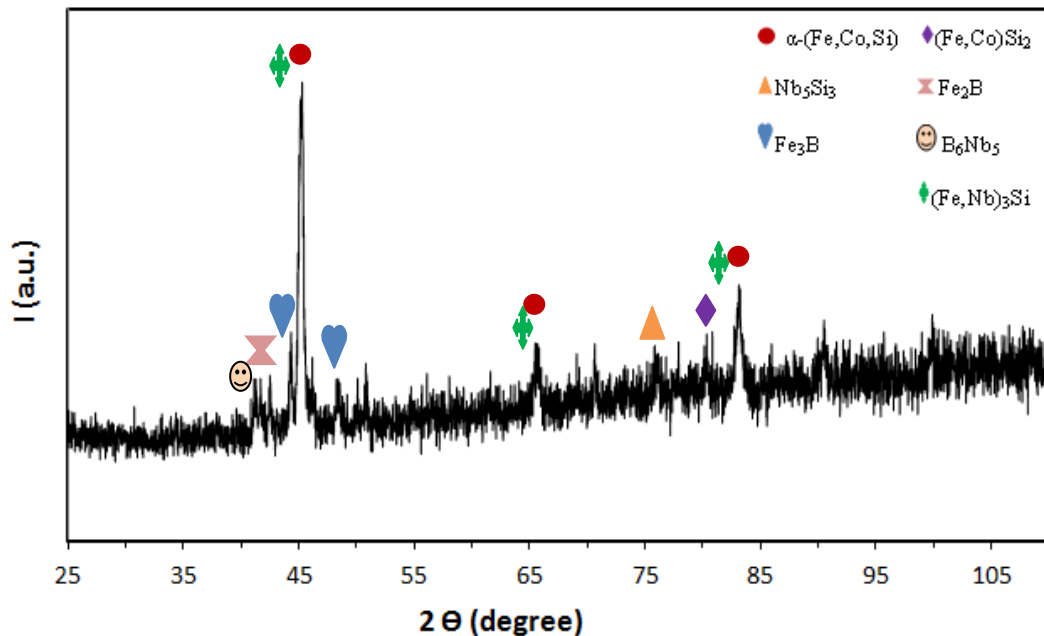


Figure 4.5 XRD pattern of the head part of bulk glassy $(\text{Fe}_{36}\text{Co}_{36}\text{B}_{19.2}\text{Si}_{4.8}\text{Nb}_4)_{99.25}\text{Cu}_{0.75}$ alloy shown in Figure 4.4.

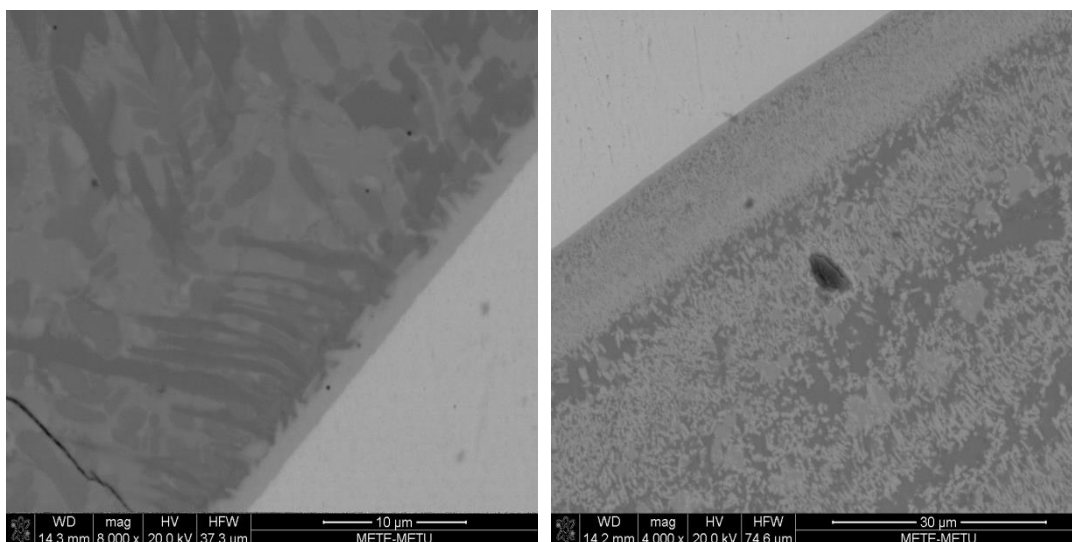


Figure 4.6 Back scattered electron image of dendrites (left) and eutectics (right) the head part of bulk glassy $(\text{Fe}_{36}\text{Co}_{36}\text{B}_{19.2}\text{Si}_{4.8}\text{Nb}_4)_{99.25}\text{Cu}_{0.75}$ alloy.

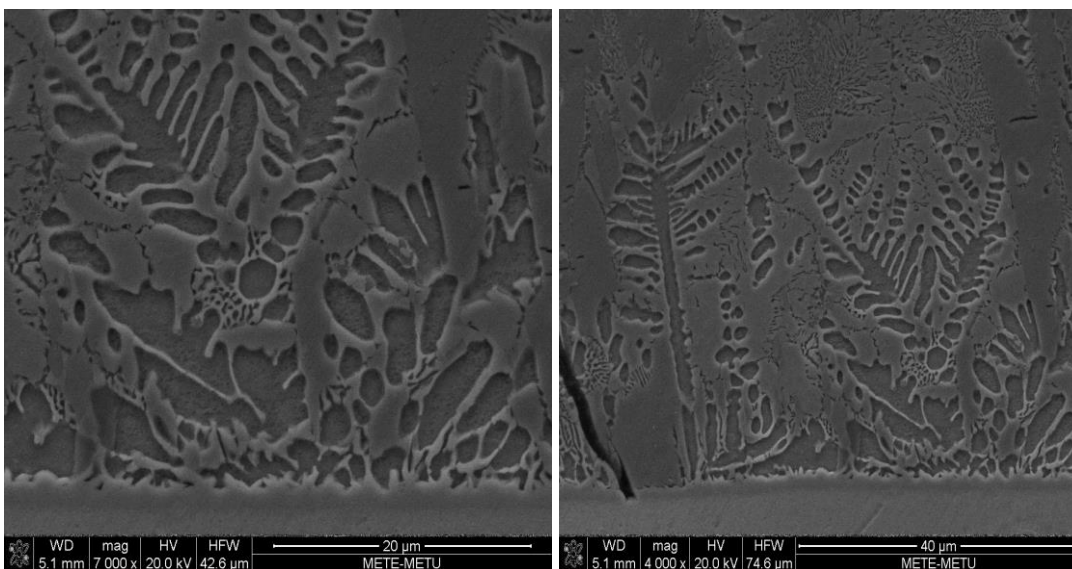


Figure 4.7 Secondary electron image of dendrites after etching of the head part of bulk glassy $(\text{Fe}_{36}\text{Co}_{36}\text{B}_{19.2}\text{Si}_{4.8}\text{Nb}_4)_{99.25}\text{Cu}_{0.75}$ alloy.

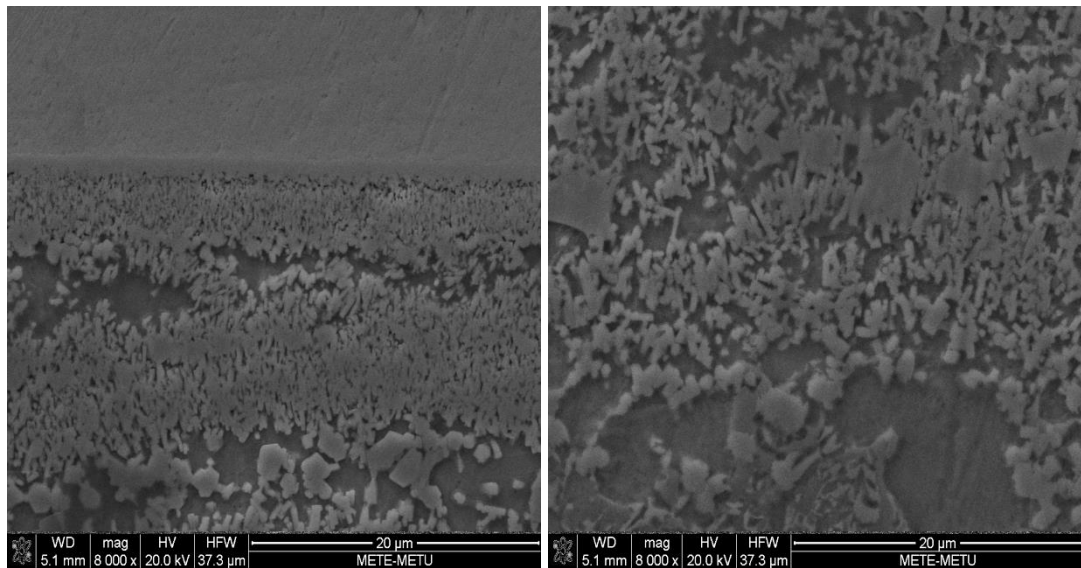


Figure 4.8 Secondary electron image of eutectic like structures after etching of the head part of bulk glassy $(\text{Fe}_{36}\text{Co}_{36}\text{B}_{19.2}\text{Si}_{4.8}\text{Nb}_4)_{99.25}\text{Cu}_{0.75}$ alloy.

In Figure 4.6, there is a white region in both images of dendrites and eutectics. According to EDS results given in Appendix A, Figure 8, this region is almost completely Nb. In EDS analysis, B content is not detected exactly because it is a light element. Thus, when this results compared with the XRD results, this phase can be B_6Nb_5 .

Thermal Analysis

The amorphous nature of the alloy was further confirmed by thermal analysis. DSC trace of the specimen given in Figure 4.9 exhibits a typical glass transition followed by three exothermic crystallization reactions. The glass transition temperature is 509 °C and consecutive exothermic peaks are attributed to the crystallization events and denoted as T_{x1} , T_{x2} and T_{x3} . This multistage crystallization process can yield nanoscale crystalline particles distributed in the amorphous matrix. Table 4.1 shows glass transition and exothermic crystallization temperatures values.

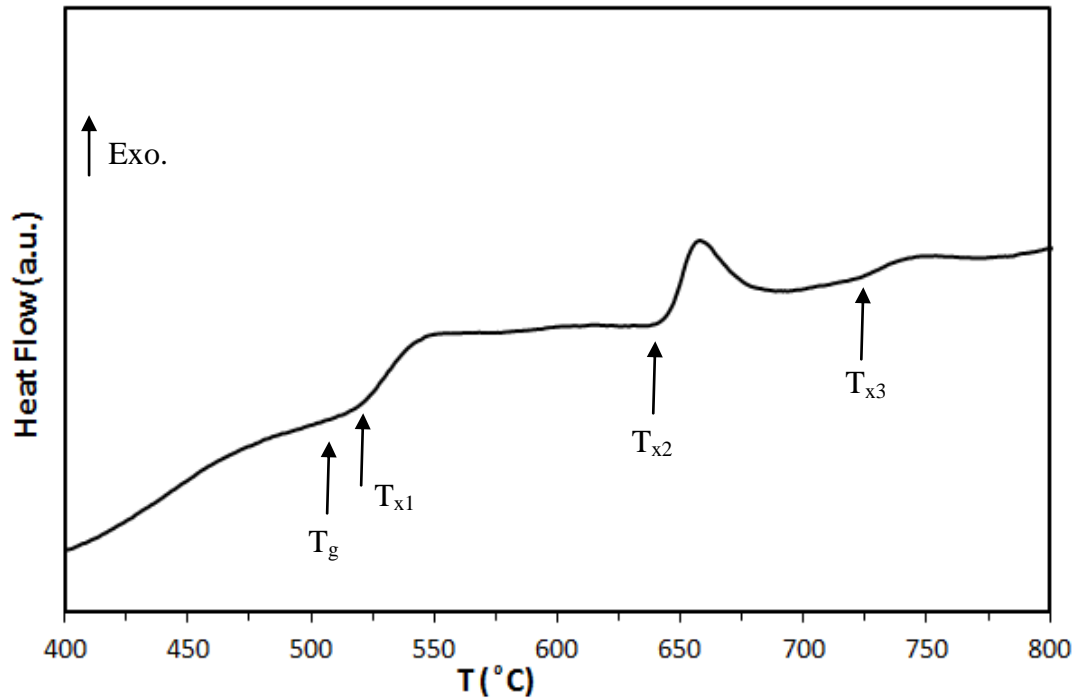


Figure 4.9 DSC trace of the bulk glassy $(\text{Fe}_{36}\text{Co}_{36}\text{B}_{19.2}\text{Si}_{4.8}\text{Nb}_4)_{99.25}\text{Cu}_{0.75}$ alloy on heating at 40 °C/min rate.

Table 4.1 Glass transition and crystallization temperatures of the bulk glassy $(\text{Fe}_{36}\text{Co}_{36}\text{B}_{19.2}\text{Si}_{4.8}\text{Nb}_4)_{99.25}\text{Cu}_{0.75}$ alloy obtained from DSC pattern.

T_g	T_{x1}	T_{x2}	T_{x3}
509 °C	520 °C	645 °C	724 °C

DSC analyses conducted with two subsequent heating and cooling paths. The 1st heating path gives information about the glass transition (T_g) and following crystallization (T_x) of the bulk glassy alloy. The cooling region of 1st path can not give exact results due to strong local order preserving even in the molten state thus, 2nd cooling path was used for determining several transition temperatures such as liquidus; T_l , eutectic; T_e , allotropic transformation; $T_{\gamma-\alpha}$ and order-disorder transition; T_{odt} temperatures. Figures 4.10 shows these heating and cooling paths.

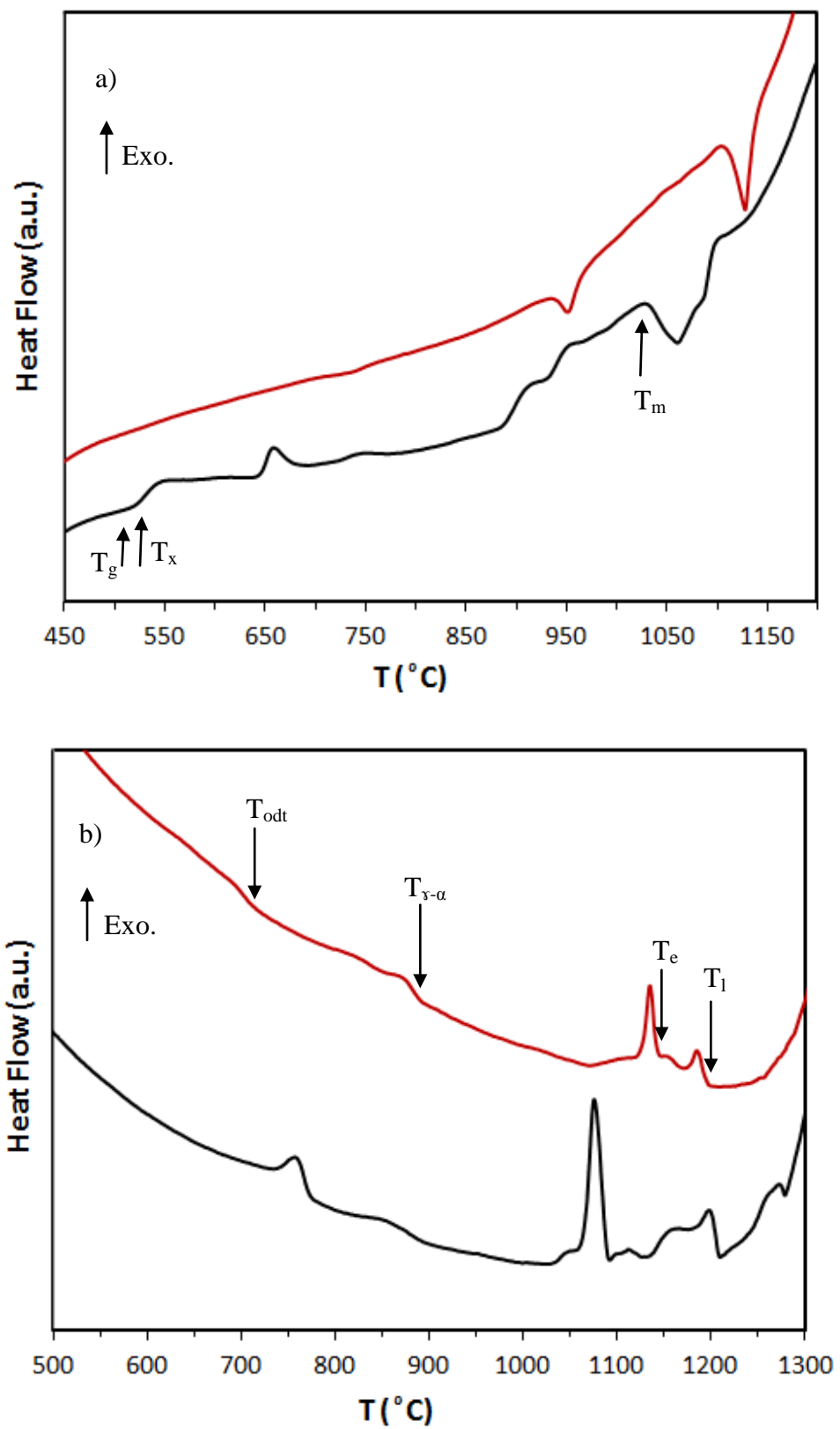


Figure 4.10 Comparison of 1st (black) and 2nd (red) a) heating paths b) cooling paths of bulk glassy $(\text{Fe}_{36}\text{Co}_{36}\text{B}_{19.2}\text{Si}_{4.8}\text{Nb}_4)_{99.25}\text{Cu}_{0.75}$ alloy at 40 °C/min.

Transition temperatures obtained from DSC patterns of the bulk glassy $(\text{Fe}_{36}\text{Co}_{36}\text{B}_{19.2}\text{Si}_{4.8}\text{Nb}_4)_{99.25}\text{Cu}_{0.75}$ alloy was shown in Table 4.2.

Table 4.2 Transition temperatures of the bulk glassy

$(\text{Fe}_{36}\text{Co}_{36}\text{B}_{19.2}\text{Si}_{4.8}\text{Nb}_4)_{99.25}\text{Cu}_{0.75}$ alloy obtained from DSC pattern at 40 °C/min.

T_g	T_x	T_m	T_{odt}	$T_{\gamma-\alpha}$	T_e	T_1
509 °C	520 °C	1030 °C	675 °C	851 °C	1127 °C	1176 °C

The solidification behavior of the $(\text{Fe}_{36}\text{Co}_{36}\text{B}_{19.2}\text{Si}_{4.8}\text{Nb}_4)_{99.25}\text{Cu}_{0.75}$ alloy shows a near eutectic like solidification and T_1 and T_e temperatures are too close. Following the eutectic reaction, as the alloy is further cooled down, two exothermic reactions occur in the alloy. The first one can be attributed to $\gamma\text{-Fe}(\text{Co}) \rightarrow \alpha\text{-Fe}(\text{Co})$ allotropic phase transformation. After $\gamma \rightarrow \alpha$ transformation, the disordered A2 phase is expected to go through an $\text{A2} \rightarrow \text{B2}$ order disorder transition with further cooling. This transition occurs when alloy has same amount of Fe and Co. Fe and Co have wide solubilities both in high temperature γ (FCC) and low temperature α (BCC) phases [92] and α is assumed to be a B2-type intermetallic compound. Allotropic phase transformation $\gamma\text{-Fe}(\text{Co}) \rightarrow \alpha\text{-Fe}(\text{Co})$ peak [92] shows the presence of a BCC Fe(Co) phase and this phase is known to yield the highest saturation magnetization of any material [92]. If these Fe(Co) crystals can be stabilized in nano-scale, the alloy shows excellent soft magnetic properties.

Figure 4.10 also shows the comparison of 1st and 2nd heating paths and the comparison of 1st and 2nd cooling paths.

Head part of the bulk glassy $(\text{Fe}_{36}\text{Co}_{36}\text{B}_{19.2}\text{Si}_{4.8}\text{Nb}_4)_{99.25}\text{Cu}_{0.75}$ rod alloy shown in Figure 4.4 was also investigated by DSC. Figure 4.11 shows this DSC pattern. According to XRD results of this part of the specimen, sample has crystalline phases. Thus, DSC traces of the head part of the bulk glassy rod $(\text{Fe}_{36}\text{Co}_{36}\text{B}_{19.2}\text{Si}_{4.8}\text{Nb}_4)_{99.25}\text{Cu}_{0.75}$ alloy have some differences from the DSC traces of rod samples. While for rod samples 1st and 2nd paths have some differences, for head part of the specimen these paths are almost same because this part of the alloy has crystalline phases. 1st heating behavior of this part revealed no significant information other than two-fold reactions which can be attributed to eutectic reaction and primary phase precipitation. On the other hand, in rod samples, 1st heating path has glass transition temperatures followed by three exothermic reactions. 2nd heating path is same for both parts because alloy became fully crystalline structure.

The cooling curve of the 2nd path of rod sample shows that the alloy approached the eutectic composition since T_e and T_1 became observable and close to each other; indicating that the composition is near eutectic. The peak in between these two points might have occurred due to several reasons like; a peritectic reaction is followed by a eutectic reaction upon cooling, or a separate unknown phase like Fe_{23}B_6 precipitates in between. On the contrary, for 2nd cooling path of the head part of the sample T_e and T_1 are far from each other and when 1st cooling paths are compared, they showed different patterns.

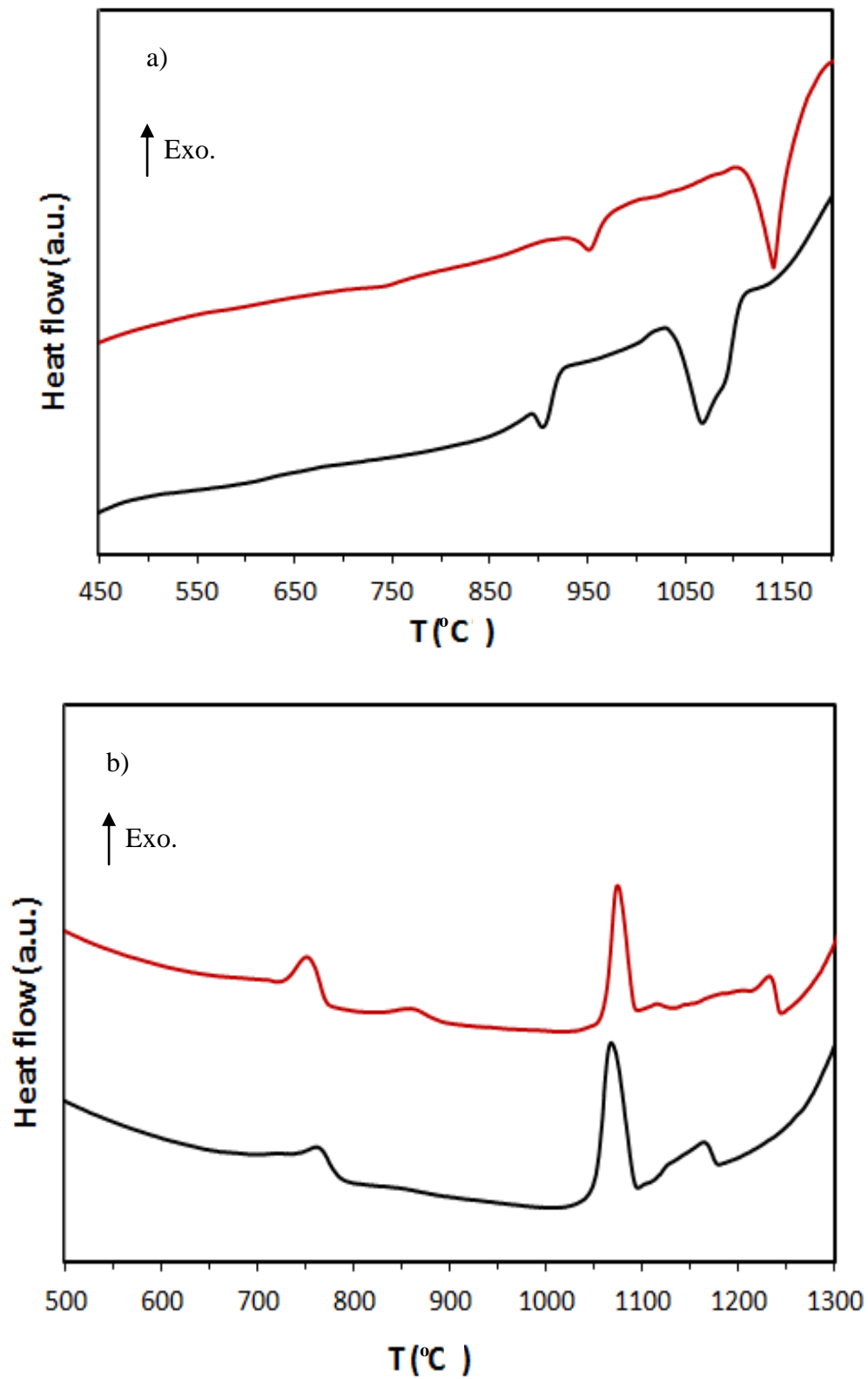


Figure 4.11 Comparison of 1st (black) and 2nd (red) a)heating paths b)cooling paths of head part of the bulk glassy $(\text{Fe}_{36}\text{Co}_{36}\text{B}_{19.2}\text{Si}_{4.8}\text{Nb}_4)_{99.25}\text{Cu}_{0.75}$ alloy at 40 °C/min.

Magnetic Measurements

The soft magnetic performances of the alloys are important for their promising uses in different areas. The desired properties for a soft magnet can be described as a saturation induction (B_s) above 1 T and coercivity (H_c) below 1000 A/m (~13 Oe). The room temperature (RT) saturation magnetization and coercivity of $(\text{Fe}_{36}\text{Co}_{36}\text{B}_{19.2}\text{Si}_{4.8}\text{Nb}_4)_{99.25}\text{Cu}_{0.75}$ BMG were measured as 1.10 T and 3.214 Oe (1 Oe = 79.58 A/m) respectively and hysteresis (B-H) loop was given in Figure 4.12, proving that this alloy is a good soft magnet. The inset shows the region of B-H loop near zero field strength, clarifies the low coercivity. Magnetic properties of the current $(\text{Fe}_{36}\text{Co}_{36}\text{B}_{19.2}\text{Si}_{4.8}\text{Nb}_4)_{99.25}\text{Cu}_{0.75}$ BMG produced by suction casting are much better than the similar ones reported in the original work [93] in which; e.g., B_s was reported as 0.84 T.

Electrical Resistivity Measurements

Electrical resistivity of $(\text{Fe}_{36}\text{Co}_{36}\text{B}_{19.2}\text{Si}_{4.8}\text{Nb}_4)_{99.25}\text{Cu}_{0.75}$ BMG was measured by four point probe method. The desired values for good electrical resistivity is between 10^{-6} and 1.5×10^{-6} Ωm . The room temperature electrical resistivity and conductivity of $(\text{Fe}_{36}\text{Co}_{36}\text{B}_{19.2}\text{Si}_{4.8}\text{Nb}_4)_{99.25}\text{Cu}_{0.75}$ BMG were measured as $\rho = 1.88 \times 10^{-6}$ Ωm and $\sigma = 5.32 \times 10^5$ S/m respectively and related graphs were given in Figure 4.13, proving that this alloy has a high electrical resistivity.

According to magnetic and electrical resistivity measurements, it can be said that it is a good candidate for transformers. In transformers, sources of energy loss are Eddy current and Hysteresis. For eliminating these losses, materials which have high resistivity and low coercivity must be used. Materials with high resistivity oppose Eddy current, so dissipation of energy as heat can be minimized and low coercivity provides low Hysteresis loss.

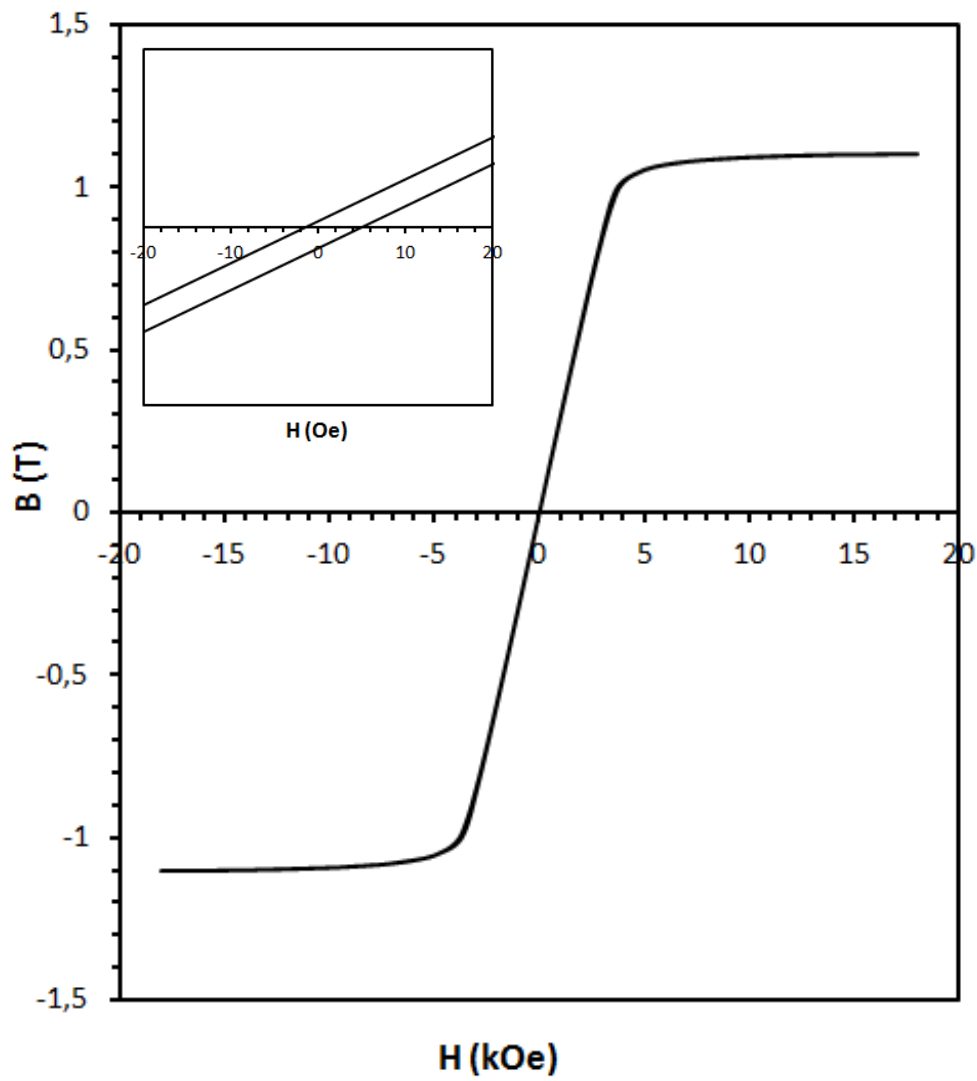


Figure 4.12 Hysteresis loop of the bulk glassy $(\text{Fe}_{36}\text{Co}_{36}\text{B}_{19.2}\text{Si}_{4.8}\text{Nb}_4)_{99.25}\text{Cu}_{0.75}$ alloy. Inset shows the region around zero field strength.

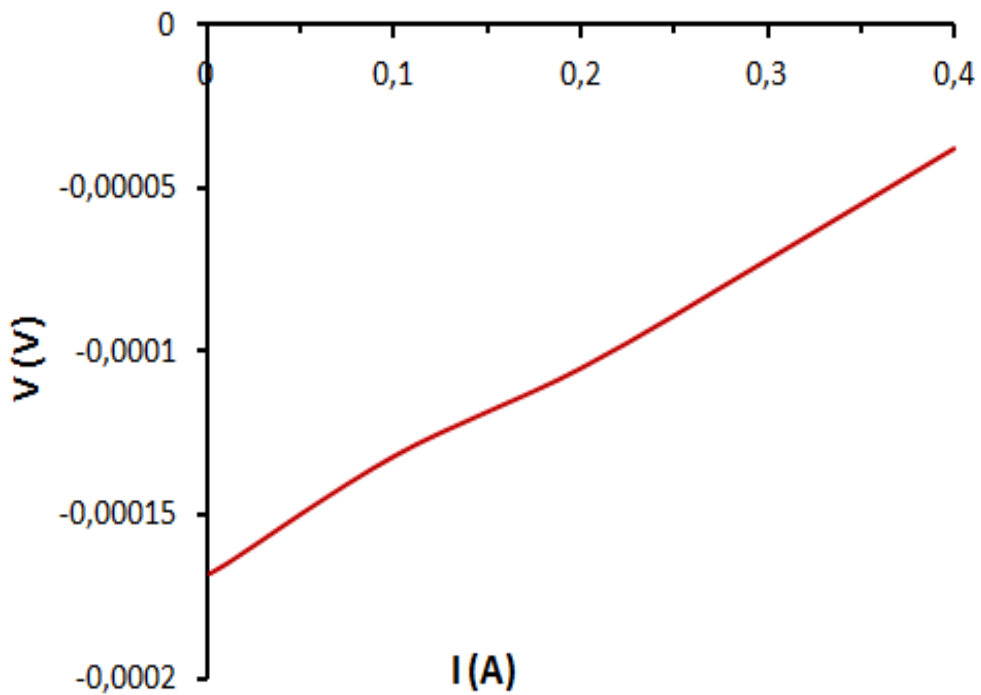
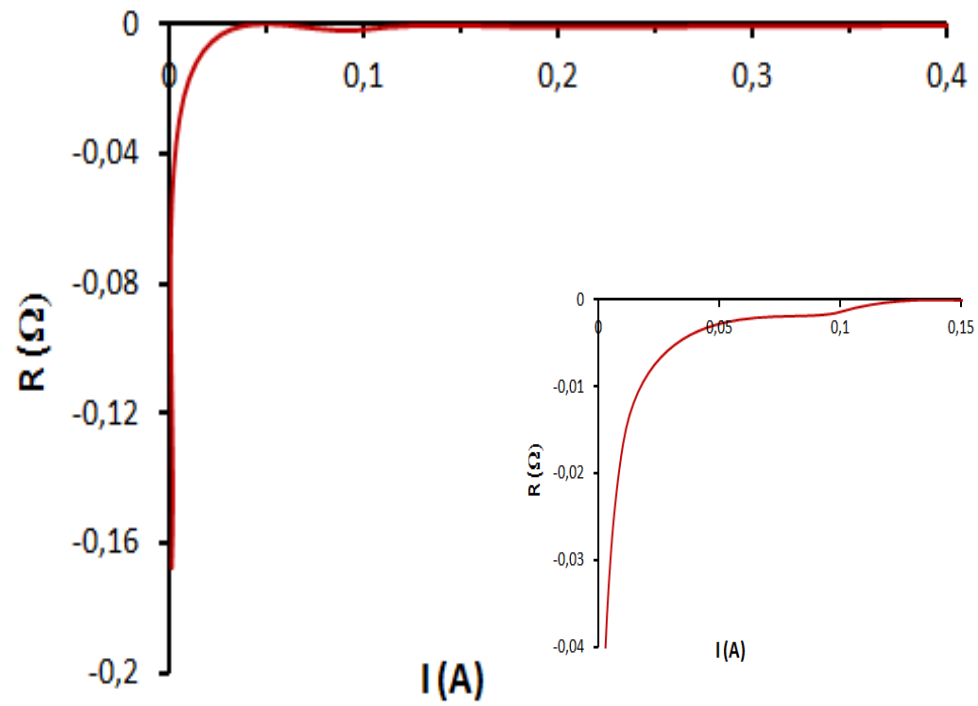


Figure 4.13 R vs I and V vs I graphs for obtaining electrical resistivity value of the bulk glassy $(\text{Fe}_{36}\text{Co}_{36}\text{B}_{19.2}\text{Si}_{4.8}\text{Nb}_4)_{99.25}\text{Cu}_{0.75}$ alloy. Inset shows the region of change of R where is close to zero.

4.2 CRYSTALLIZATION KINETICS OF THE BULK GLASSY ALLOYS

The thermo-analytical techniques are generally used to observe crystallization behaviour of alloy systems. There are two approaches when using thermal analysis, one is the isothermal heating at a temperature below the crystallization temperature and the other is non-isothermal heating by applying different heating rates.

4.2.1 Isochronal DSC Analyses

The non-isothermal experiments are highly advantageous since they allow for the observation of many of the phase transformations occurring in short time durations which otherwise can not be detected. For this reason, non-isothermal DSC experiments was conducted using different heating rates. The heating rates were chosen as 10, 20, 30, 40, 50, 60 and 80 °C/min and all analyses were done with a constant heating rate from 30 °C to 1400 °C waiting there in molten state for 200 seconds and cooling the melt to 30 °C with the same heating rate. According to the resultant DSC scans given in Figures 4.14- 4.19, the height and area of the peaks get smaller and peaks shift to lower temperatures as the heating rate was decreased. These shifts in the peak temperature were taken into account in calculation of activation energy (E_a) for T_g , T_{x1} and peak temperatures of first (T_{p1}), second (T_{p2}) and third (T_{p3}) exothermic reactions. Some of the heating rate curves did not follow this shifting trends, thus these rates were not taken into account. Calculations were done for 10,20 and 40 °C/min and the high correlation coefficients were obtained.

For calculation of the activation energies, two analytical methods called Kissinger and Ozawa methods defined by equation 2.19 and 2.20 respectively, were used. In these methods, Kissinger ($\ln \frac{\beta}{T_p^2}$ vs $1/T_p$) and Ozawa ($\ln \beta$ vs $1/T_p$) graphs are plotted and activation energies (E_a) of them are obtained from slopes of linear plots of these graphs.

Figure 4.20 shows the Kissinger plots for the glass transition and three crystallization reactions. The activation energies of first, second and third crystallization exotherms denoted as E_{a1} , E_{a2} and E_{a3} are found as 447.18, 1141.33 and 551.12 kJ respectively. Also, the activation energy for glass transition, E_g , was determined to be 288.06 kJ/mol, which is lower than the activation energies of all crystallization reactions. When the activation energies of exothermic transitions are compared, activation energies of T_{x1} and T_{p2} are higher than the others. This means that for other peaks crystallization is easier. Activation energy shows the stability of the alloy because it indicates the energy barrier that atoms should overcome to change their present structures. The highest energy barrier between two stable parts is almost a constant during crystallization process and includes atom migration energy and Gibbs free energy difference between parent and product phases.

Figure 4.20 also shows Ozawa graphs of glass transition and three crystallization reactions and activation energy values of them were given in Table 4.3. When Kissinger and Ozawa methods are compared, it can be observed that the activation energies estimated by two methods were very close to each other especially the glass transition activation energy which is almost the same. The agreement between these two approaches showed that calculated activation energy values were consistent.

As in the alloy cobalt atoms replace iron atoms to form BCC FeCo solid solution, the BCC structure becomes instable when cobalt dominates in lattice. Transforming the instable phase to stable phase requires less energy. Thus, the activation energy for first exothermic peak is lower than second and third exothermic peaks. Meanwhile, Co atoms are more difficult to separate from BCC FeCo solid solution, so the activation energy of second exothermic reaction is larger, and is mainly determined by the energy that Co atoms start to migrate from BCC FeCo phase.

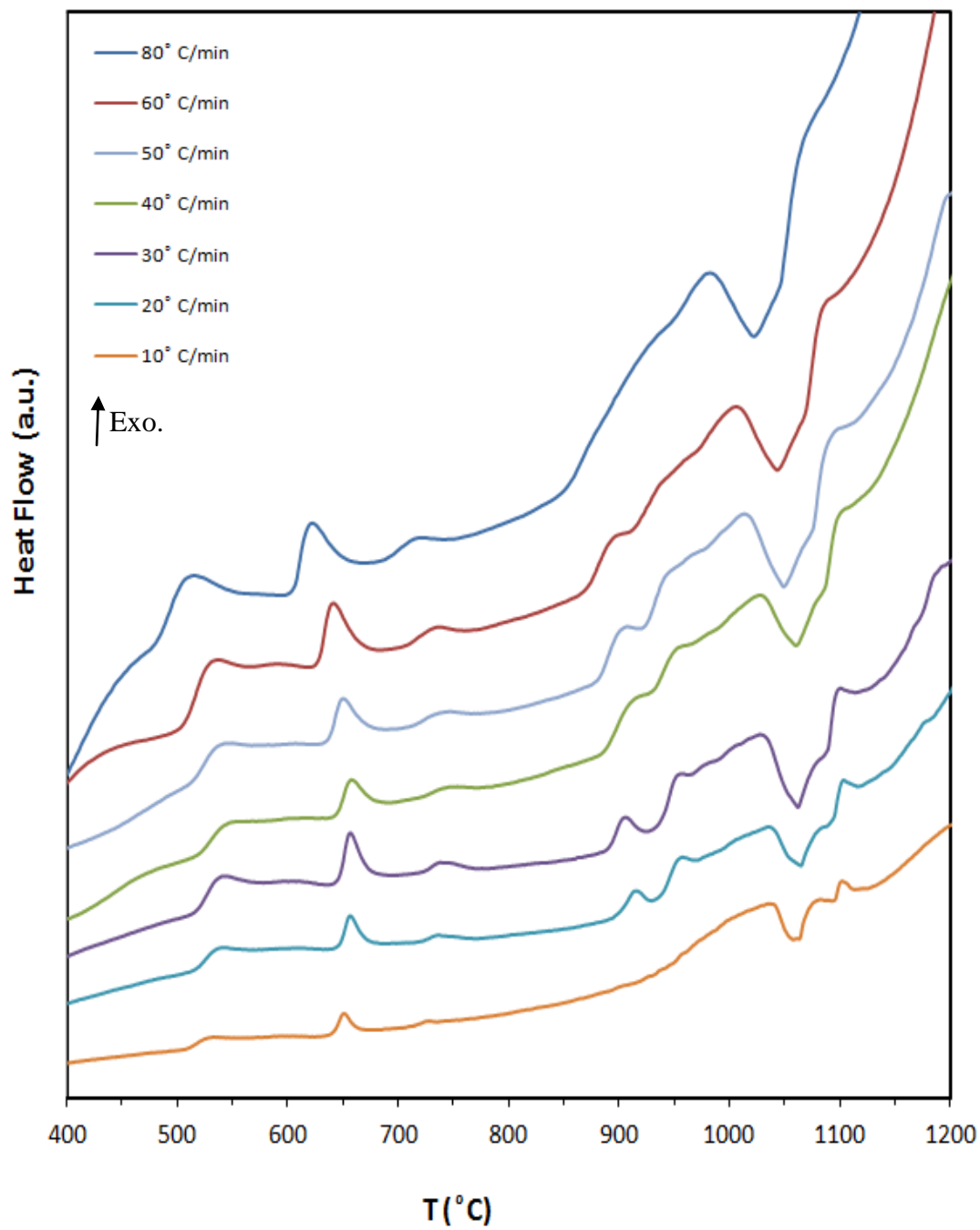


Figure 4.14 1st heating paths of bulk glassy $(\text{Fe}_{36}\text{Co}_{36}\text{B}_{19.2}\text{Si}_{4.8}\text{Nb}_4)_{99.25}\text{Cu}_{0.75}$ alloy at different heating rates.

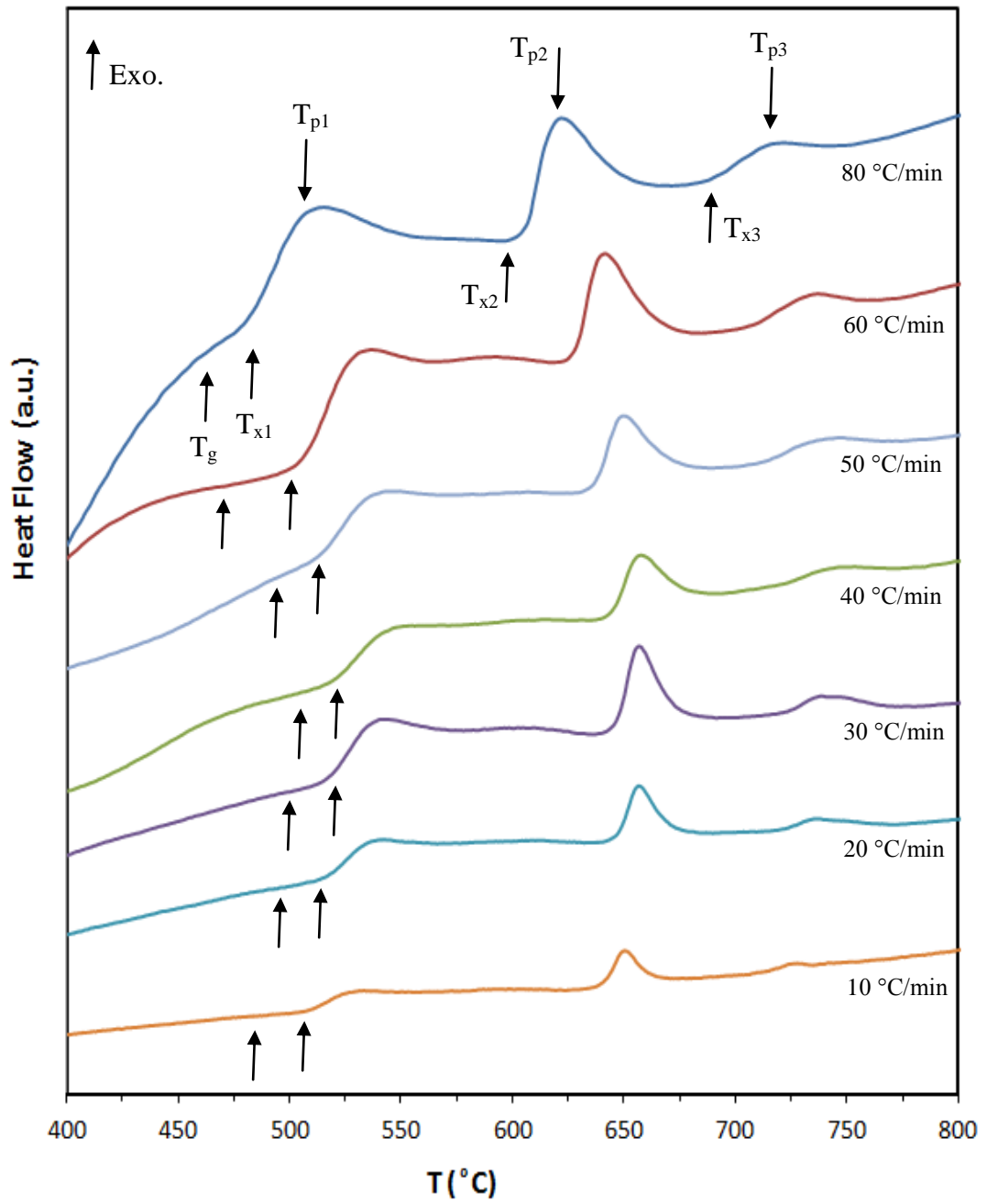


Figure 4.15 Comparison of low temperature regions of 1st heating paths of bulk glassy $(\text{Fe}_{36}\text{Co}_{36}\text{B}_{19.2}\text{Si}_{4.8}\text{Nb}_4)_{99.25}\text{Cu}_{0.75}$ alloy at different heating rates.

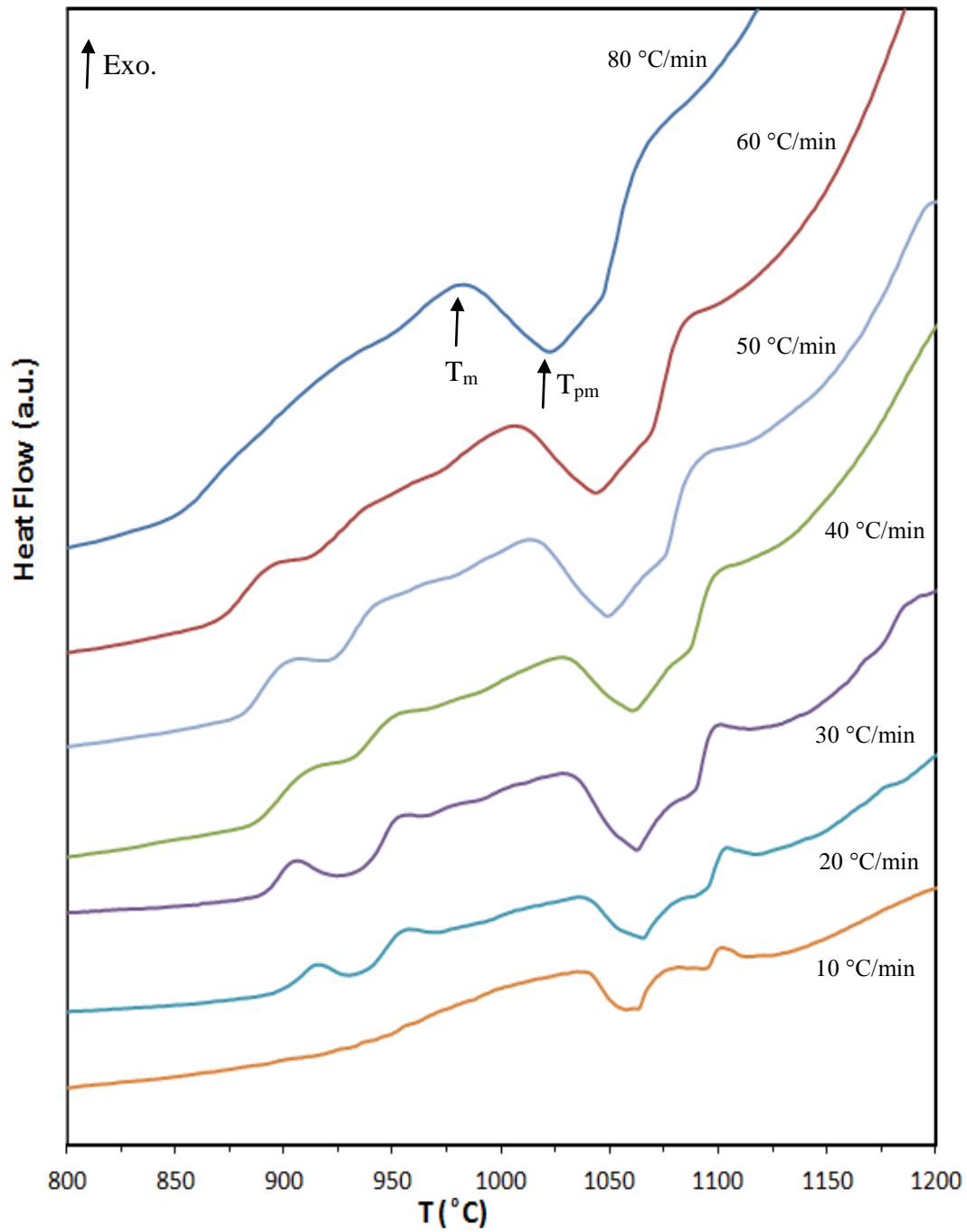


Figure 4.16 Comparison of high temperature regions of 1st heating paths of bulk glassy $(\text{Fe}_{36}\text{Co}_{36}\text{B}_{19.2}\text{Si}_{4.8}\text{Nb}_4)_{99.25}\text{Cu}_{0.75}$ alloy at different heating rates.

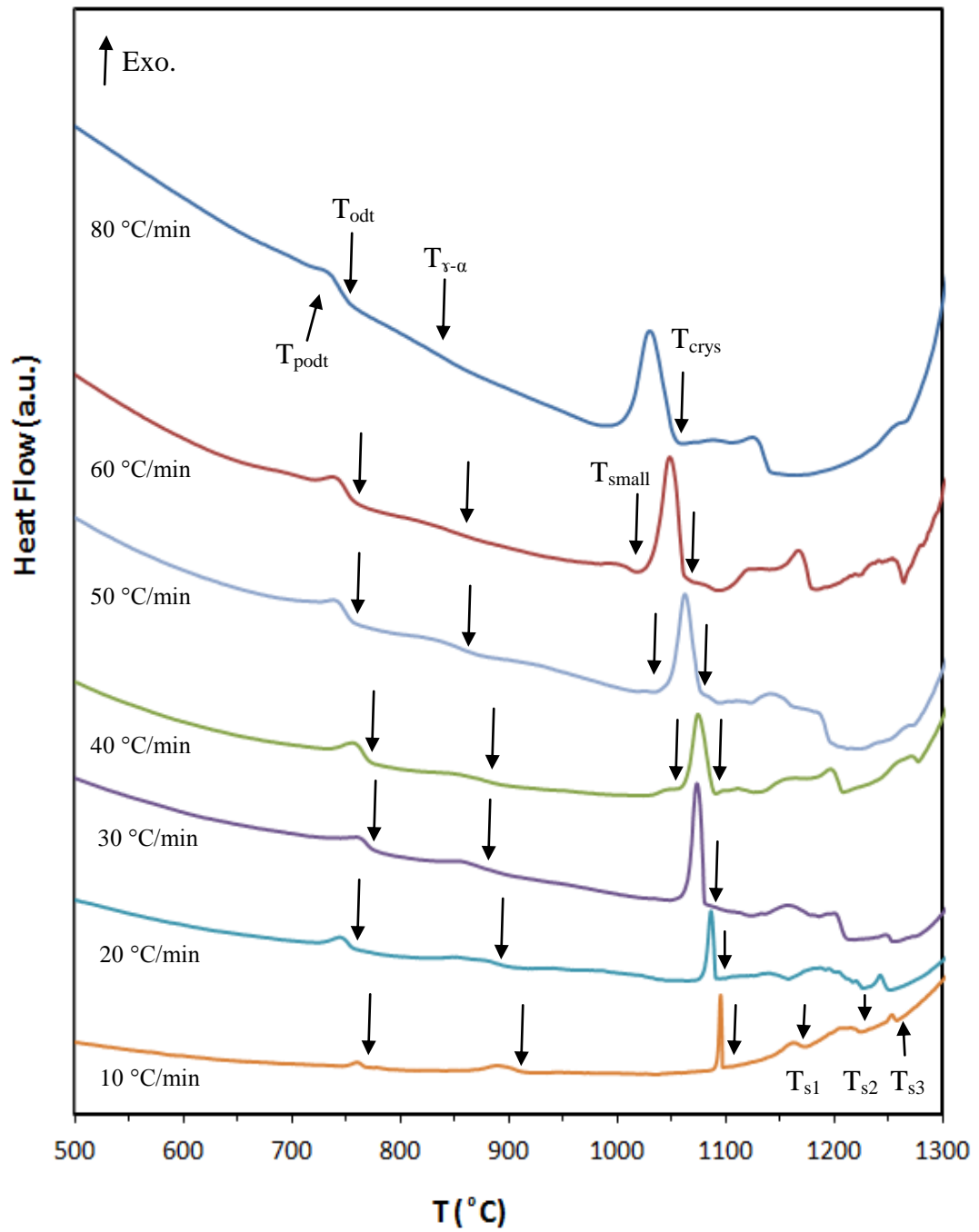


Figure 4.17 1st cooling paths of bulk glassy $(\text{Fe}_{36}\text{Co}_{36}\text{B}_{19.2}\text{Si}_{14.8}\text{Nb}_4)_{99.25}\text{Cu}_{0.75}$ alloy at different heating rates.

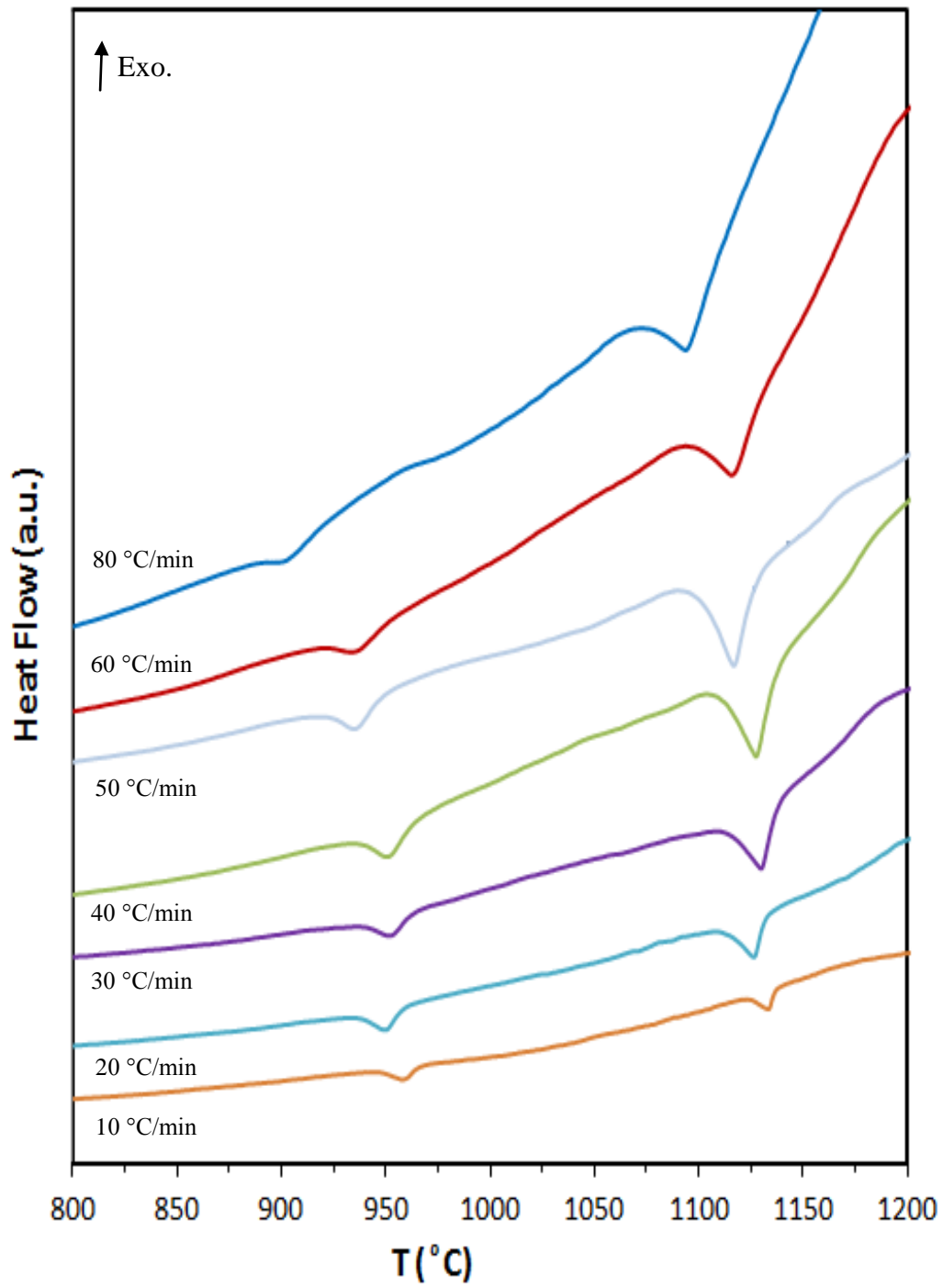


Figure 4.18 2nd heating paths of bulk glassy $(\text{Fe}_{36}\text{Co}_{36}\text{B}_{19.2}\text{Si}_{4.8}\text{Nb}_4)_{99.25}\text{Cu}_{0.75}$ alloy at different heating rates.

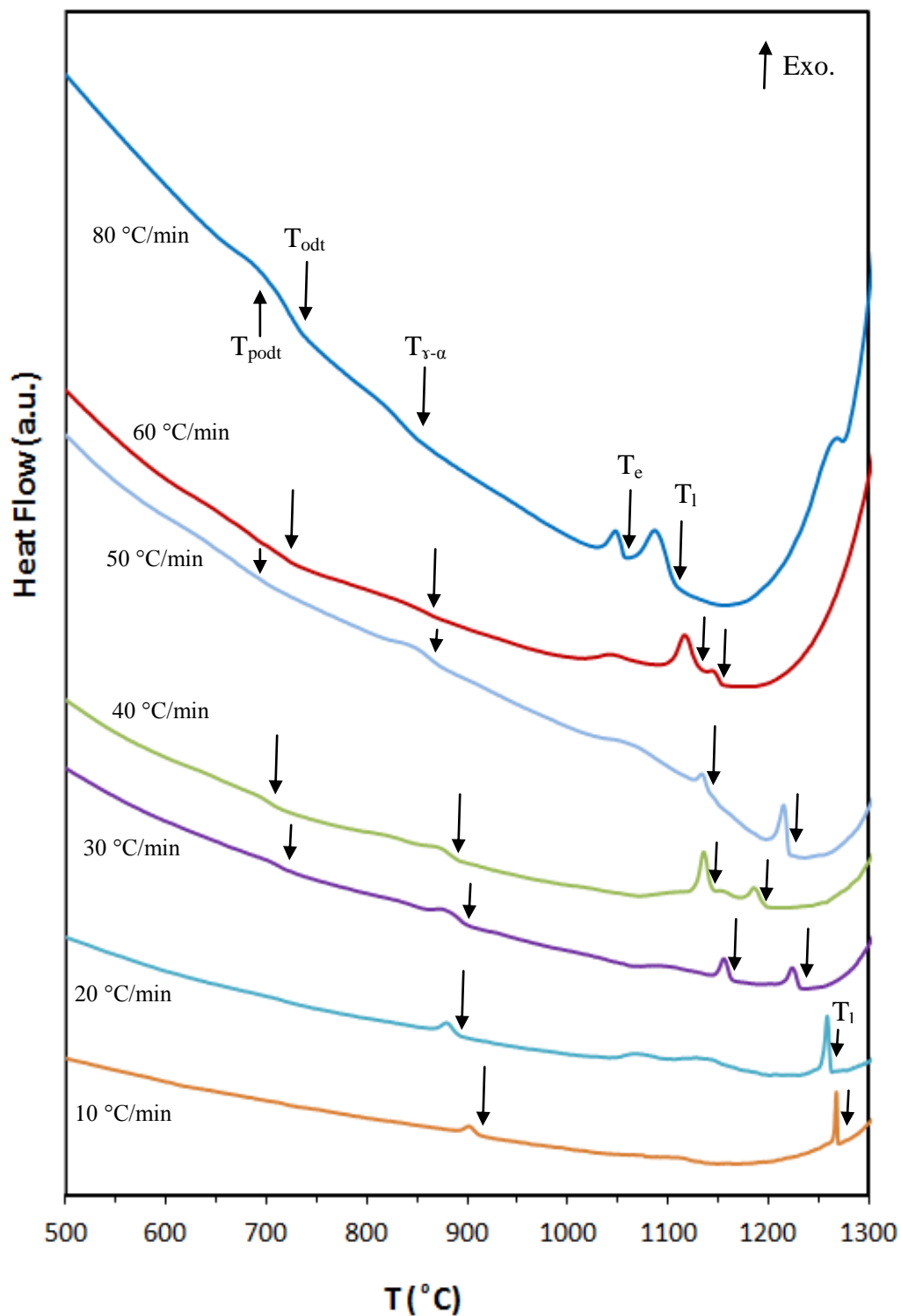


Figure 4.19 2nd cooling paths of bulk glassy $(Fe_{36}Co_{36}B_{19.2}Si_{4.8}Nb_4)_{99.25}Cu_{0.75}$ alloy at different heating rates.

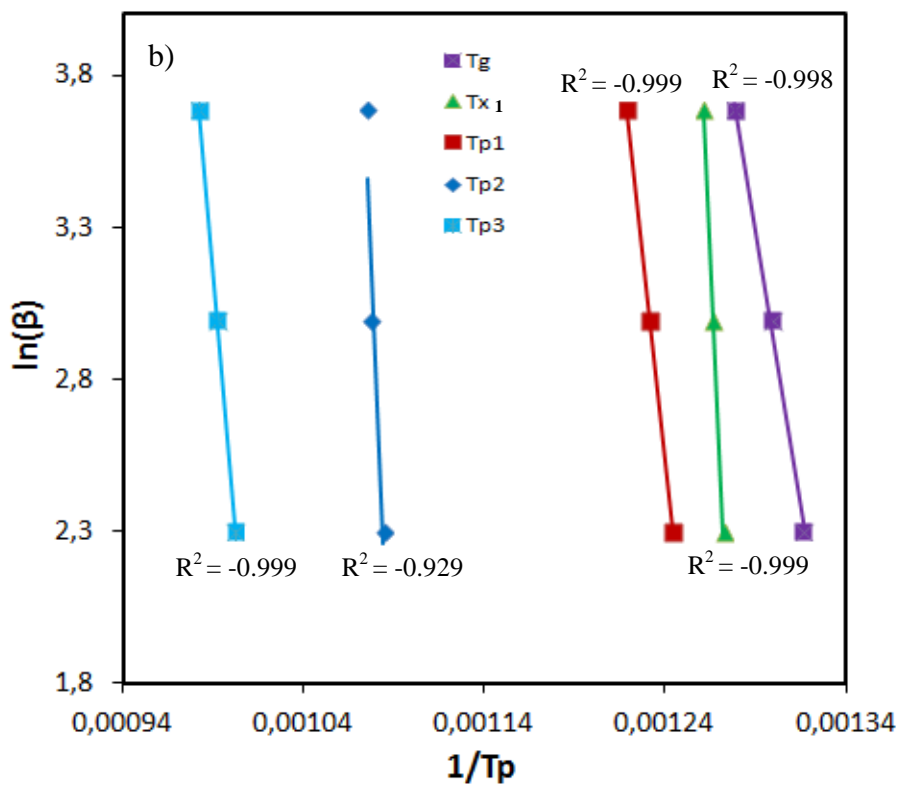
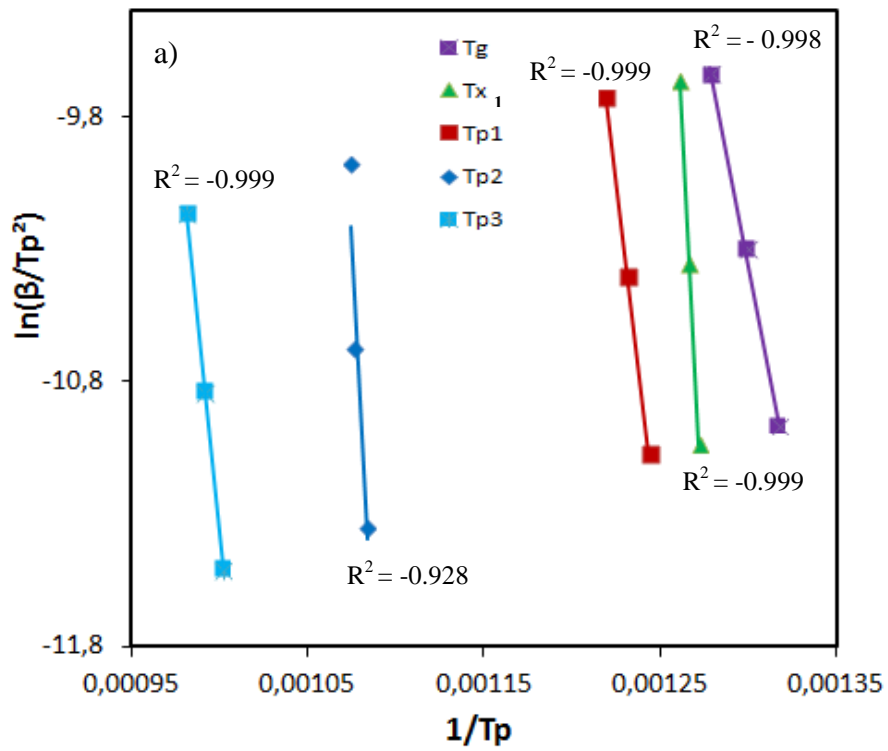


Figure 4.20 a) Kissinger b) Ozawa plots of bulk glassy $(Fe_{36}Co_{36}B_{19.2}Si_{4.8}Nb_4)_{99.25}Cu_{0.75}$ alloy for 10, 20, 40 °C/min.

Table 4.3 Calculated E_a values of the bulk glassy ($\text{Fe}_{36}\text{Co}_{36}\text{B}_{19.2}\text{Si}_{4.8}\text{Nb}_4$) $_{99.25}\text{Cu}_{0.75}$ alloy obtained from Kissinger and Ozawa plots for 10,20,40 °C/min.

	Kissinger E_a	R^2	Ozawa E_a	R^2
T_g	288.06 kJ	- 0.99834	286.12 kJ	- 0.99849
T_{x1}	1062.496 kJ	- 0.99972	1022.85 kJ	- 0.99973
T_{p1}	447.18 kJ	- 0.99985	438.07 kJ	- 0.99985
T_{p2}	1141.33 kJ	- 0.92772	1099.97 kJ	- 0.92943
T_{p3}	551.12 kJ	- 0.99992	540.02 kJ	- 0.99993

In order to design new alloys and investigate whether these alloys can form glass, glass forming ability (GFA) criteria is important. Thus, some glass forming ability criterias were calculated. For doing this calculations, necessary transition temperatures were obtained from isochronal DSC experiments and calculated by using SETARAM thermal analysis software. These temperatures were given in Tables 4.4 - 4.7. Enthalpies (ΔH) of the related peaks were also shown in these tables. Enthalpy values were calculated by SETARAM thermal analysis software by using linear fit.

According to calculated GFA parameters shown in Table 4.8, while some of the calculated parameters show that the alloy has good GFA other parameters may not because some of the parameters are not as powerful as the authors adduced and do not show high correlation with related parameters. These GFA parameters were stated in Chapter 2 Theory. For example; the reduced glass transition temperature T_{rg} is considered in general, the alloy do not show a good GFA since the alloys with T_{rg} greater than 0.67 are considered to be good glass formers. On the other hand, the width of the supercooled liquid region ΔT_x is large. Thus, while ΔT_x can be respectable indicators of high GFA, T_{rg} can not be very suitable in comparing the relative glass forming abilities obtained in this study. γ parameter larger than 0.362 can be considered as good glass formers. The γ values presented in Table 4.8 showed that the alloy can form a good glass.

Table 4.4 Transition temperatures of 1st heating paths of the bulk glassy ($\text{Fe}_{36}\text{Co}_{36}\text{B}_{19.2}\text{Si}_{14.8}\text{Nb}_4$)_{99.25} $\text{Cu}_{0.75}$ alloy obtained from isochronal DSC analysis at different heating rates.

Heating rate C/min.	T_g (°C)	T_{x1} (°C)	T_{x2} (°C)	T_{x3} (°C)	T_m (°C)	T_{p1} (°C)	T_{p2} (°C)	T_{p3} (°C)	T_{pm} (°C)	ΔH_{x1} (J/g)	ΔH_{x2} (J/g)	ΔH_{x3} (J/g)	ΔH_m (J/g)
10 ° C/min.	486.517	513.383	641.546	706.209	1041.082	530.963	649.901	725.209	1062.662	-54.401	-28.563	-2.585	113.017
20 ° C/min.	496.614	516.843	646.934	724.048	1040.581	539.372	656.129	735.206	1065.06	-67.529	-28.488	-8.013	117.095
30 ° C/min.	498.883	516.808	646.799	723.64	1033.713	539.928	656.611	737.72	1062.308	-67.786	-30.572	-8.85	126.976
40 ° C/min.	509.206	520.062	644.792	724.133	1029.604	547.461	657.291	745.847	1061.401	-39.619	-18.293	-4.856	101.226
50 ° C/min.	493.000	512.919	636.905	717.86	1017.573	541.066	649.302	739.864	1049.948	-47.776	-24.68	-6.109	134.108
60 ° C/min.	468.412	507.371	628.265	709.431	1010.15	531.468	640.904	734.542	1045.328	-56.224	-25.757	-6.234	99.152
80 ° C/min.	464.656	480.146	605.42	691.194	985.066	511.452	620.53	716.516	1025.905	-49.899	-30.269	-6.494	110.302

Table 4.5 Transition temperatures of 1st cooling paths of the bulk glassy $(\text{Fe}_{36}\text{Co}_{36}\text{B}_{19.2}\text{Si}_{4.8}\text{Nb}_4)_{99.25}\text{Cu}_{0.75}$ alloy obtained from isochronal DSC analysis at different heating rates.

Heating rate	T_{odt} (° C)	$T_{\gamma-\alpha}$ (° C)	T_{small} (° C)	T_{crys} (° C)	T_{s1} (° C)	T_{s2} (° C)	T_{s3} (° C)
10 ° C/min.	751.834	873.827	—	1091.556	1144.808	1182.625	1246.097
20 ° C/min.	728.585	833.572	—	1080.317	1125.343	1163.603	1235.868
30 ° C/min.	732.815	826.859	—	1064.457	Separated peak: 1171.343		
40 ° C/min.	736.68	832.781	1036.257	1064.196	1092.153	Separated peak: 1173.875	
50 ° C/min.	712.712	793.111	1020.542	1049.546	1097.067	Separated peak: 1124.585	
60 ° C/min.	719.73	793.446	984.438	1033.625	1070.42	Separated peak: 1138.91	
80 ° C/min.	695.614	774.145	—	1010.027	Separated peak: 1089.409		

Heating rate	T_{podt} (° C)	$T_{\text{pv}-\alpha}$ (° C)	T_{psmall} (° C)	T_{percrys} (° C)	T_{ps1} (° C)	T_{ps2} (° C)	T_{ps3} (° C)
10 ° C/min.	759.399	889.33	—	1094.249	1159.911	1203.503	1251.808
20 ° C/min.	742.969	853.241	—	1085.406	1139.123	1186.876	1241.597
30 ° C/min.	760.41	856.96	—	1072.794	Separated peak: 1200.489		
40 ° C/min.	756.851	853.108	1042.998	1074.596	1110.939	Separated peak: 1197.093	
50 ° C/min.	738.618	831.324	1026.585	1062.252	1109.994	Separated peak: 1185.461	
60 ° C/min.	740.148	821.404	1000.314	1047.92	1080.602	Separated peak: 1166.56	
80 ° C/min.	730.777	802.879	—	1029.154	Separated peak: 1125.165		

Table 4.6 Enthalpy values of 1st cooling paths of the bulk glassy $(\text{Fe}_{36}\text{Co}_{36}\text{B}_{19.2}\text{Si}_{4.8}\text{Nb}_4)_{99.25}\text{Cu}_{0.75}$ alloy obtained from isochronal DSC analysis at different heating rates.

Heating rate	ΔH_{odt} (J/g)	$\Delta H_{\gamma-\alpha}$ (J/g)	ΔH_{small} (J/g)	ΔH_{crys} (J/g)	ΔH_{s1} (J/g)	ΔH_{s2} (J/g)	ΔH_{s3} (J/g)
10 °C/min.	-6.247	-22.152	—	-26.657	-16.925	-33.839	-6.577
20 °C/min.	-21.373	-21.207	—	-32.639	-13.686	-50.939	-9.764
30 °C/min.	-17.484	-13.419	—	-62.384	Separated peak: -61.141		
40 °C/min.	-14.695	-6.804	-0.784	-41.226	-3.248	Separated peak: -36.63	
50 °C/min.	-27.557	-9.229	-0.248	-70.315	-1.255	Separated peak: -50.635	
60 °C/min.	-11.17	-3.649	-2.077	-58.061	-0.469	Separated peak: - 46.912	
80 °C/min.	-38.967	-2.428	—	-68.01	Separated peak: -31.411		

For the calculation of the GFA values transition temperatures of the 2nd cooling paths were used. As it was stated before, the cooling region of 1st path can not give exact results due to strong local order preserving even in the molten state. This situation can be seen clearly from Figure 4.21. When 1st and 2nd cooling paths were compared, it was seen that 2nd cooling path has clearer peaks than 1st cooling paths.

Table 4.7 Transition temperatures of 2nd cooling paths of the bulk glassy ($\text{Fe}_{36}\text{Co}_{36}\text{B}_{19.2}\text{Si}_{14.8}\text{Nb}_4$)_{99.25} $\text{Cu}_{0.75}$ alloy obtained from isochronal DSC analysis at different heating rates.

Heating rate C/min.	T_{odt} (°C)	$T_{\gamma-\alpha}$ (°C)	T_e (°C)	T_1 (°C)	T_{podt} (°C)	$T_{\text{py-}\alpha}$ (°C)	T_{pe} (°C)	T_{pl} (°C)	ΔH_{odt} (J/g)	$\Delta H_{\gamma-\alpha}$ (J/g)	ΔH_e (J/g)	ΔH_1 (J/g)
10° C/min.	—	892.982	—	1265.504	—	901.888	—	1268.054	—	-10.174	—	-15.431
20° C/min.	—	870.161	—	1253.665	—	879.328	—	1258.203	—	-9.498	—	-24.476
30° C/min.	687.219	861.663	1147.594	1216.043	700.373	877.708	1155.501	1224.051	-1.853	-7.775	-8.157	-8.316
40° C/min.	674.767	850.521	1127.361	1176.401	692.251	871.472	1134.916	1185.34	-1.165	-4.608	-12.831	-5.848
50° C/min.	593.884	821.784	1127.286	1206.287	634.846	849.706	1134.237	1215.206	-5.339	-7.803	-3.479	-14.783
60° C/min.	625.153	797.479	1103.593	1138.808	647.227	834.647	1116.73	1145.88	-5.35	-6.534	-14.164	-1.441
80° C/min.	654.88	767.745	1033.811	1066.556	693.627	815.835	1046.91	1086.81	-29.86	-7.251	-6.795	-23.718

Table 4.8 Calculated GFA parameters of the bulk glassy $(\text{Fe}_{36}\text{Co}_{36}\text{B}_{19.2}\text{Si}_{4.8}\text{Nb}_4)_{99.25}\text{Cu}_{0.75}$ alloy obtained from isochronal DSC analysis at different heating rates.

Heating Rate	T_{rg}	ΔT_x	α	β	new β	γ	γ_m
10 °C/min.	0.494	27	0.511	1.529	1.056	0.342	0.529
20 °C/min.	0.504	20	0.517	1.530	1.119	0.344	0.531
30 °C/min.	0.518	18	0.530	1.542	1.247	0.349	0.542
40 °C/min.	0.539	11	0.547	1.554	1.440	0.355	0.555
50 °C/min.	0.518	20	0.531	1.544	1.252	0.350	0.545
60 °C/min.	0.525	39	0.553	1.578	1.451	0.362	0.580
80 °C/min.	0.551	15	0.562	1.572	1.616	0.363	0.574

Heating Rate	δ	K_{gl}	ϕ	T_{rx}	ω	S	γ_c
10 °C/min.	1.009	0.051	0.306	0.511	0.305	0.622	0.546
20 °C/min.	1.043	0.039	0.299	0.517	0.304	0.592	0.544
30 °C/min.	1.101	0.035	0.303	0.530	0.295	0.537	0.554
40 °C/min.	1.189	0.021	0.293	0.547	0.285	0.380	0.562
50 °C/min.	1.102	0.039	0.307	0.531	0.292	0.732	0.558
60 °C/min.	1.164	0.077	0.345	0.553	0.261	1.266	0.608
80 °C/min.	1.251	0.031	0.317	0.562	0.269	0.657	0.585

Critical Cooling Rate Calculations:

Barandiaran-Colmenero [64] approach was used to estimate the critical cooling rate experimentally. Calculations were done for 10, 20 and 40 °C/min. The critical cooling rate (R_c) was calculated from the linear plot of $\ln R$ vs $(T_\ell - T_{xc})^2$ where R is the cooling rate, T_ℓ is the offset temperature of fusion and T_{xc} is the onset temperature of solidification upon cooling at a rate R . According to this plot shown in Figure 4.21, the intersection point of the line with $\ln R$ axis gave the logarithm of the critical cooling rate. R_c was calculated as 0.17 K/s which is extremely low when the case was Fe based bulk amorphous alloys. This low R_c showed that $(Fe_{36}Co_{36}B_{19.2}Si_{4.8}Nb_4)_{99.25}Cu_{0.75}$ alloy can form glass easily because low critical cooling rates are required for production of the bulk metallic glasses.

Figure 4.21 has one more plots of $\ln R$ vs $(T_\ell - T_{xc})^2$. In this plot, T_{xc} values were obtained from first cooling path of isochronal DSC experiments. R_c was calculated as 0.15 K/s which is extremely low again. Figure 4.22 shows the difference between plots which includes T_{xc} values obtained from first and second cooling paths.

$(Fe_{36}Co_{36}B_{19.2}Si_{4.8}Nb_4)_{99.25}Cu_{0.75}$ alloy was produced by rapid solidification technique. Non-equilibrium structures can be reached with this technique that led to synthesis of bulk metallic glasses. In the rapid solidification processing, a molten metal or alloy is solidified very rapidly at rates of about 10^6 K/s, but at least at about 10^4 K/s [24]. In the light of these informations, another approach was attempted for the calculation of R_c because Barandiaran and Colmenero approach was not consistent with these rates. Apart from Barandiaran and Colmenero approach, Liu [35] et al. enhanced γ_m parameter and found a linear relationship between γ_m and R_c such as $\log_{10} R_c = 14.99 - 19.441 \gamma_m$. They calculated correlation factor as $R^2 = 0.931$. By using calculated γ_m parameters shown in Table 4.8 for the $(Fe_{36}Co_{36}B_{19.2}Si_{4.8}Nb_4)_{99.25}Cu_{0.75}$ alloy, R_c values of the alloy were calculated according to approach of Liu et al. and results were shown in table 4.10. Calculated R_c vs γ_m results were plotted and shown in Figure 4.23. R_c values obtained from Liu et al. approach are more consistent with rates of the rapid solidification processing.

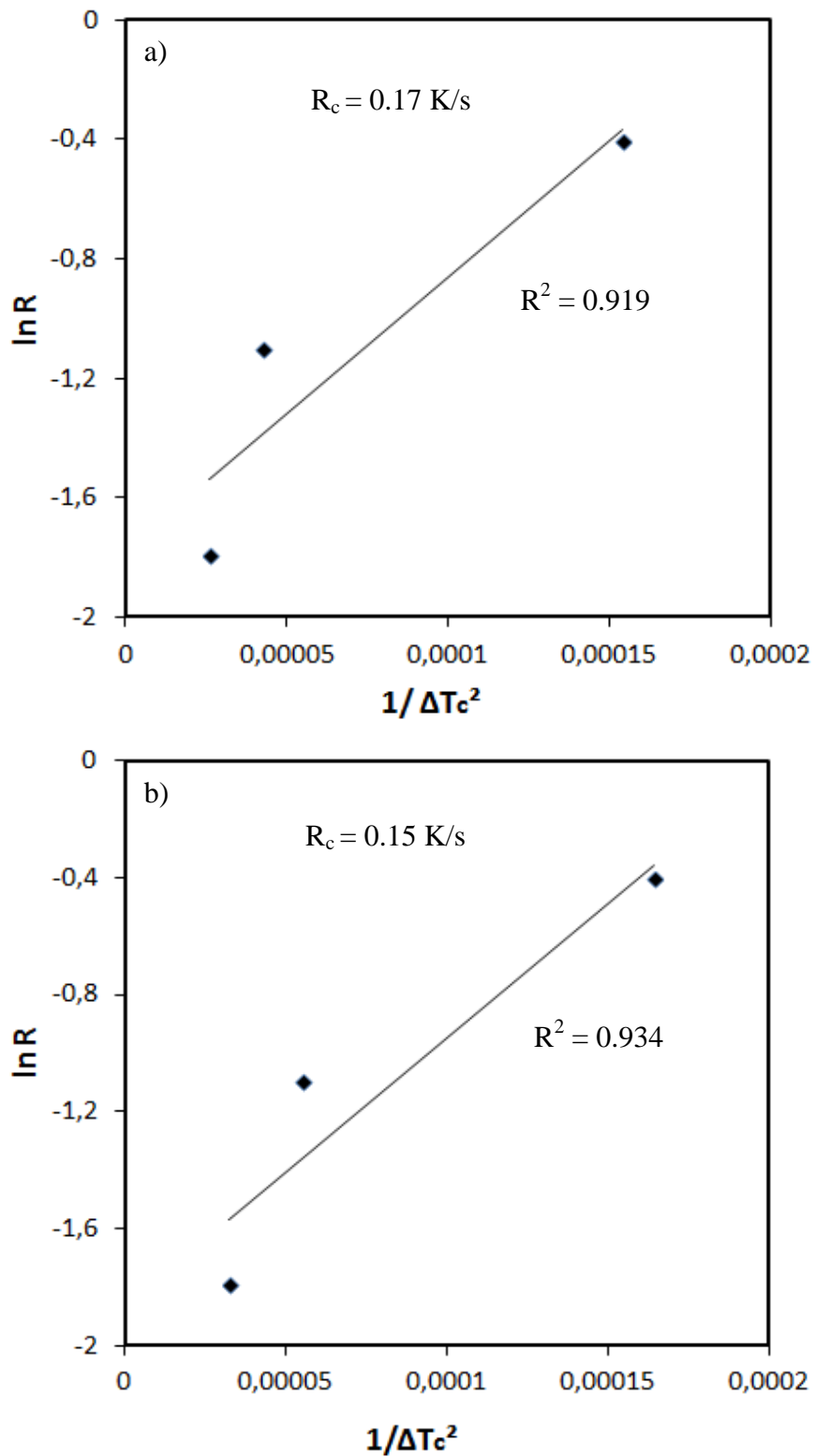


Figure 4.21 Barandiaran-Colmenero plots of the bulk glassy $(\text{Fe}_{36}\text{Co}_{36}\text{B}_{19.2}\text{Si}_{4.8}\text{Nb}_4)_{99.25}\text{Cu}_{0.75}$ alloy for 10, 20, 40 °C/min. T_{xc} values obtained from a) second and b) first cooling paths.

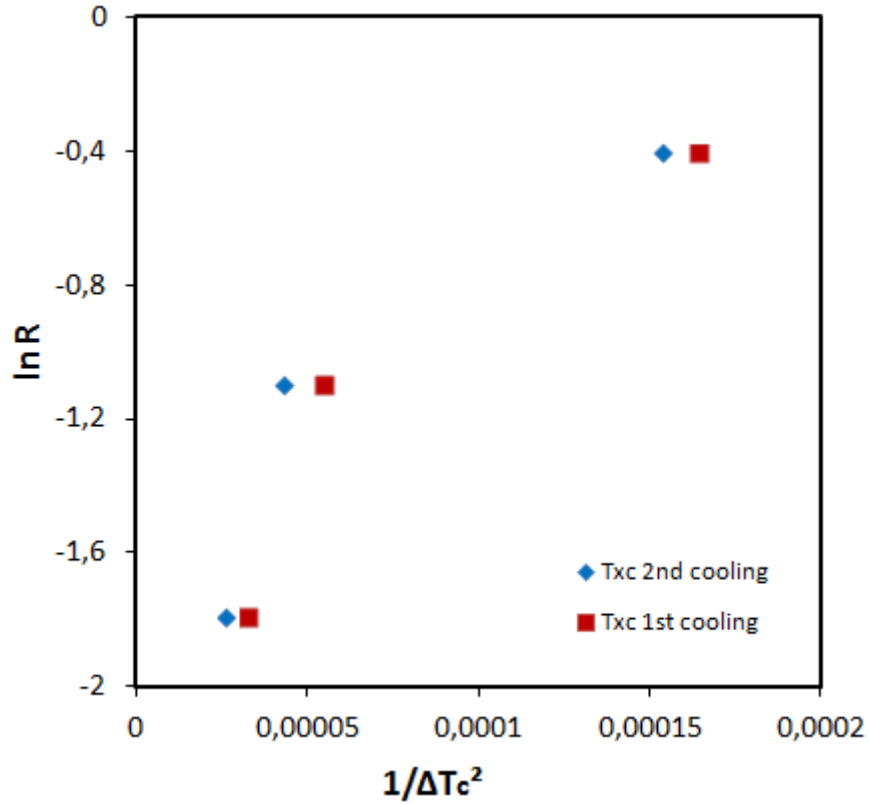


Figure 4.22 Comparison of Barandiaran-Colmenero plots for first and second cooling paths of the bulk glassy $(\text{Fe}_{36}\text{Co}_{36}\text{B}_{19.2}\text{Si}_{4.8}\text{Nb}_4)_{99.25}\text{Cu}_{0.75}$ alloy for 10, 20 and 40 °C/min.

Table 4.9 T_t and T_{xc} values of the bulk glassy $(\text{Fe}_{36}\text{Co}_{36}\text{B}_{19.2}\text{Si}_{4.8}\text{Nb}_4)_{99.25}\text{Cu}_{0.75}$ alloy obtained from isochronal DSC analysis at different heating rates.

Heating rate	2nd cooling		1st cooling	
	T_t (K)	T_{xc} (K)	T_t (K)	T_{xc} (K)
10 °C/min	1343.691	1538.504	1343.691	1519.097
20 °C/min	1373.722	1526.665	1373.722	1508.868
40 °C/min	1368.788	1449.401	1368.788	1446.875

Table 4.10 γ_m and R_c values of the bulk glassy $(\text{Fe}_{36}\text{Co}_{36}\text{B}_{19.2}\text{Si}_{4.8}\text{Nb}_4)_{99.25}\text{Cu}_{0.75}$ alloy at different heating rates. R_c was calculated by Liu et al. approach.

Heating rate	γ_m	R_c (K/s)
10 °C/min	0.528597	51706.57
20 °C/min	0.530615	47240.42
30 °C/min	0.542451	27810.58
40 °C/min	0.554655	16104.68
50 °C/min	0.544748	25093.09
60 °C/min	0.580341	5100.24
80 °C/min	0.573799	6835.553

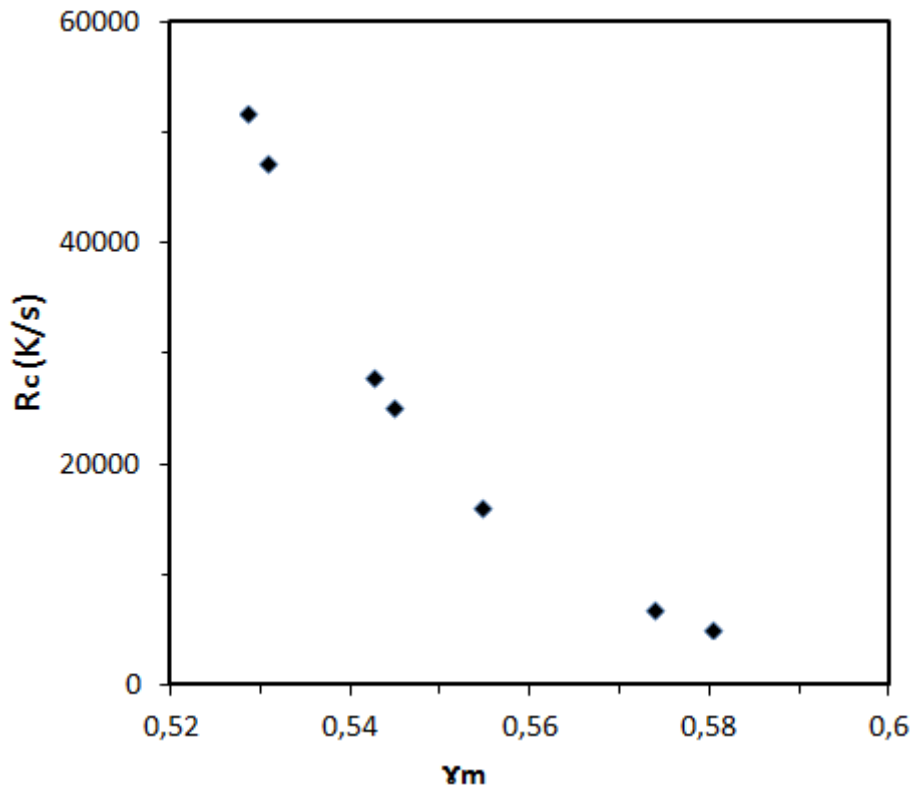


Figure 4.23 R_c calculated by Liu et al. approach vs γ_m plots of the bulk glassy $(\text{Fe}_{36}\text{Co}_{36}\text{B}_{19.2}\text{Si}_{4.8}\text{Nb}_4)_{99.25}\text{Cu}_{0.75}$ alloy for different heating rates.

4.2.2 Isothermal DSC Analyses

In order to investigate the crystallized phases of the $(\text{Fe}_{36}\text{Co}_{36}\text{B}_{19.2}\text{Si}_{4.8}\text{Nb}_4)_{99.25}\text{Cu}_{0.75}$ amorphous alloy and obtain an interpretation of the observed peaks in DSC traces of the amorphous samples, the isothermal annealing experiments were performed.

Two representative parts of the amorphous rod samples numbered as 1 and 10 shown in Figure 4.1 were heated by using Setaram DSC131 under argon atmosphere with a constant heating rate 100 °C/min from 25 °C to selected temperature waiting there for a different holding time and cooling the melt to 25 °C with the same heating rate. The two selected temperatures are 535 °C and 585 °C chosen above the first crystallization temperature and holding time was changed like 5, 15, 30, 60, 120, 240 and 480 min.

Results of the DSC scans were given in Figure 4.24. According to DSC results, 5 min annealing at 585 °C shows an exothermic peak while for all other holding times no exothermic peaks were appeared for both 535 °C and 585 °C. Therefore, the JMAK analysis could not be performed on these selected temperatures since the crystallization peaks could not be detected at all holding times. This may be attributed to the high stability of the alloy against crystallization.

For applying JMAK method, DSC procedures with higher temperatures should be applied and investigated whether crystallization peaks can be observed or not in this high temperatures. The further works can be made for clarification of the behaviour of the $(\text{Fe}_{36}\text{Co}_{36}\text{B}_{19.2}\text{Si}_{4.8}\text{Nb}_4)_{99.25}\text{Cu}_{0.75}$ amorphous alloy.

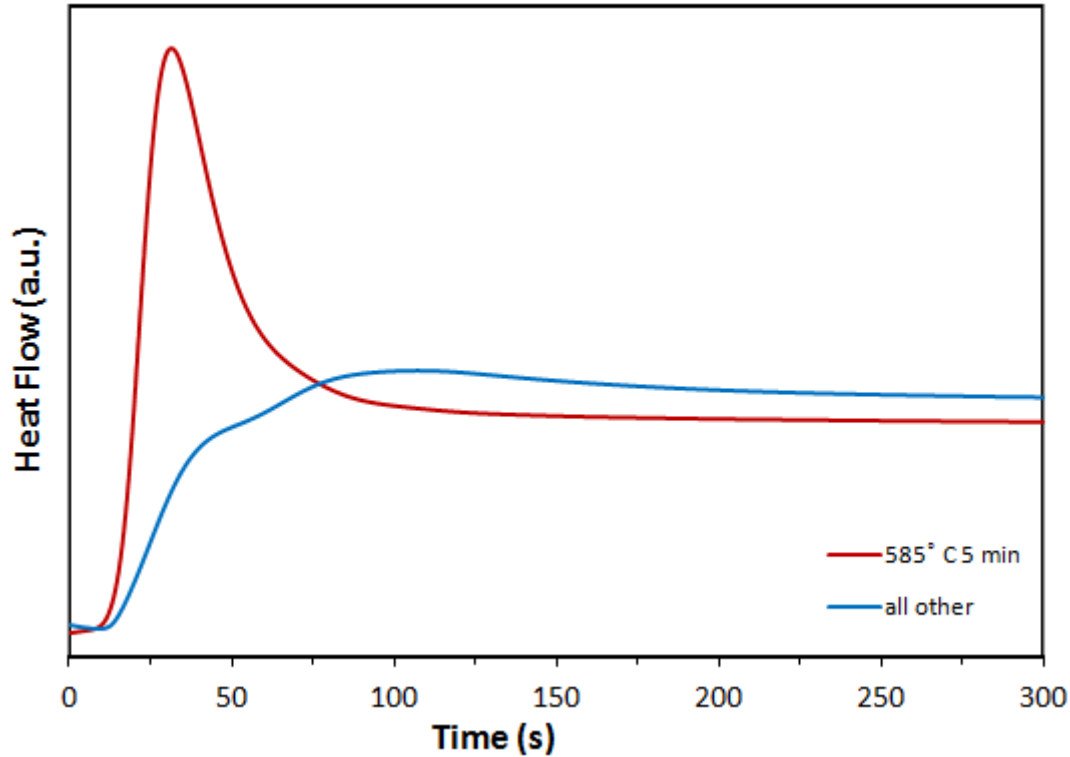


Figure 4.24 Isothermal DSC traces of the bulk amorphous $(\text{Fe}_{36}\text{Co}_{36}\text{B}_{19.2}\text{Si}_{4.8}\text{Nb}_4)_{99.25}\text{Cu}_{0.75}$ alloy at 535 °C and 585 °C for all holding times. 5 min annealing at 585 °C shows an exothermic peak but for all other holding times no exothermic peaks were appeared for both 535 °C and 585 °C.

XRD patterns of the alloys for different holding times were given in Figure 4.25 and Figure 4.26. From XRD results, α -(Fe,Co) peaks can be seen for both temperatures. The sizes of the BCC α -(Fe,Co) crystallites were estimated by Scherrer formula and results were given in Table 4.11. It can be seen from the table, sizes of the BCC α -(Fe,Co) crystallites are highly small and do not show regular increase as holding time increases due to the nonhomogeneous structure of the alloy. For clarity, changes of crystallite sizes with respect to time were plotted for both temperatures and shown in Figure 4.27.

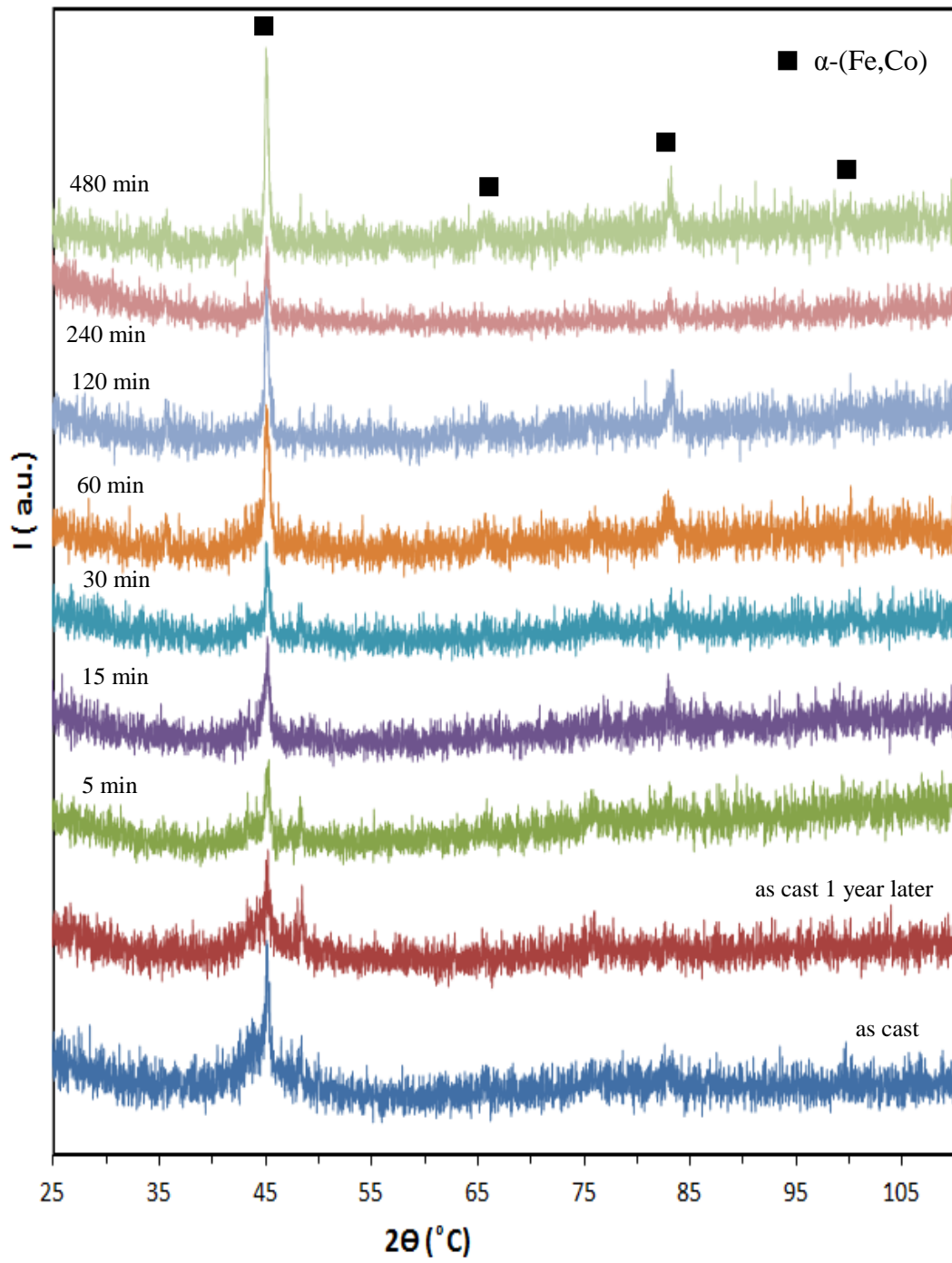


Figure 4.25 XRD patterns of the bulk glassy $(\text{Fe}_{36}\text{Co}_{36}\text{B}_{19.2}\text{Si}_{4.8}\text{Nb}_4)_{99.25}\text{Cu}_{0.75}$ alloy at $535\text{ }^\circ\text{C}$ for different holding times.

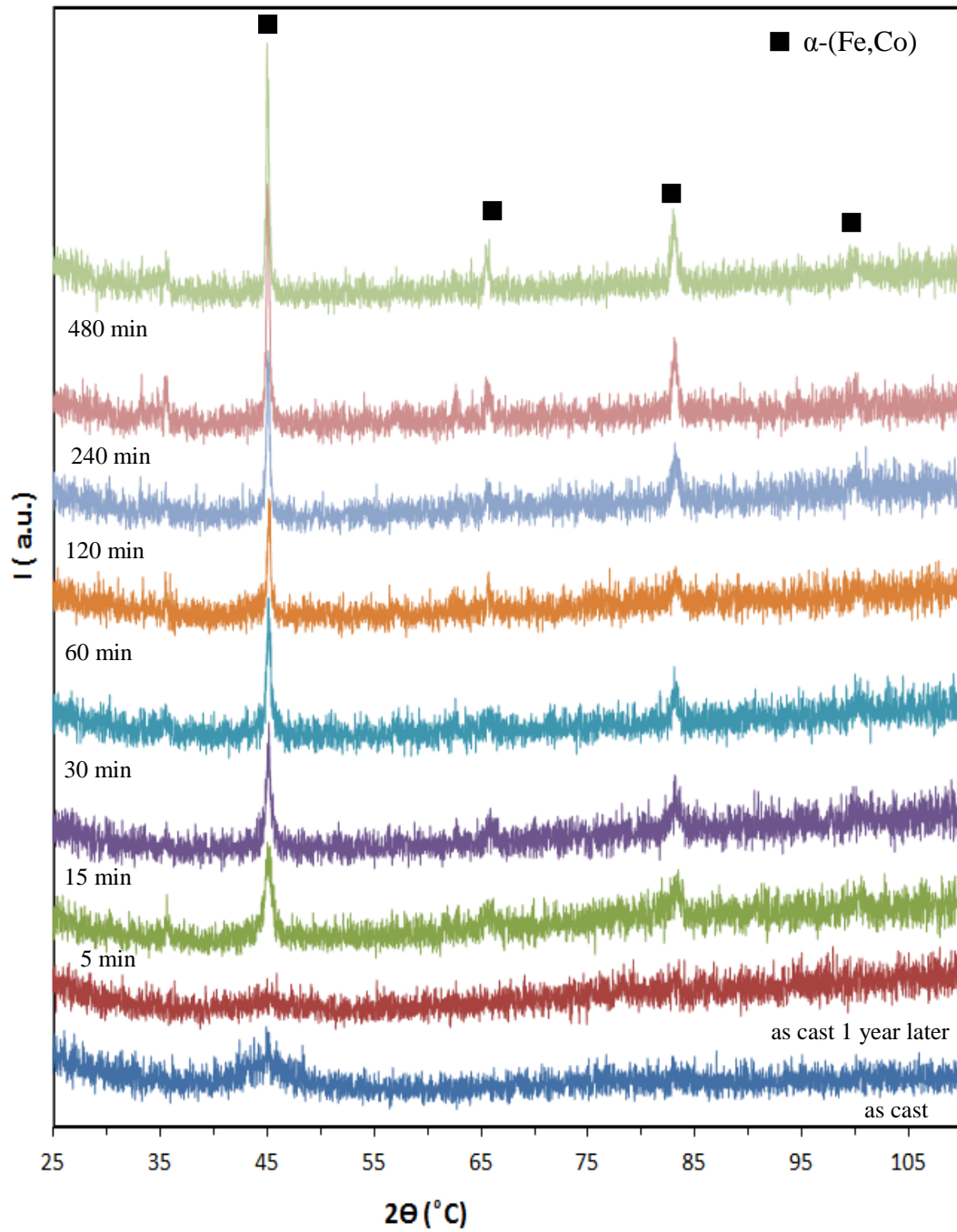


Figure 4.26 XRD patterns of the bulk glassy $(\text{Fe}_{36}\text{Co}_{36}\text{B}_{19.2}\text{Si}_{4.8}\text{Nb}_4)_{99.25}\text{Cu}_{0.75}$ alloy at $585\text{ }^\circ\text{C}$ for different holding times.

Table 4.11 α -(Fe,Co) crystallite sizes estimated by Scherrer formula for annealed bulk glassy $(\text{Fe}_{36}\text{Co}_{36}\text{B}_{19.2}\text{Si}_{4.8}\text{Nb}_4)_{99.25}\text{Cu}_{0.75}$ alloy at different holding times.

Time (min)	α -(Fe,Co) Crystallite Size (nm)	
	535 °C	585 °C
5	27.89	12.81
15	19.73	21.43
30	48.13	26.02
60	15.70	25.28
120	22.68	26.36
240	40.15	27.86
480	22.46	33.33

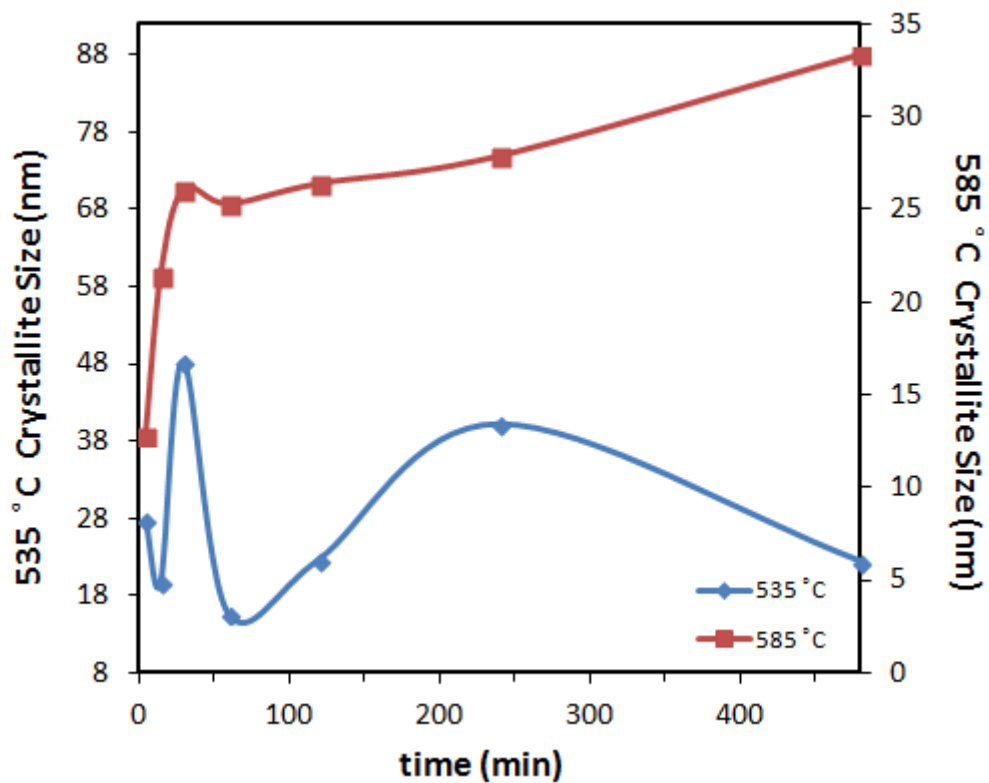


Figure 4.27 Changes of crystallite size vs time graph of the bulk glassy $(\text{Fe}_{36}\text{Co}_{36}\text{B}_{19.2}\text{Si}_{4.8}\text{Nb}_4)_{99.25}\text{Cu}_{0.75}$ alloy at 535 °C and 585 °C.

After 480 min annealing, the resultant microstructures were investigated by SEM to observe α -(Fe,Co) crystalline phases. The backscattered electrons micrographs of the as-polished annealed samples at 535 °C and 585 °C were given in Figure 4.28. As it can be seen from the SEM micrographs of the alloys, there is no precipitation of any phases. Since annealed samples show featureless matrix, the exact identification of the crystallization products could not be achieved by SEM. The further studies by using transmission electron microscopy, exact nature and sizes of the crystallized phases may be revealed.

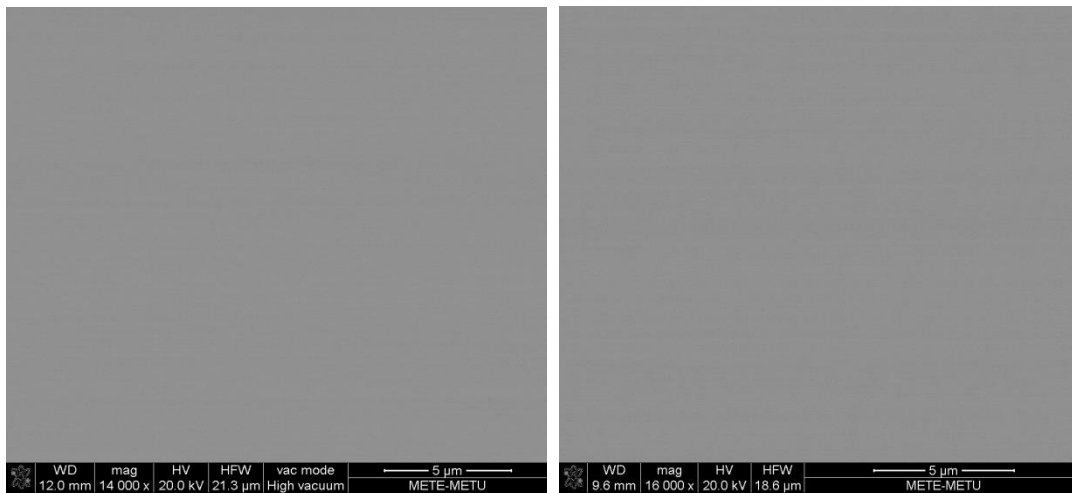


Figure 4.28 Back scattered electrons images of the bulk amorphous $(\text{Fe}_{36}\text{Co}_{36}\text{B}_{19.2}\text{Si}_{4.8}\text{Nb}_4)_{99.25}\text{Cu}_{0.75}$ alloy at 535 °C (left) and 585 °C (right).

Apart from back scattered electrons, secondary electrons images of the annealed samples were obtained after etching. In this way, dendritic structures can be seen for both samples annealed at 535 °C and 585 °C. Formation of these dendrites are related to solidification. For supporting this, EDS analyses were done for both annealed samples and given in Appendix A, Figures 9 - 12. According to EDS results, both dendrites and their surroundings have approximately same atomic percentages of the constituent elements. This also shows the compositional homogeneity of the alloys. SEM images of the dendrites and mapping micrographs of them were given in Figure 4.29 and Appendix D.

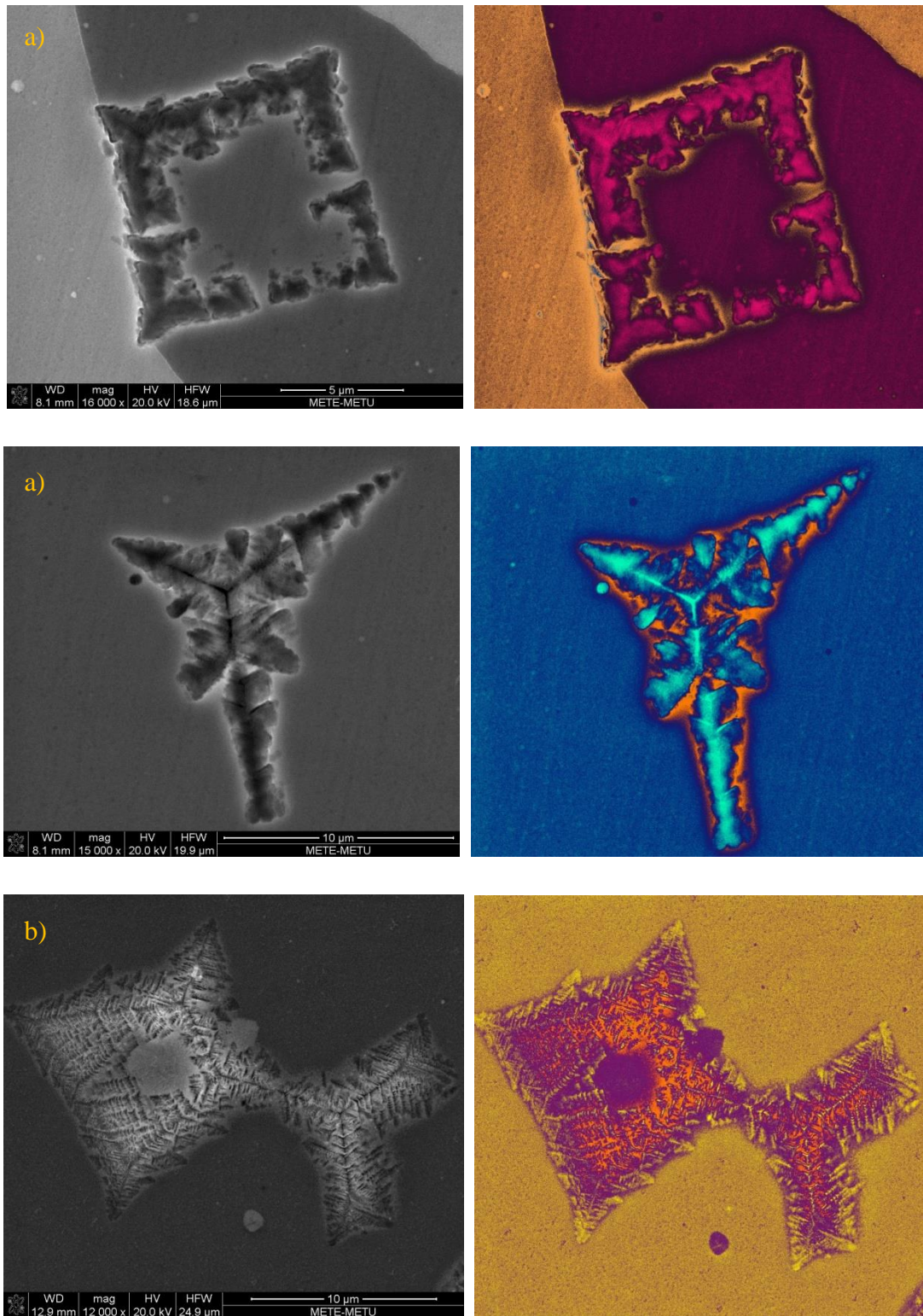


Figure 4.29 SEM images and mapping micrographs of the annealed $(\text{Fe}_{36}\text{Co}_{36}\text{B}_{19.2}\text{Si}_{4.8}\text{Nb}_4)_{99.25}\text{Cu}_{0.75}$ alloy at a) 535 °C and b) 585 °C.

Magnetic Measurements

When Cu modified and Cu free alloys are compared, due to the heterogeneous nucleation effect of Cu clusters formed by structural relaxation of the as cast amorphous alloy during annealing [94] Cu modification provides lower T_x value which means lower supercooling necessary for primary crystallization of the amorphous phase. This primary phase is α -(Fe,Co) phase which is thermodynamically favored at lower temperatures. The two phase metastable microstructure consisting of α -(Fe,Co) nanocrystals dispersed in an amorphous matrix provides very good soft magnetic properties like high saturation magnetization and low coercive force [95, 96].

For verifying that the primary crystallization product of the bulk amorphous $(\text{Fe}_{36}\text{Co}_{36}\text{B}_{19.2}\text{Si}_{4.8}\text{Nb}_4)_{99.25}\text{Cu}_{0.75}$ alloy is α -(Fe,Co), as cast samples numbered as 1 and 10 were annealed at 535 °C and 585 °C respectively for different holding times. The magnetic properties of the alloys were investigated by VSM and results of the analysis were presented in Figure 4.30 and Figure 4.32 showing the hysteresis loops of the as cast and annealed samples for both temperatures.

After 535 °C annealing of the sample at different holding times, it can be seen that when the holding time increases saturation magnetization (B_s) also increases but this increase are very slowly. However, after annealing the alloy at 585 °C for 5 min and obtaining an α -(Fe,Co) phase dispersed in the amorphous matrix in sample, extreme improvements in saturation induction are observed as shown in B-H loops traced in Figure 4.34. After 5 min annealing at 585 °C, for other holding times until 480 min, there was a slightly decrease in B_s value. The slightly altered decrease can be attributed to demagnetization effects due to samples being in bulk forms and is observed in previously reported bulk nanocrystalline soft magnets [97, 98]. However, after 480 min annealing at 585 °C, it will reach the same value at the 5 min annealing.

In conclusion, as cast sample has 1.1 T saturation magnetization but after annealing at 585 °C for 5 min, it has observable change of saturation magnetization such as 1.2 T due to precipitation of α -(Fe,Co) phase in the amorphous matrix. Moreover, coercive force, H_c decreases from 3.214 to 2.12 Oe. Table 4.12 and Table 4.13 gives the values of saturation and remanent magnetizations and coercivities of the annealed samples at 535 °C and 585 °C respectively. For clarity, changes of B_s and H_c with respect to holding time graphs were plotted for both temperatures and shown in Figure 4.31 and Figure 4.33.

Nanocrystalline and amorphous Fe based alloys have been used widely in applications of high frequency transformers, inductors, motors and electrical energy managements. These applications requires good soft magnetic properties that show high permeability, low hysteresis loss, high saturation and low remanent magnetizations, and high Curie temperature. According to VSM results of $(\text{Fe}_{36}\text{Co}_{36}\text{B}_{19.2}\text{Si}_{4.8}\text{Nb}_4)_{99.25}\text{Cu}_{0.75}$ alloy, it can be said that it is a good candidate for these applications.

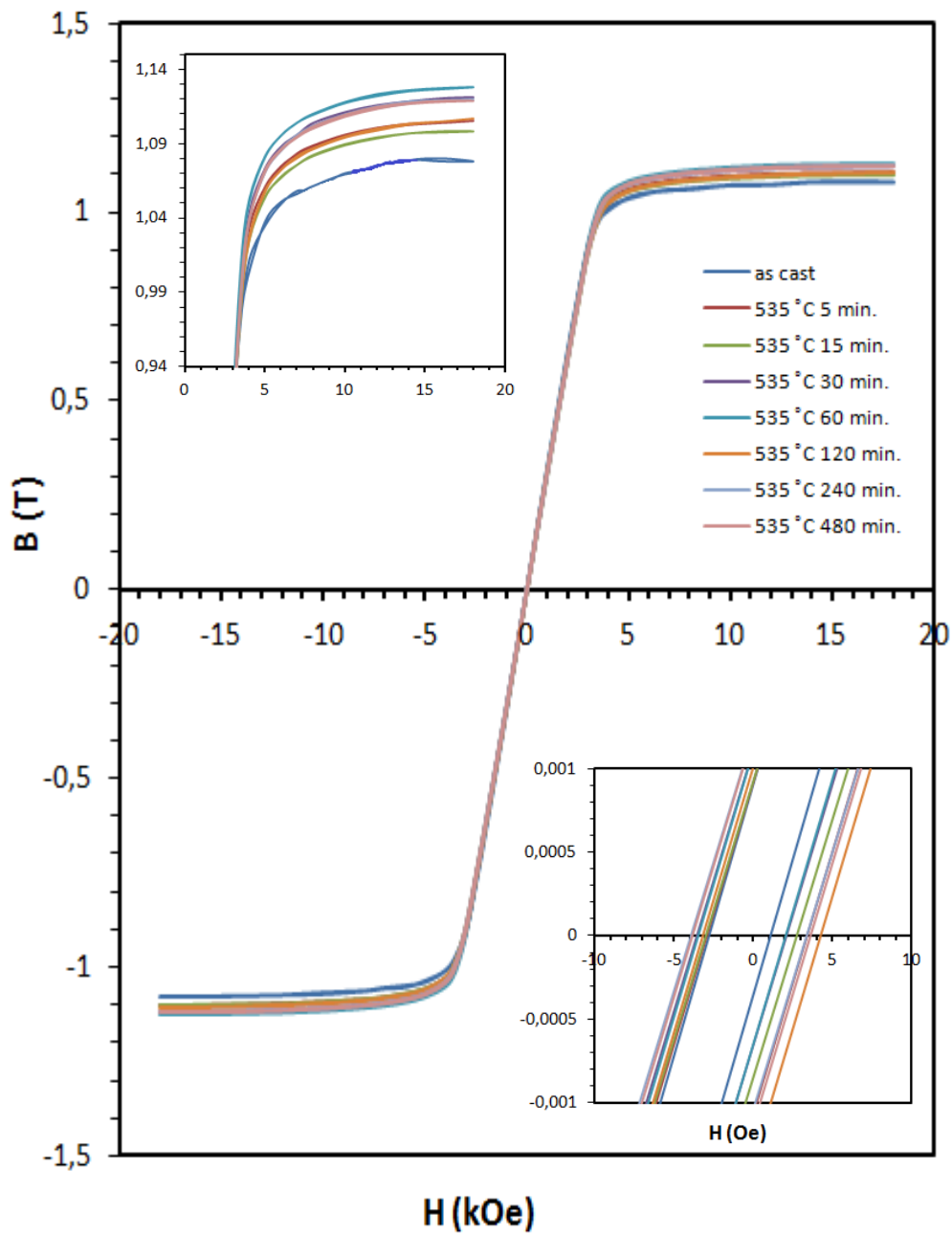


Figure 4.30 B-H loops of the as cast alloy and annealed $(\text{Fe}_{36}\text{Co}_{36}\text{B}_{19.2}\text{Si}_{4.8}\text{Nb}_4)_{99.25}\text{Cu}_{0.75}$ alloys at 535 °C for different holding times. While upper inset shows change of B_s , below inset shows the region around zero field strength.

Table 4.12 H_c , B_s and B_r values of annealed $(Fe_{36}Co_{36}B_{19.2}Si_{4.8}Nb_4)_{99.25}Cu_{0.75}$ alloys at 535 °C for different holding times.

Holding time	H_c (Oe)	B_s (T)	B_r (T)
as cast	1.936	1.0794	0.000632
5 min	3.155	1.1046	0.000993
15 min	2.863	1.0993	0.000888
30 min	2.819	1.1213	0.000884
60 min	2.754	1.1280	0.000879
120 min	3.708	1.1062	0.001182
240 min	3.641	1.1197	0.001128
480 min	3.714	1.1193	0.001170

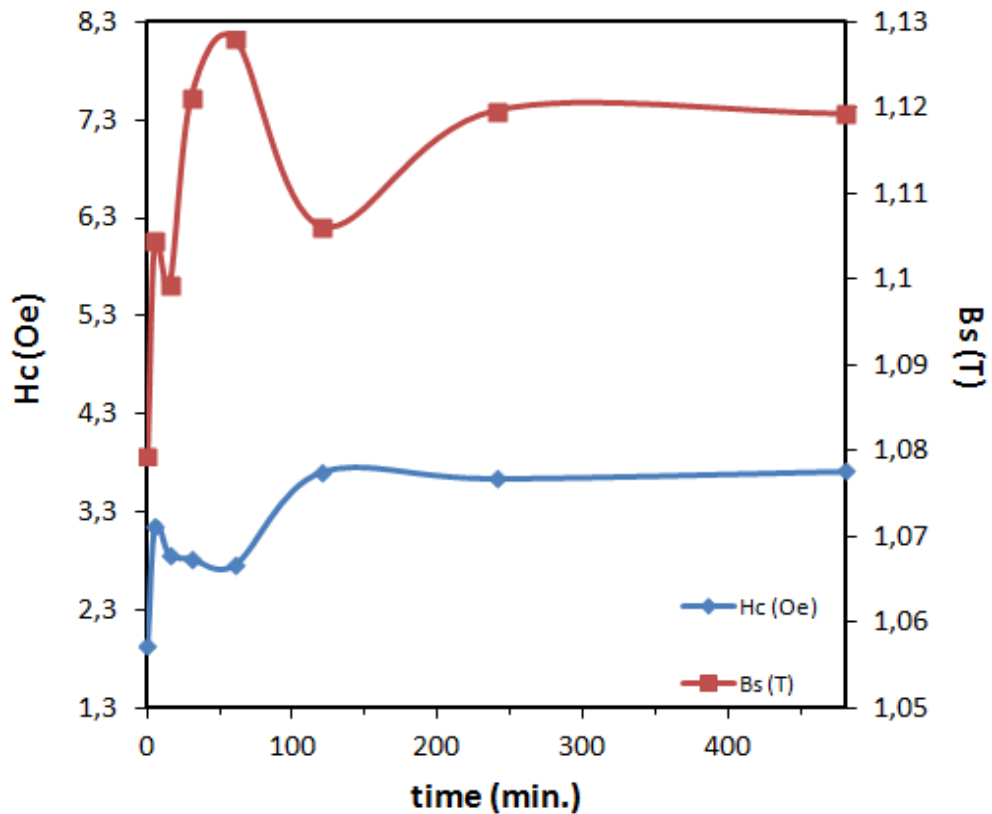


Figure 4.31 Changes of H_c and B_s vs time graph of the annealed $(Fe_{36}Co_{36}B_{19.2}Si_{4.8}Nb_4)_{99.25}Cu_{0.75}$ alloy at 535 °C.

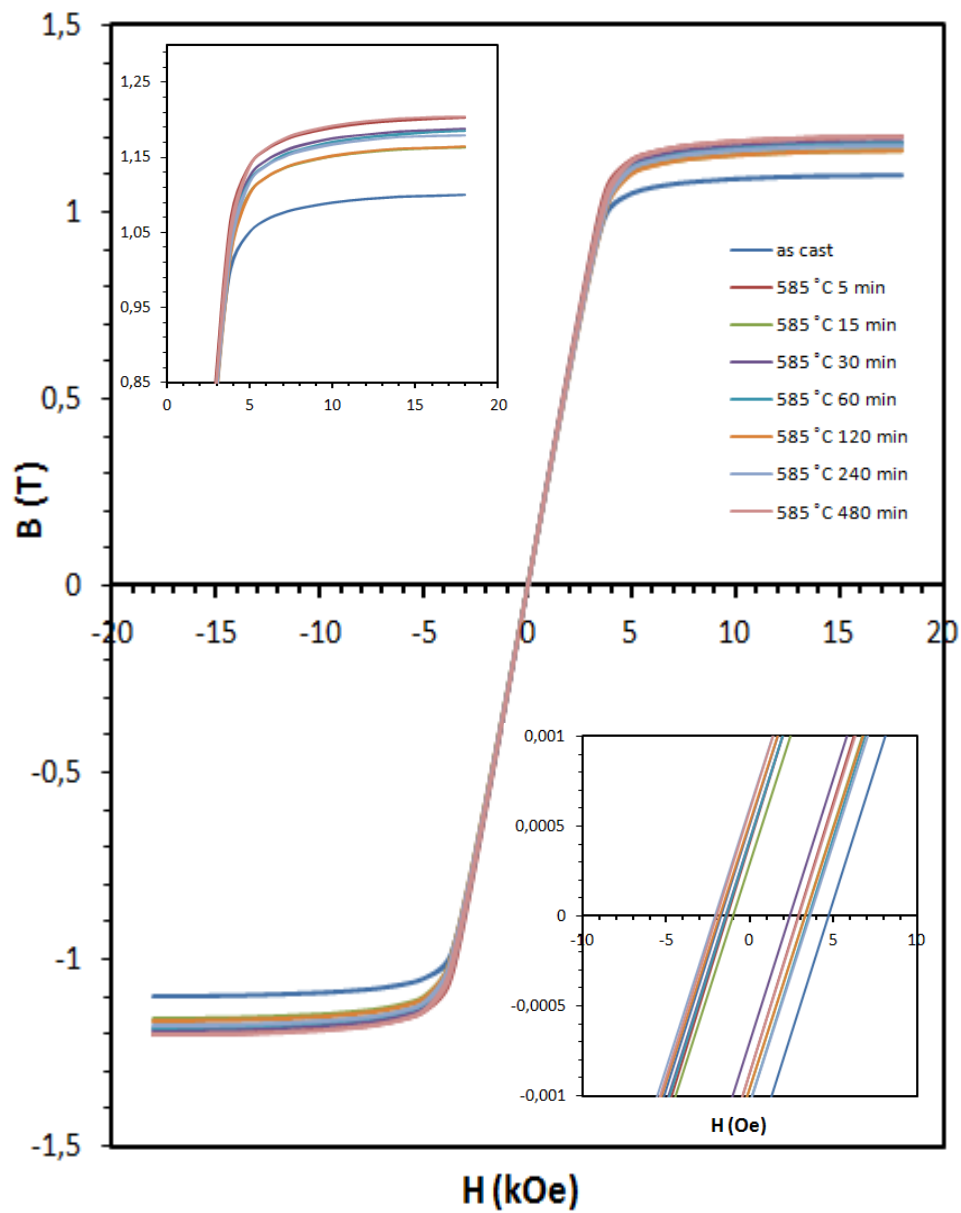


Figure 4.32 B-H loops of the as cast alloy and annealed $(\text{Fe}_{36}\text{Co}_{36}\text{B}_{19.2}\text{Si}_{4.8}\text{Nb}_4)_{99.25}\text{Cu}_{0.75}$ alloys at 585 °C for different holding times. While upper inset shows change of B_s , below inset shows the region around zero field strength.

Table 4.13 H_c , B_s and B_r values of annealed $(Fe_{36}Co_{36}B_{19.2}Si_{4.8}Nb_4)_{99.25}Cu_{0.75}$ alloys at 585 °C for different holding times.

Holding time	H_c (Oe)	B_s (T)	B_r (T)
as cast	3.214	1.1003	0.000947
5 min	2.12	1.2032	0.000639
15 min	2.141	1.1629	0.000625
30 min	1.919	1.1871	0.000562
60 min	2.466	1.1849	0.000731
120 min	2.556	1.1640	0.000739
240 min	2.838	1.1798	0.000823
480 min	2.46	1.2041	0.00073

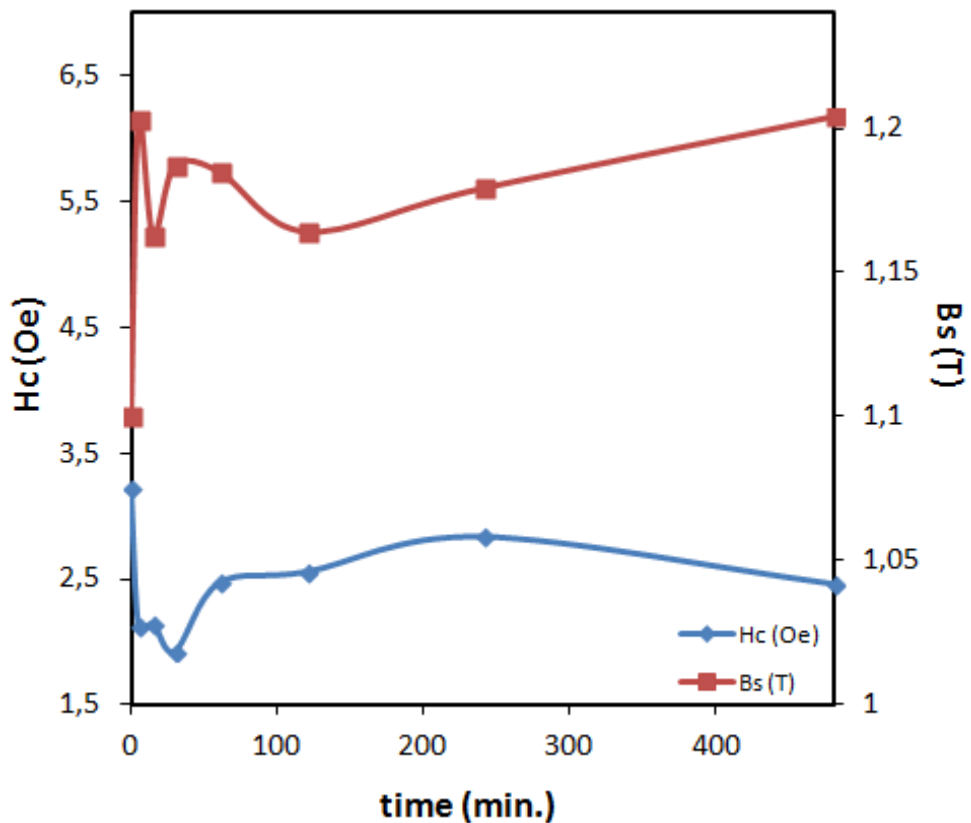


Figure 4.33 Changes of H_c and B_s vs time graph of the annealed $(Fe_{36}Co_{36}B_{19.2}Si_{4.8}Nb_4)_{99.25}Cu_{0.75}$ alloy at 585 °C.

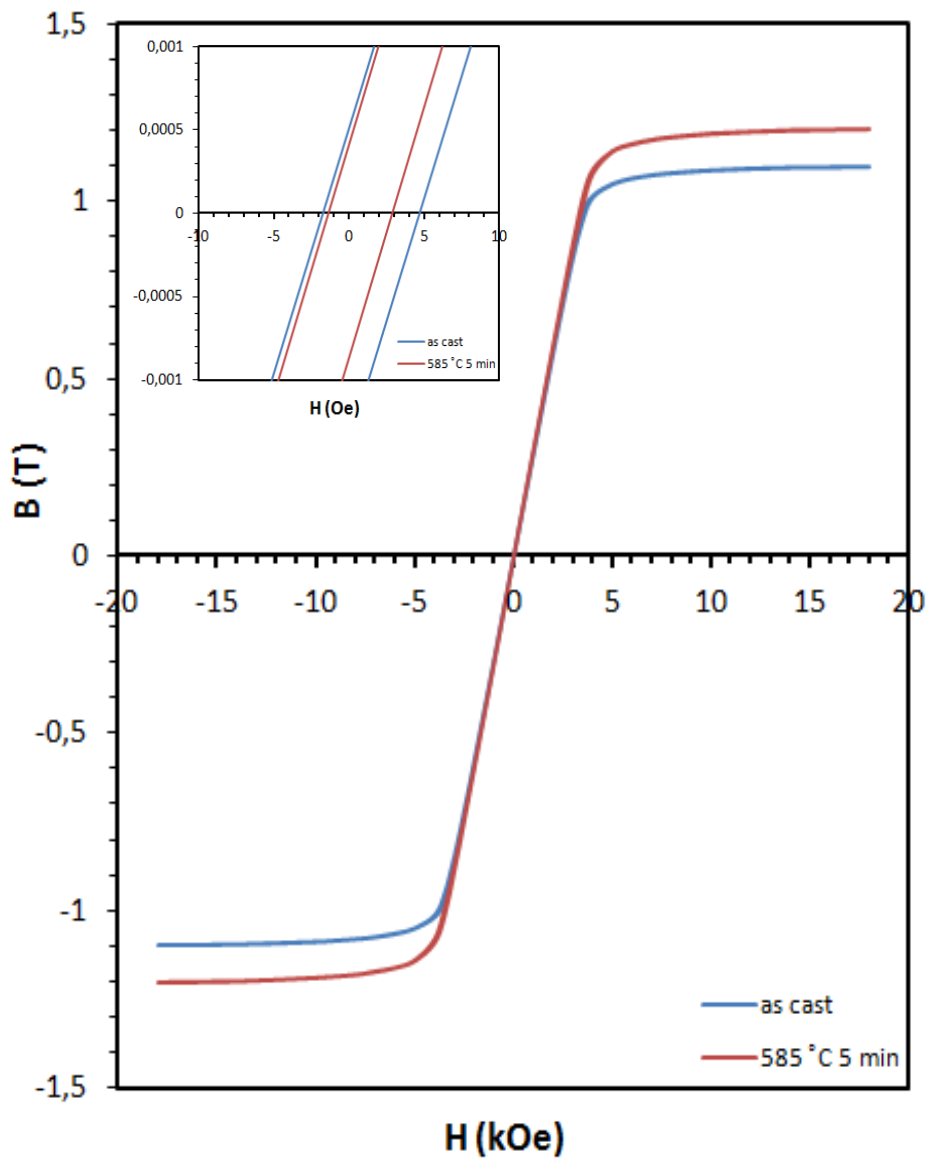


Figure 4.34 B-H loops of the as cast alloy and annealed $(\text{Fe}_{36}\text{Co}_{36}\text{B}_{19.2}\text{Si}_{4.8}\text{Nb}_4)_{99.25}\text{Cu}_{0.75}$ alloy at 585 °C for 5 min. Inset shows the region around zero field strength.

Microhardness Measurements

Fe based bulk metallic glasses have good mechanical properties and they are characterized by a much higher value of microhardness than the equivalent crystalline counterparts. As it can be seen from the Figure 4.35, the average microhardness value for Fe based BMGs is in between 900 to 1300 HV whereas that for their crystalline counterparts is below 600 HV.

On the basis of these informations, the microhardness measurements of the $(\text{Fe}_{36}\text{Co}_{36}\text{B}_{19.2}\text{Si}_{4.8}\text{Nb}_4)_{99.25}\text{Cu}_{0.75}$ alloy were obtained by using Vickers method with the load of 9.8 N and pressure time of 10 seconds. The pattern of the measurements was shown in Figure 4.36 and results of the measurements for both as cast alloy and annealed alloys at 535 °C and 585 °C after 480 min holding time were given in Table 4.14. According to the obtained results, annealed alloys have higher microhardness values than as cast alloys due to the nanocrystalline structures.

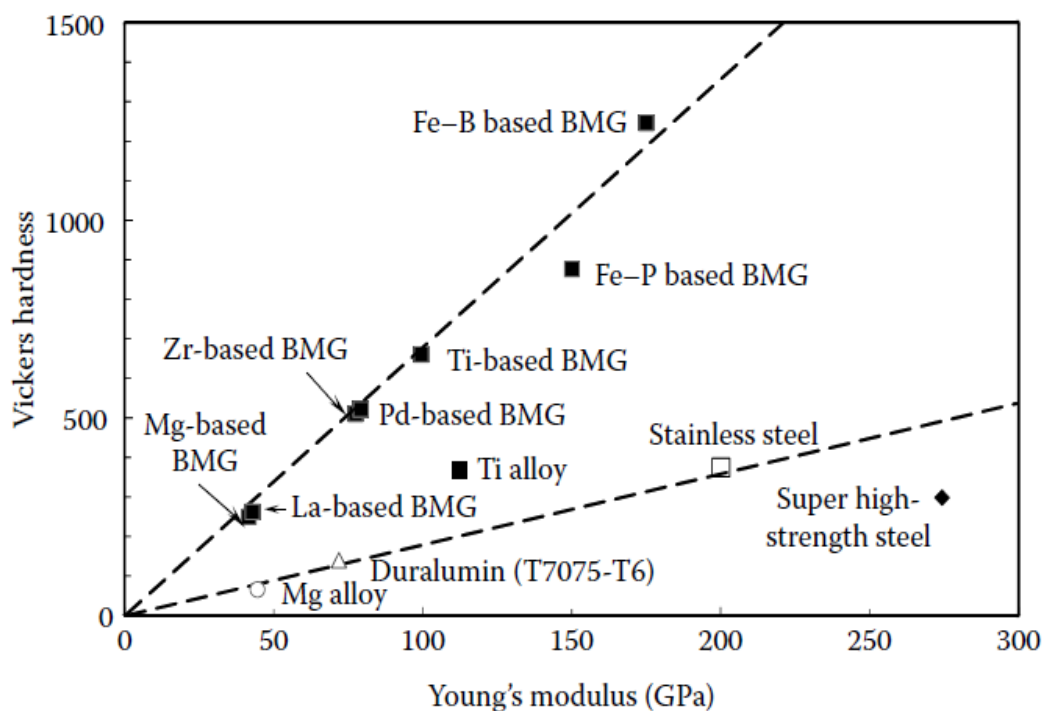


Figure 4.35 Vickers hardness and Young's modulus for some bulk metallic glasses [1].

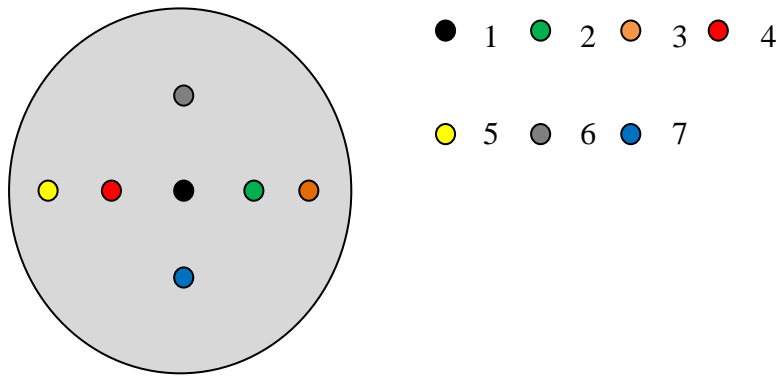


Figure 4.36 Followed pattern of $(\text{Fe}_{36}\text{Co}_{36}\text{B}_{19.2}\text{Si}_{4.8}\text{Nb}_4)_{99.25}\text{Cu}_{0.75}$ alloy for Vickers microhardness measurements.

Table 4.14 Vickers microhardness values of the as cast and annealed $(\text{Fe}_{36}\text{Co}_{36}\text{B}_{19.2}\text{Si}_{4.8}\text{Nb}_4)_{99.25}\text{Cu}_{0.75}$ alloys.

Pattern	Vickers microhardness (HV) for alloy numbered as (1)		Vickers microhardness (HV) for alloy numbered as (10)	
	as cast	at 535 °C	as cast	at 585 °C
1	1005	1090	993	1086
2	1111	1198	963	1213
3	1107	1152	994	1194
4	1038	1062	996	1192
5	1195	1098	963	1178
6	1166	1074	996	1191
7	1142	1052	939	1139

All results shown in Table 4.14 are between 900 and 1300 HV. Thus, results are consistent with the values obtained from Figure 4.35 Vickers hardness vs Young's modulus graphs for Fe based bulk metallic glasses. For observing changing of Vickers hardness of the alloys with respect to followed pattern, graph shown in Figure 4.37 was plotted.

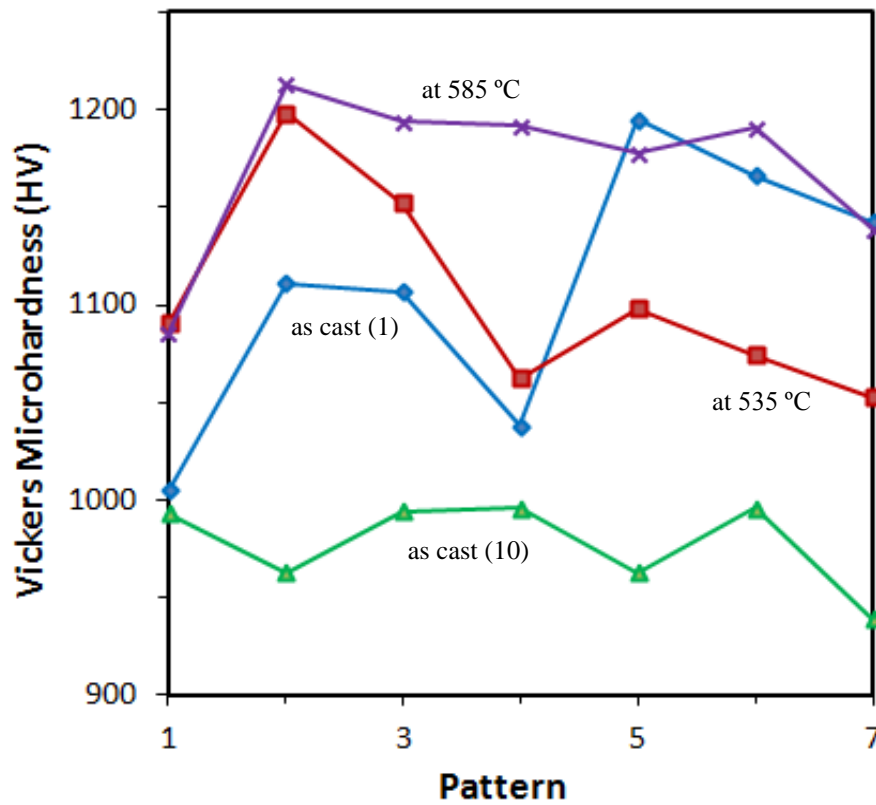


Figure 4.37 Vickers microhardness vs followed pattern graph for $(\text{Fe}_{36}\text{Co}_{36}\text{B}_{19.2}\text{Si}_{4.8}\text{Nb}_4)_{99.25}\text{Cu}_{0.75}$ alloy.

CHAPTER 5

CONCLUSIONS

In this study, the non-equilibrium cooling conditions were supplied by arc melting and suction casting devices and bulk glassy $(\text{Fe}_{36}\text{Co}_{36}\text{B}_{19.2}\text{Si}_{4.8}\text{Nb}_4)_{99.25}\text{Cu}_{0.75}$ rod which has a good soft magnetic property and high electrical resistivity was produced successfully. By isochronal and isothermal DSC analyses, crystallization kinetics of the alloy was also investigated.

In the first part of the study, after characterizations of the as cast bulk glassy $(\text{Fe}_{36}\text{Co}_{36}\text{B}_{19.2}\text{Si}_{4.8}\text{Nb}_4)_{99.25}\text{Cu}_{0.75}$ rod, isochronal DSC experiments were done. Activation energies of glass transition and crystallization events were calculated by the Kissinger and Ozawa methods. When these methods are compared, activation energies estimated by two methods were very close to each other especially the glass transition activation energy which is almost the same. This agreement between two approaches showed that calculated activation energy values were consistent.

Numerous glass forming ability parameters such as T_{rg} , ΔT_x , and γ were estimated for the all samples obtained from isochronal DSC analyses. High majority of them showed that the alloy is a good bulk glass former.

The critical cooling rate (R_c) of the alloy was estimated by using two approaches. First of all, Barandiaran-Colmenero approach was used and R_c was calculated for both onset temperatures of solidification (T_{xc}) obtained from first and second cooling paths of the DSC traces. Values of R_c are 0.17 K/s and 0.15 K/s for first and second T_{xc} respectively. This low values show that the alloy can form glass easily.

However, for rapid solidification cooling rate is about 10^6 K/s, but at least at about 10^4 K/s [24]. Thus, Liu et al. approach was also used for calculation of R_c and it can be seen that results are more consistent with rates of the rapid solidification processing.

In the second part of the study, isothermal DSC experiments were done at temperatures which are above the first crystallization temperature. There were no crystallization signals detected in the isothermal section of the DSC scans except for 585 °C at 5 min holding. Although SEM showed featureless matrix, α -(FeCo) crystallites were distinguished in the XRD pattern and size of these crystallites was estimated by Scherrer equation.

The magnetic and mechanical properties of the as cast and annealed alloys were compared. According to the obtained results, annealed alloys have higher saturation magnetization, low coercive force and high microhardness values than as cast alloys due to the nanocrystalline structures.

REFERENCES

- [1] A. Inoue, Stabilization of metallic supercooled liquid and bulk amorphous alloys, *Acta Materialia* 48 (2000) 279-306.
- [2] C.J. Byrne, M. Eldrup, Bulk metallic glasses, *Science* 321 (2008) 502-503.
- [3] W.L. Johnson, Bulk amorphous metal - an emerging engineering material, *JOM Journal of the Minerals, Metals and Materials Society* 54 (2002) 40-43.
- [4] L. Jörg F, Bulk metallic glasses, *Intermetallics* 11 (2003) 529-540.
- [5] C.A. Schuh, T.C. Hufnagel, U. Ramamurty, Mechanical behavior of amorphous alloys, *Acta Materialia* 55 (2007) 4067-4109.
- [6] W. Wei Hua, The elastic properties, elastic models and elastic perspectives of metallic glasses, *Progress in Materials Science* (2012)
- [7] A. Inoue, Bulk amorphous alloys with soft and hard magnetic properties, *Materials Science and Engineering: A* 226-228 (1997) 357-363.
- [8] F. Li, T. Zhang, A. Inoue, S. Guan, N. Shen, (Fe,Co)-Zr-Nd-B bulk amorphous alloys with good soft magnetic properties, *Intermetallics* 12 (2004) 1139-1142.
- [9] S.J. Pang, T. Zhang, K. Asami, A. Inoue, Synthesis of Fe-Cr-Mo-C-B-P bulk metallic glasses with high corrosion resistance, *Acta Materialia* 50 (2002) 489-497.

- [10] L. Wang, Y. Chao, Corrosion behavior of $\text{Fe}_{41}\text{Co}_7\text{Cr}_{15}\text{Mo}_{14}\text{C}_{15}\text{B}_6\text{Y}_2$ bulk metallic glass in NaCl solution, *Materials Letters* 69 (2012) 76-78.
- [11] A. Inoue, B.L. Shen, C.T. Chang, Fe and Co-based bulk glassy alloys with ultrahigh strength of over 4000 MPa, *Intermetallics* 14 (2006) 936-944.
- [12] A. Inoue, B.L. Shen, C.T. Chang, Super-high strength of over 4000 MPa for Fe-based bulk glassy alloys in $[(\text{Fe}_{1-x}\text{Co}_x)_{0.75}\text{B}_{0.2}\text{Si}_{0.05}]_{96}\text{Nb}_4$ system, *Acta Materialia* 52 (2004) 4093-4099.
- [13] M. Aykol, M.V. Akdeniz, A.O. Mekhrabov, Solidification behavior, glass forming ability and thermal characteristics of soft magnetic Fe-Co-B-Si-Nb-Cu bulk amorphous alloys, *Intermetallics*, 19 (2011) 1330-1337.
- [14] W. Klement, R. H. Willens and P. Duwez, Non-crystalline Structure in Solidified Gold-Silicon Alloys, *Nature*, 187 (1960) 869-870.
- [15] A.L. Greer, Metallic glasses, *Science*, 267 (1995) 1947-1953.
- [16] W. H. Wang, C. Dong and C. H. Shek, Bulk metallic glasses, *Material Science and Engineering R*, 44 (2004) 45-89.
- [17] H. Chen, D. Turnbull, Evidence of a glass-liquid transition in a gold-germanium-silicon alloy, *The Journal of Chemical Physics*, 48 (1968) 2560-2571.
- [18] D. Turnbull, M.H. Cohen, Free-volume model of the amorphous phase: glass transition, *The Journal of Chemical Physics*, 34 (1961) 120-125.
- [19] A. J. Drehman, A. L. Greer, and D. Turnbull, Bulk Formation of a Metallic-Glass $\text{Pd}_{40}\text{Ni}_{40}\text{P}_{20}$, *Applied Physics Letters*, 41 (1982) 716-717.

- [20] H. W. Kui, A. L. Greer and D. Turnbull, Formation of Bulk Metallic Glass by Fluxing, *Applied Physics Letters*, 45 (1984) 615-616.
- [21] F.E. Luborsky 1983. Amorphous Metallic Alloys. Pages 1-7 in F.E. Luborsky, ed., *Amorphous Metallic Alloys*, Butterworths, London, 1983.
- [22] M.L. Hair, A.M. Filbert in *Encyclopedia of Material Science and Engineering* Ed. By M. B. Bever, Vol.3, Pergamon Press, Oxford, UK, 1988.
- [23] J. C. Dyre, Colloquium: The glass transition and elastic models of glass forming liquids, *Reviews of Modern Physics*, 78 (2006) 953-972.
- [24] C. Suryanarayana, A. Inoue, *Bulk metallic glasses*, CRC Press, 2011.
- [25] C.A. Angell, Formation of glasses from liquids and biopolymers, *Science*, 267 (1995) 1924-1935.
- [26] A. Inoue and A. Takeuchi, Recent progress in bulk glassy, nanoquasicrystalline and nanocrystalline alloys, *Materials Science and Engineering A*, 375-377 (2004) 16-30.
- [27] A. Inoue, T. Zhang and T. Masumoto, Glass-forming ability of alloys, *Journal of Non-Crystalline Solids*, 156-158 (1993) 473-480.
- [28] D. Turnbull, J.C. Fisher, Rate of Nucleation in Condensed Systems, *Journal of Chemical Physics*, 17 (1949) 71-73.
- [29] D. Turnbull, Under What Conditions Can a Glass be Formed?, *Contemporary Physics*, 10 (1969) 473-488.

- [30] A. Hruby, Evaluation of glass-forming tendency by means of DTA, Czechoslovak Journal of Physics, 22 (1972) 1187-1193.
- [31] M. Saad, M. Poulain, Glass Formation Ability Criterion, Material Science Forum, 19-20 (1987) 11-18.
- [32] G. J. Fan, H. Choo and P. K. Liaw, A new criterion for the glass-forming ability of liquids, Journal of Non-Crystalline Solids, 353 (2007) 102-107.
- [33] Z. Lu, C. Liu, A new glass-forming ability criterion for bulk metallic glasses, Acta Materialia, 50 (2002) 3501-3512.
- [34] Z. P. Lu and C. T. Liu, A new approach to understanding and measuring glass formation in bulk amorphous materials, Intermetallics 12 (2004) 1035-1043.
- [35] X.H. Du, J.C. Huang, C.T. Liu, Z.P. Lu, New criterion of glass forming ability for bulk metallic glasses, Journal of Applied Physics, 101 (2007) 086108-1–086108-3.
- [36] Q.J. Chen, J. Shen, H.B. Fan, J.F. Sun, Y.J. Huang, and D.G. McCartney, Glass-forming ability of an iron-based alloy enhanced by Co addition and evaluated by a new criterion, Chin. Phys. Lett., 22 (2005) 1736–1738.
- [37] Q.J. Chen, J. Shen, D. Zhang, H.B. Fan, J.F. Sun, and D.G. McCartney, A new criterion for evaluating the glass-forming ability of bulk metallic glasses, Mater. Sci. Eng. A, 433 (2006) 155–160.
- [38] K. Mondal, B. Murty, On the parameters to assess the glass forming ability of liquids, Journal of Non-Crystalline Solids, 351 (2005) 1366-1371.

- [39] Z. Long, G. Xie, H. Wei, X. Su, J. Peng, P. Zhang, A. Inoue, On the new criterion to assess the glass-forming ability of metallic alloys, *Materials Science and Engineering: A*, 509 (2009) 23-30.
- [40] J.H. Kim, J.S. Park, H.K. Lim, W.T. Kim, and D.H. Kim, Heating and cooling rate dependence of the parameters representing the glass forming ability in bulk metallic glasses, *J. Non-Cryst. Solids*, 351 (2005) 1433–1440.
- [41] Z.-Z. Yuan, S.-L. Bao, Y. Lu, D.-P. Zhang, and L. Yao, A new criterion for evaluating the glass-forming ability of bulk glass forming alloys. *J. Alloys Compd.* 459 (2008) 251–260.
- [42] G. Sheng, C.T. Liu, New glass forming ability criterion derived from cooling consideration, *Intermetallics*, 18 (2010) 2065-2068.
- [43] B. Majumdar and D. Akhtar, Synthesis and crystallization of Fe-Co-Ni-Zr(Nb)-B bulk glasses, *Materials Science and Technology*, 21 (2005) 1139-1144.
- [44] A. Inoue, Y. Shinohara, Y. Yokoyama, and T. Masumoto, Solidification analyses of bulky $Zr_{60}Al_{10}Ni_{10}Cu_{15}Pd_5$ glass produced by casting into wedge shape copper mold, *Mater. Trans., JIM* 36 (1995) 1276–1281.
- [45] A. Inoue, *Bulk Amorphous Alloys: Preparation and Fundamental characteristics*, Trans. Tech. Public. Ltd., Switzerland, 1998.
- [46] A. Inoue, and T. Zhang, Fabrication of bulky Zr-based glassy alloys by suction casting into copper mold, *Mater. Trans., JIM* 36 (1995) 1184–1187.

- [47] I.A. Figueroa, P.A. Carroll, H.A. Davies, H. Jones, and I. Todd, Preparation of Cu-based bulk metallic glasses by suction casting, In SP-07, Proceedings of the Fifth Decennial International Conference on Solidification Processing, Sheffield, U.K., July 2007, 479–482.
- [48] X. Gu, L.Q. Xing, and T.C. Hufnagel, Glass-forming Ability and Crystallization of Bulk Metallic Glass $(\text{Hf}_x\text{Zr}_{1-x})_{52.5}\text{Cu}_{17.9}\text{Ni}_{14.6}\text{Al}_{10}\text{Ti}_5$, J. Non-Cryst. Solids, 311 (2002) 77–82.
- [49] M.K. Pehlivanoglu, M.V. Akdeniz and A.Ş. Bor, Structural Characterization of Iron-Based Bulk Metallic Glass Alloys Produced by Centrifugal Casting, Chemical Engineering Communications, 190 (2003) 925-935.
- [50] M.V. Akdeniz, A.O. Mekhrabov, M.K. Pehlivanoglu, Solidification Behaviour of Bulk Glass-Forming Alloy Systems, Journal of alloys and compounds, 386 (2005) 185-191.
- [51] A.N. Kolmogorov, A statistical theory for the recrystallization of metals, Izvestia Akademia Nauk Serie Mathematica SSSR, 1 (1937) 355-359.
- [52] W.A. Johnson and R.F. Mehl, Reaction kinetics in processes of nucleation and growth, Transactions of American Institute of Mining, Metallurgical and Petroleum Engineers, 135 (1939) 416-458.
- [53] M. Avrami, Kinetics of Phase Change I, Journal of Chemical Physics, 7 (1939) 1103-1112.
- [54] H.E. Kissinger, Reaction Kinetics in Differential Thermal Analysis, Analytical Chemistry, 29 (1957) 1702-1706.

- [55] T. Ozawa, A new method of analyzing thermogravimetric data, *Bulletin Chemical Society of Japan*, 38 (1965) 1881-1886.
- [56] D.W. Henderson, Experimental analysis of non-isothermal transformations involving nucleation and growth, *J. Therm Anal*, 15 (1979) 325-331.
- [57] P. Shepilovm, D.S. Baik, Computer simulation of crystallization kinetics for the model with simultaneous nucleation of randomly-oriented ellipsoidal crystals, *J. Non-Cryst Solids*, 171 (1994) 141-156.
- [58] T. Wang, X. Yang and Q. Li, Effect of Cu and Nb additions on crystallization kinetics of $\text{Fe}_{80}\text{P}_{13}\text{C}_7$ bulk metallic glasses, *Thermochimica Acta*, 579 (2014) 9-14.
- [59] Duman N. 2012. Magnetic Monitoring Approach to Kinetics of Phase Transformations in Multicomponent Alloy Systems, Ankara , Ph.D. Thesis, Middle East Technical University, 222 p.
- [60] J.W. Christian, *The theory of transformations in metals and alloys*, (1981).
- [61] A. Takeuchi and A. Inoue, Quantitative evaluation of critical cooling rate for metallic glasses, *Materials Science and Engineering A*, 304-306 (2001) 446- 451.
- [62] D. R. Uhlmann, A kinetic treatment of glass formation, *Journal of Non-Crystalline Solids*, 7 (1972) 337-348.
- [63] P.I.K. Onorato, and D.R. Uhlmann, Nucleating heterogeneities and glass formation, *J. Non-Cryst. Solids*, 22 (1976) 367–378.
- [64] J. M. Barandiaran and J. Colmenero, Continuous cooling approximation for the formation of a glass, *Journal of Non-Crystalline Solids*, 46 (1981) 277-287.

- [65] H.A. Davies, 1983. Metallic glass formation. In *Amorphous Metallic Alloys*, ed. F.E. Luborsky, pp. 8–25. London, U.K.: Butterworths.
- [66] C. S. Ray, S. T. Reis, R. K. Brow, W. Holand and V. Rheinberger, A new DTA method for measuring critical cooling rate for glass formation, *Journal of Non-Crystalline Solids*, 351 (2005) 1350-1358.
- [67] X.H. Lin and W.L. Johnson, Formation of Ti–Zr–Cu–Ni bulk metallic glasses, *J. Appl. Phys.*, 78 (1995) 6514–6519.
- [68] M. F. Ashby and A. L. Greer, Metallic glasses as structural materials, *Scripta Materialia* 54 (2006) 321-326.
- [69] Mermer E. 2013. Synthesis and Characterization of Copper Based Bulk Amorphous Alloys, Ankara , MSc. Thesis, Middle East Technical University, 59 p.
- [70] A. Inoue and J.S. Gook, Fe-based ferromagnetic glassy alloys with wide supercooled liquid region. *Mater. Trans., JIM* 36 (1995) 1180–1183.
- [71] B.L. Shen and A. Inoue, Fabrication of large-size Fe-based glassy cores with good soft magnetic properties by spark plasma sintering, *J. Mater. Res.* 18 (2003) 2115–2121.
- [72] B.L. Shen and A. Inoue, Soft magnetic properties of bulk nanocrystalline Fe–Co–B–Si–Nb–Cu alloy with high saturated magnetization of 1.35 T., *J. Mater. Res.* 19 (2004) 2549–2552.
- [73] L.Xing, J.Eckert, W.Löser, S. Roth, L. Schultz, Atomic ordering and magnetic properties in $\text{Nd}_{57}\text{Fe}_{20}\text{B}_8\text{Co}_5\text{Al}_{10}$ solids, *Journal of Applied Physics*, 88 (2000) 3565-3569.

- [74] A. Inoue, T. Zhang, A. Takeuchi, W. Zhang, Hard magnetic bulk amorphous Nd-Fe-Al alloys of 12 mm in diameter made by suction casting, *Materials Transactions, JIM (Japan)*, 37 (1996) 636-640.
- [75] B.C. Wei, Y. Zhang, Y.X. Zhuang, D.Q. Zhao, M.X. Pan, W.H. Wang, W.R. Hu, Nd₆₅Al₁₀Fe_{25-x}Co_x (x= 0, 5, 10) bulk metallic glasses with wide supercooled liquid regions, *Journal of Applied Physics*, 89 (2001) 3529-3531.
- [76] A. Inoue, Bulk amorphous alloys with soft and hard magnetic properties, *Materials Science and Engineering: A*, 226 (1997) 357-363.
- [77] A. Inoue, T. Zhang, H. Koshiba, A. Makino, New bulk amorphous Fe-(Co, Ni)-M-B (M= Zr, Hf, Nb, Ta, Mo, W) alloys with good soft magnetic properties, *Journal of applied physics*, 83 (1998) 6326-6328.
- [78] T. Shen, R. Schwarz, Bulk ferromagnetic glasses in the Fe-Ni-P-B system, *Acta materialia*, 49 (2001) 837-847.
- [79] S.F. Guo, Z.Y. Wy, and L. Liu, Preparation and magnetic properties of FeCoHfMoBY bulk metallic glasses, *J. Alloys Compd.* 468 (2009) 54-57.
- [80] L. Kraus, V. Haslar, and P. Duhaj, Correlation between saturation magnetization, magnetostriction and creep-induced anisotropy in amorphous (FeCo)₈₅B₁₅ alloys, *IEEE Trans. Mag.* 30 (1994) 530-532.
- [81] D.Y. Liu, W.S. Sun, H.F. Zhang, and Z.Q. Hu, Preparation, thermal stability and magnetic properties of Fe-Co-Ni-Zr-Mo-B bulk metallic glass, *Intermetallics* 12 (2004) 1149-1152.

- [82] S. Sharma, and C. Suryanarayana, Effect of Nb on the glass-forming ability of mechanically alloyed Fe–Ni–Zr–B alloys, *Scr. Mater.* 58 (2008) 508–511.
- [83] C.T. Chang, B.L. Shen, and A. Inoue, Co–Fe–B–Si–Nb bulk glassy alloys with superhigh strength and extremely low magnetostriction, *Appl. Phys. Lett.* 88 (2006) 011901-1–011901-3.
- [84] C.T. Chang, B.L. Shen, and A. Inoue, FeNi-based bulk glassy alloys with superhigh mechanical strength and excellent soft-magnetic properties, *Appl. Phys. Lett.* 89 (2006) 051912-1–051912-3.
- [85] P. Pawlik, and H.A. Davies, The bulk glass forming abilities and mechanical and magnetic properties of Fe–Co–Zr–Mo–W–B alloys, *J. Non-Cryst. Solids* 329 (2003) 17–21.
- [86] Y. Yoshizawa, S. Oguma, and K. Yamauchi, New Fe-based soft magnetic alloys composed of ultrafine grain structure, *J. Appl. Phys.* 64 (1988) 6044–6046.
- [87] A. Inoue, B.L. Shen, and T. Ohsuna, Soft magnetic properties of nanocrystalline Fe–Si–B–Nb–Cu rod alloys obtained by crystallization of cast amorphous phase, *Mater. Trans.* 43 (2002) 2337–2341.
- [88] A. Makino, H. Men, T. Kubota, K. Yubuta, and A. Inoue, FeSiBPCu nanocrystalline soft magnetic alloys with high Bs of 1.9 Tesla produced by crystallizing hetero-amorphous phase, *Mater. Trans.* 50 (2009) 204–209.
- [89] A. Makino, H. Men, T. Kubota, K. Yubuta, and A. Inoue, New Fe-metalloids based nanocrystalline alloys with high Bs of 1.9 T and excellent magnetic softness, *J. Appl. Phys.* 105 (2009) 07A308-1–07A308-3.
- [90] T. Masumoto, K. Hashimoto, CORROSION PROPERTIES OF AMORPHOUS METALS, *Journal de Physique Colloques*, 41 (C8) (1980) C8-894-C8-900.
- [91] A. Inoue and A. Takeuchi, Recent development and application products of bulk glassy alloys, *Acta Materialia*, 59 (2011) 2243- 2267.

- [92] T. Sourmail, *Prog. Mater. Sci.* 50 (2005) 816.
- [93] B. Shen, A. Inoue, C. Chang, *Appl. Phys. Lett.* 85 (2004) 4911.
- [94] M. Aykol, A.O. Mekhrabov, M.V. Akdeniz, Nano-scale phase separation in amorphous Fe-B alloys: Atomic and cluster ordering, *Acta Materialia*, 57 (2009) 171-181.
- [95] F. Kong, B. Shen, A. Makino, A. Inoue, Enhancement of soft magnetic properties of FeCoNbB nanocrystalline alloys with Cu and Ni additions, *Thin Solid Films* 519 (2011) 8280-8282.
- [96] H. Ryusuke, *Advances in amorphous and nanocrystalline magnetic materials*, *Journal of Magnetism and Magnetic Materials* 304 (2006) 187-191.
- [97] B. Shen, C. Chang, A. Inoue, *Intermetallics* 15 (2007) 9.
- [98] Y. Yoshizawa, E. Kakimoto, K. Doke, *Mater. Sci. Eng. A* (2007) 449-451.
- [99] *ASM Metals Handbook, Alloy Phase Diagrams, Volume 3.*
- [100] H. Okamoto, *Phase Equilib. Diff.* 25 (2004) 297.

APPENDICES

APPENDIX A

EDS ANALYSES

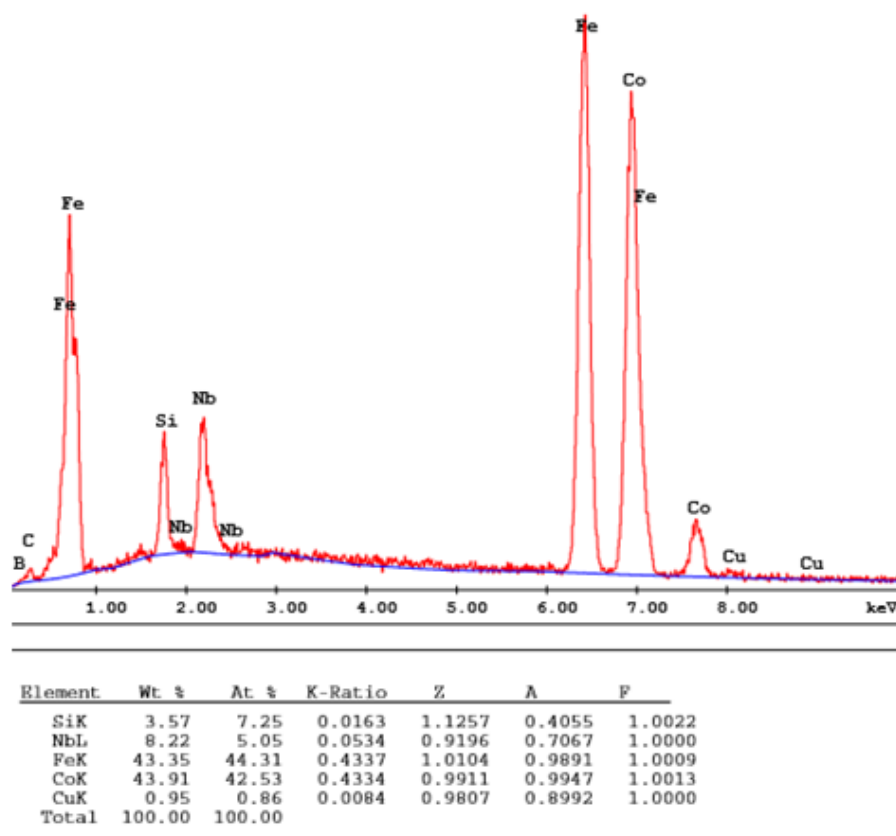


Figure A.1 EDS analysis of bulk amorphous $(\text{Fe}_{36}\text{Co}_{36}\text{B}_{19.2}\text{Si}_{4.8}\text{Nb}_4)_{99.25}\text{Cu}_{0.75}$ alloy.

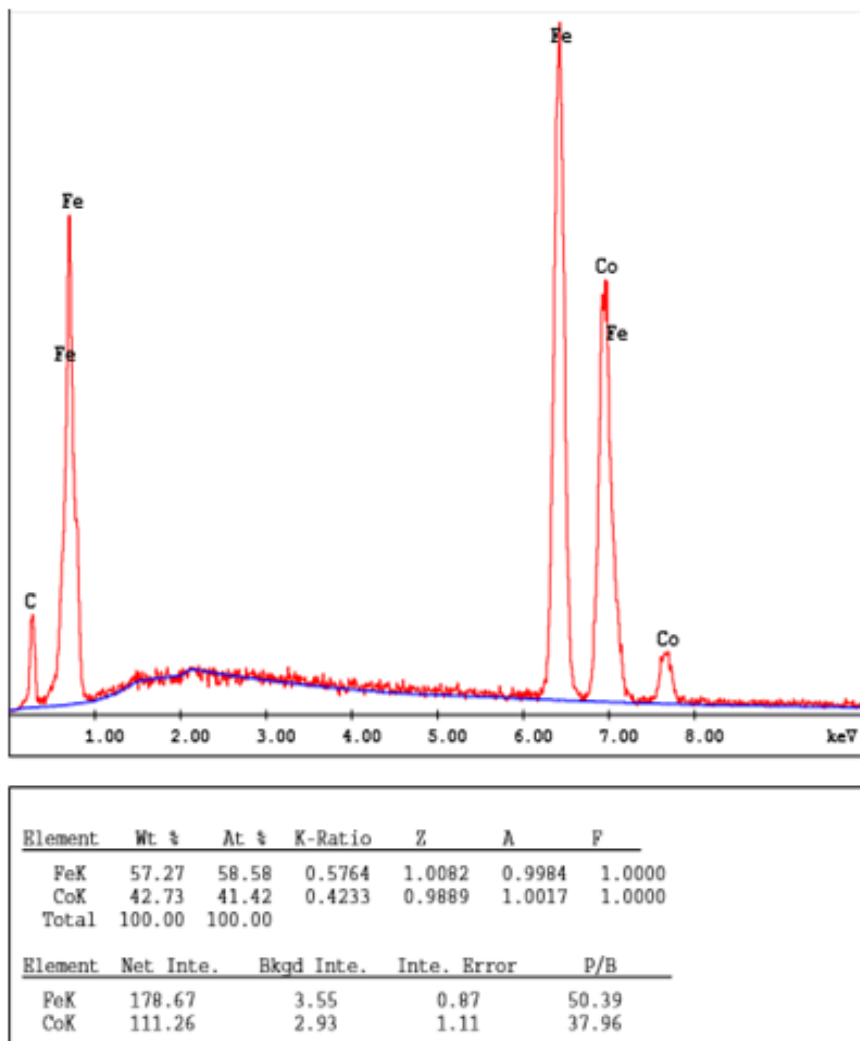


Figure A.2 EDS analysis of dendrites stated as dark for the head part of the bulk amorphous $(\text{Fe}_{36}\text{Co}_{36}\text{B}_{19.2}\text{Si}_{4.8}\text{Nb}_4)_{99.25}\text{Cu}_{0.75}$ alloy.

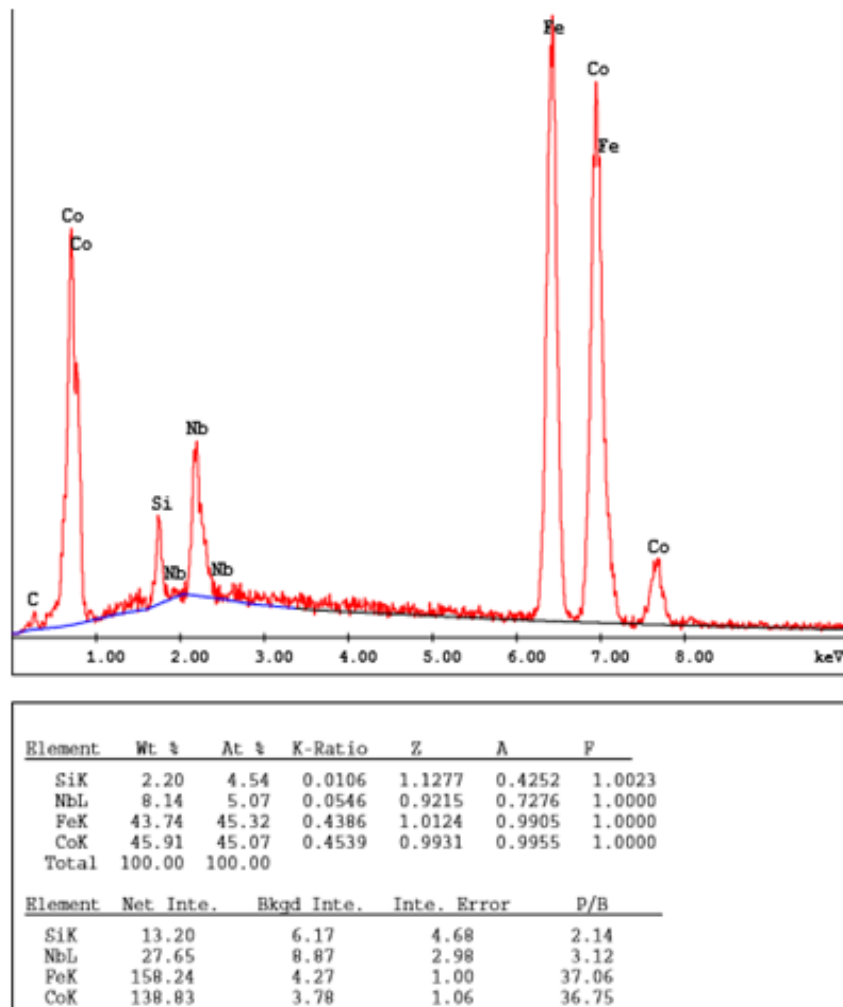


Figure A.3 EDS analysis of dendrites stated as light for the head part of the bulk amorphous $(\text{Fe}_{36}\text{Co}_{36}\text{B}_{19.2}\text{Si}_{4.8}\text{Nb}_4)_{99.25}\text{Cu}_{0.75}$ alloy.

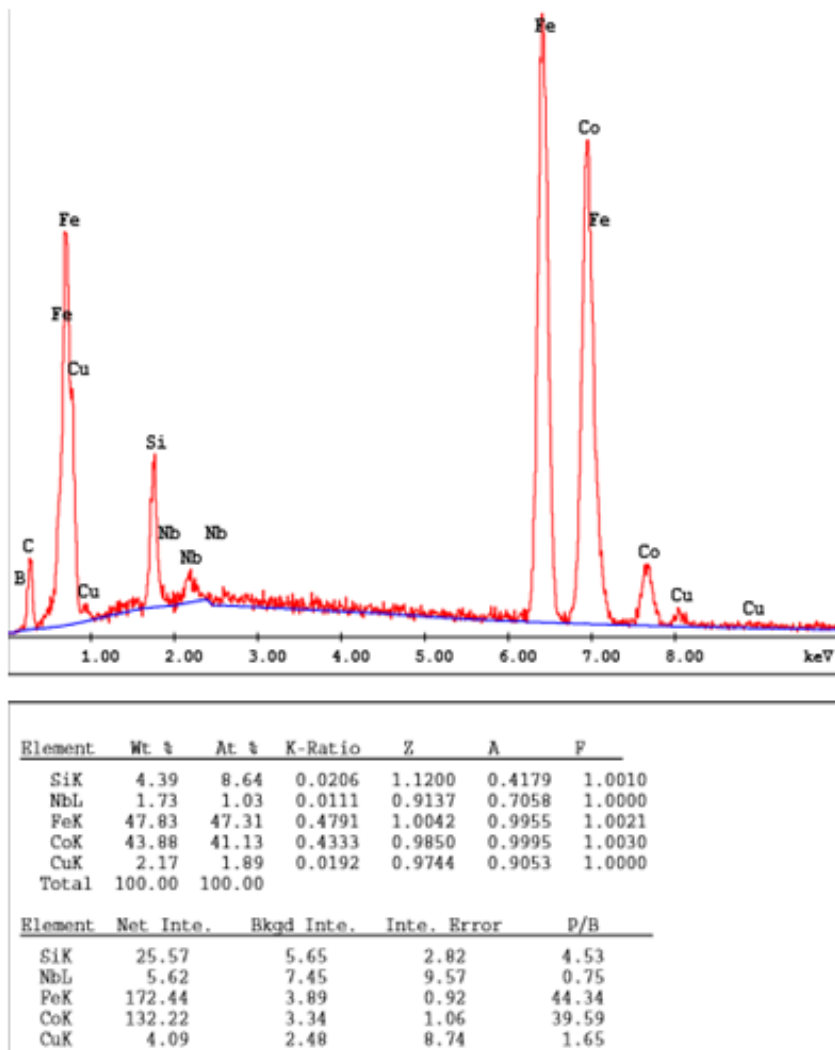


Figure A.4 EDS analysis of dendrites stated as gray for the head part of the bulk amorphous $(\text{Fe}_{36}\text{Co}_{36}\text{B}_{19.2}\text{Si}_{4.8}\text{Nb}_4)_{99.25}\text{Cu}_{0.75}$ alloy.

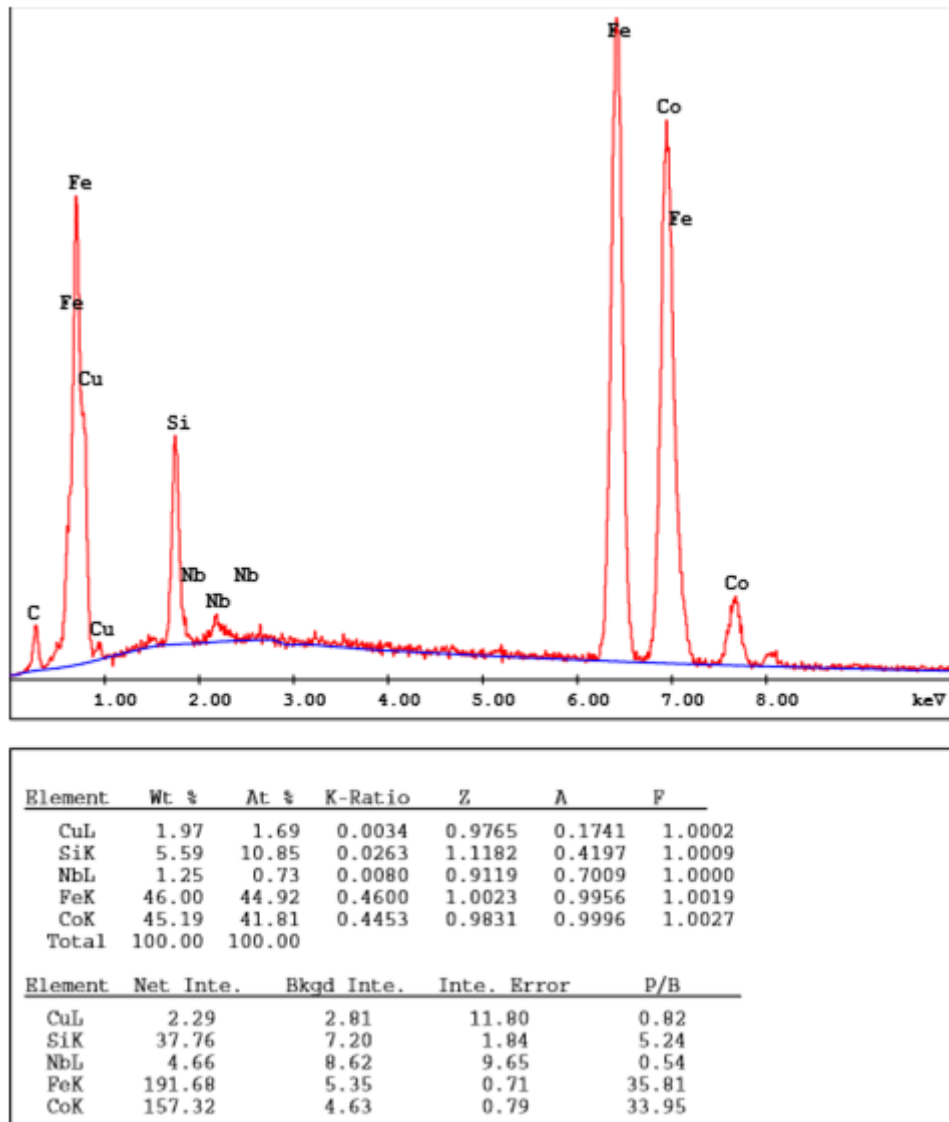
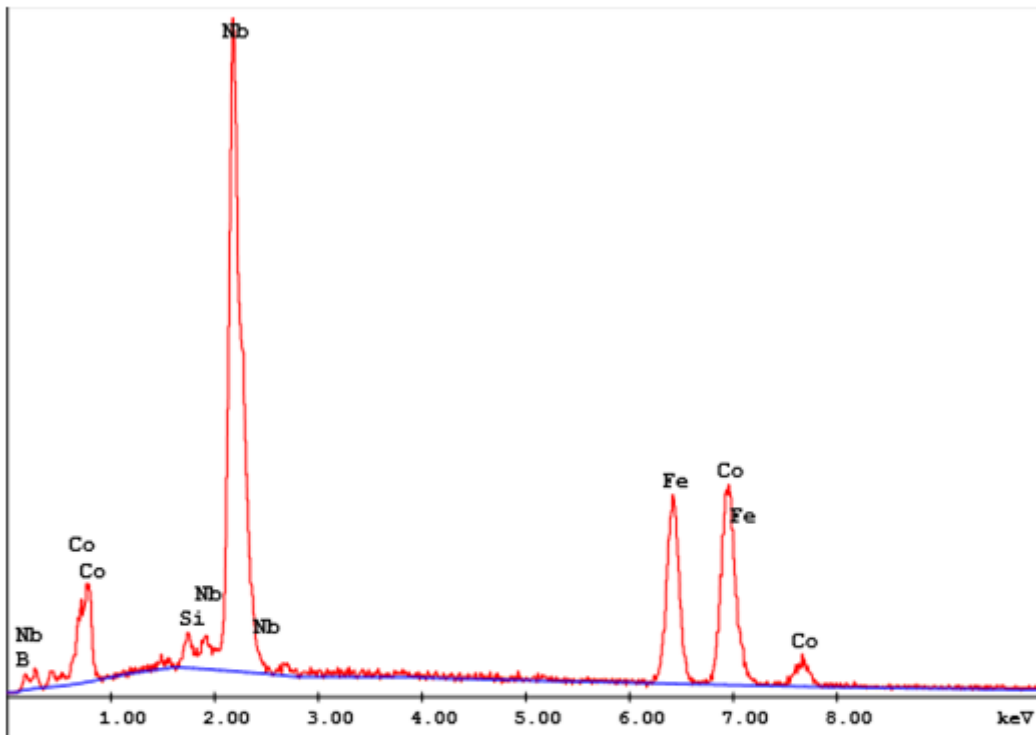


Figure A.5 EDS analysis of eutectics stated as dark for the head part of the bulk amorphous $(\text{Fe}_{36}\text{Co}_{36}\text{B}_{19.2}\text{Si}_{4.8}\text{Nb}_4)_{99.25}\text{Cu}_{0.75}$ alloy.



Element	Wt %	At %	K-Ratio	Z	A	F
SiK	1.25	3.09	0.0076	1.1576	0.5142	1.0123
NbL	48.14	35.93	0.3821	0.9534	0.8326	1.0000
FeK	21.95	27.25	0.2197	1.0456	0.9572	1.0000
CoK	28.66	33.72	0.2850	1.0266	0.9689	1.0000
Total	100.00	100.00				

Element	Net Inte.	Bkgd Inte.	Inte. Error	P/B
SiK	12.60	11.24	5.77	1.12
NbL	259.02	10.88	0.79	23.81
FeK	106.16	6.75	1.26	15.73
CoK	116.79	5.77	1.19	20.24

Figure A.6 EDS analysis of eutectics stated as light for the head part of the bulk amorphous $(\text{Fe}_{36}\text{Co}_{36}\text{B}_{19.2}\text{Si}_{4.8}\text{Nb}_4)_{99.25}\text{Cu}_{0.75}$ alloy.

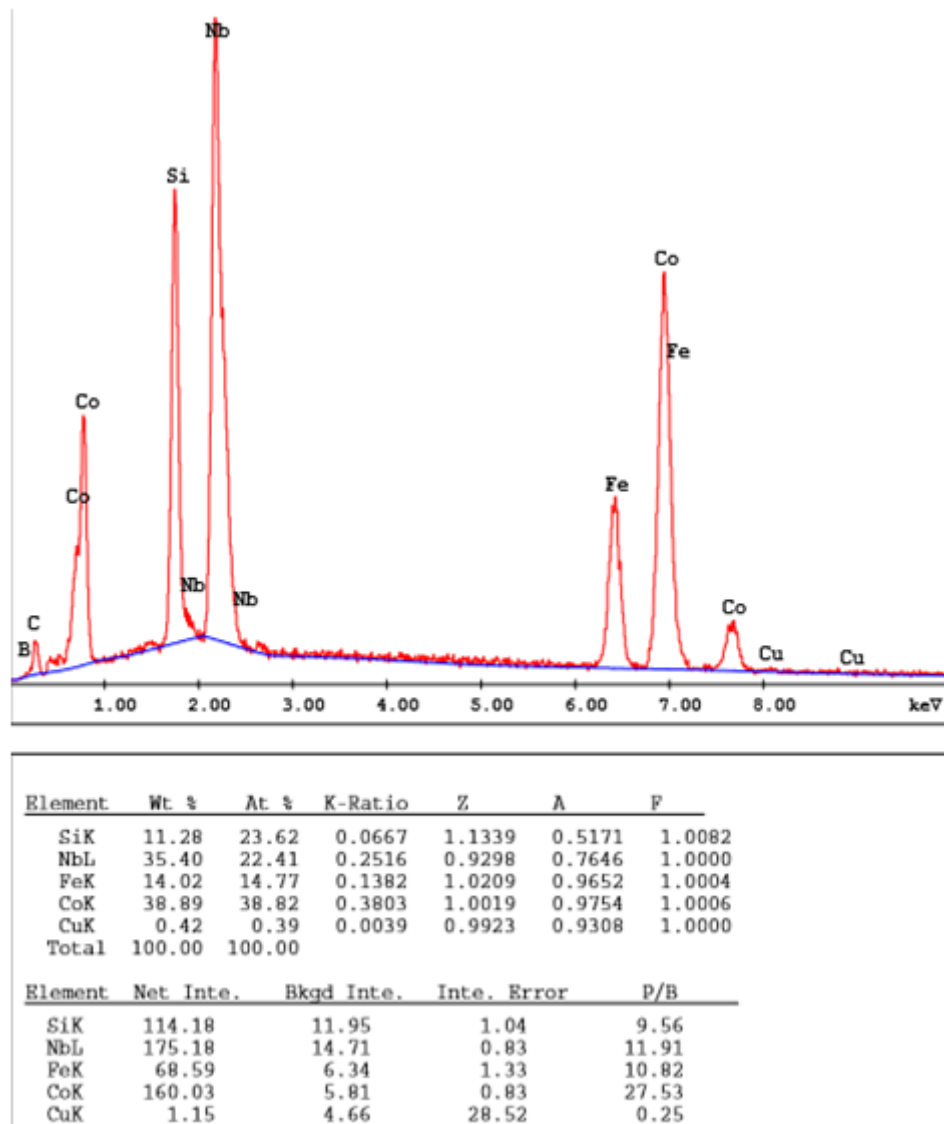


Figure A.7 EDS analysis of eutectics stated as gray for the head part of the bulk amorphous $(\text{Fe}_{36}\text{Co}_{36}\text{B}_{19.2}\text{Si}_{4.8}\text{Nb}_4)_{99.25}\text{Cu}_{0.75}$ alloy.

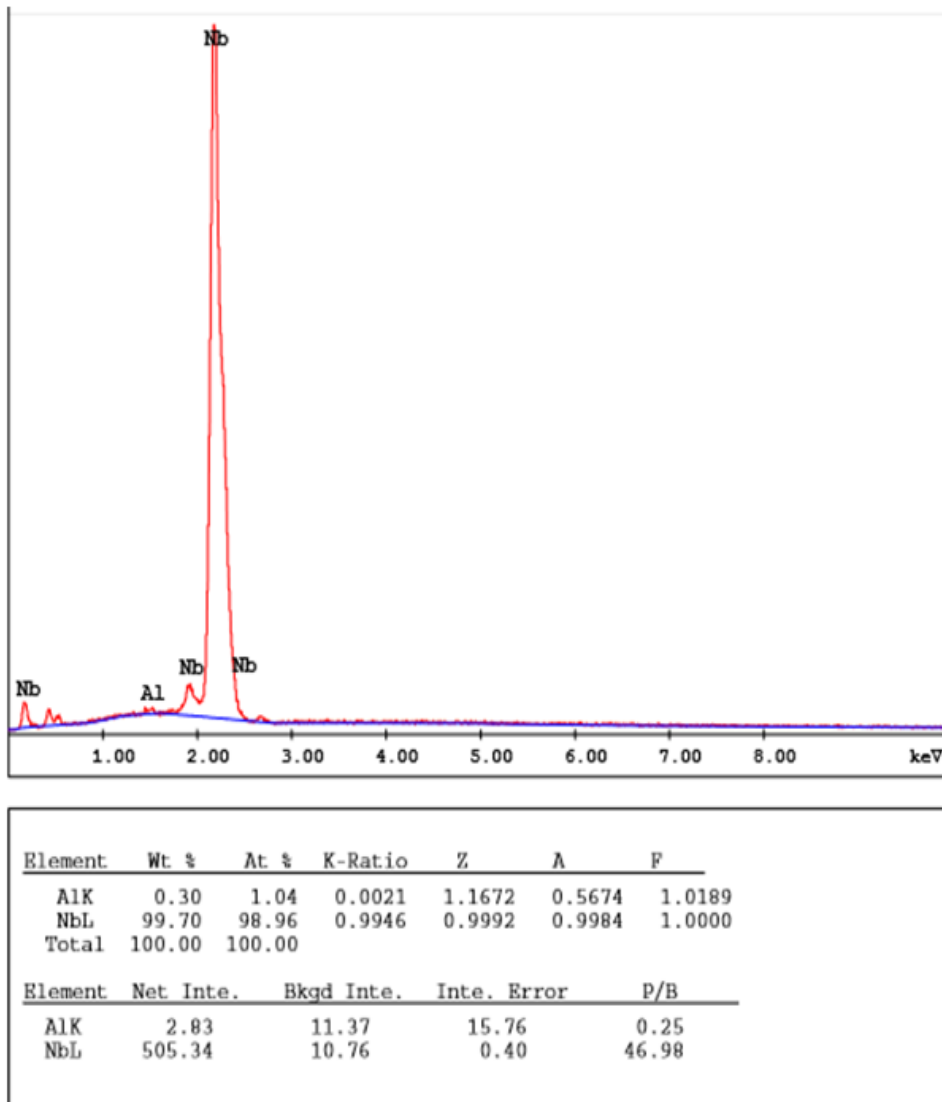
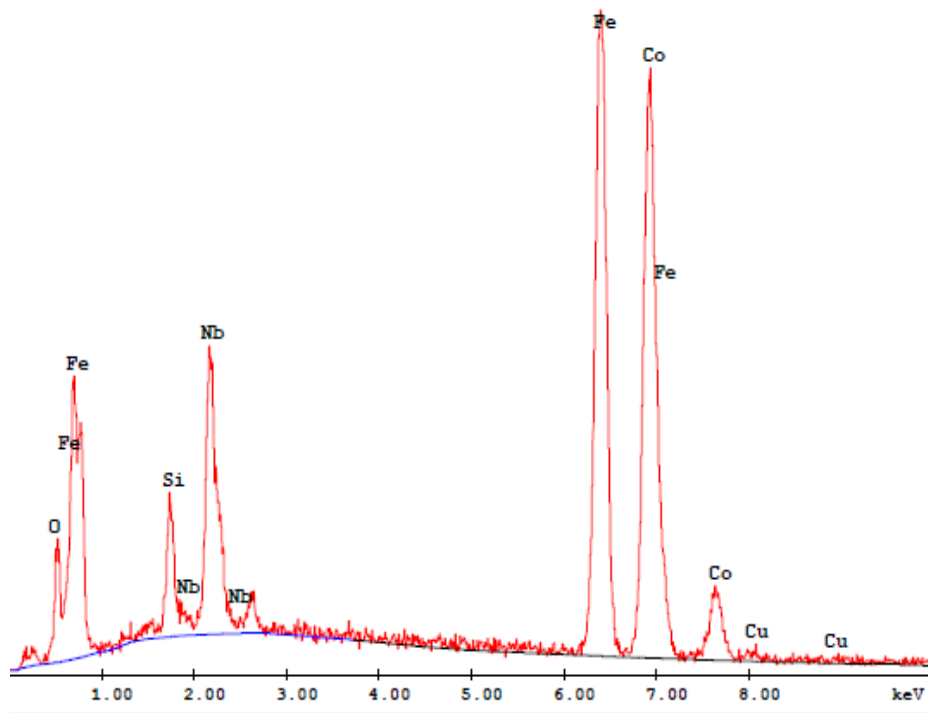


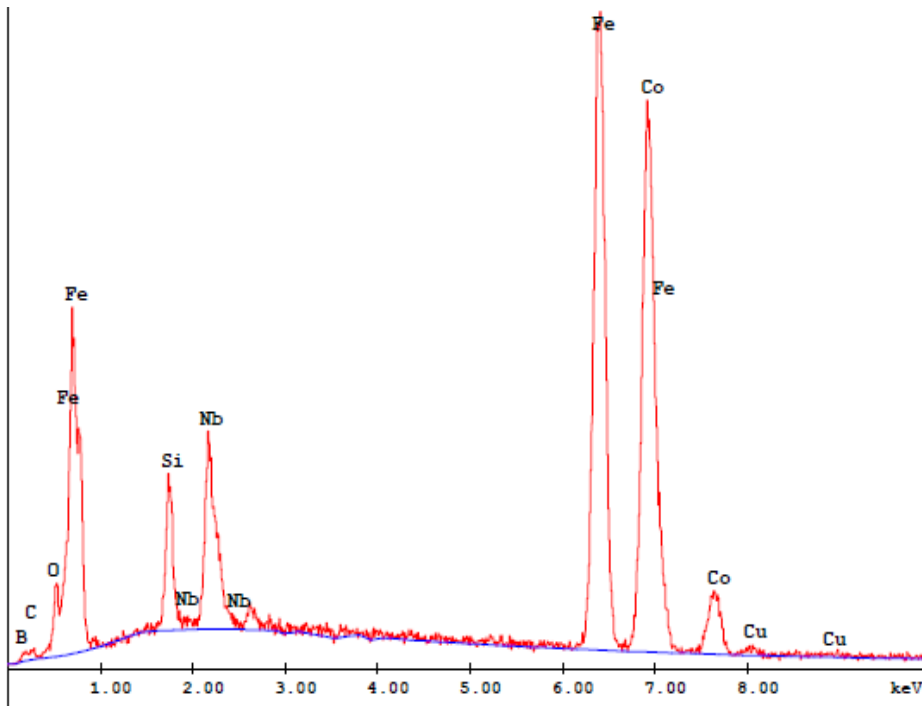
Figure A.8 EDS analysis of white region in both dendrites and eutectics for the head part of the bulk amorphous $(\text{Fe}_{36}\text{Co}_{36}\text{B}_{19.2}\text{Si}_{4.8}\text{Nb}_4)_{99.25}\text{Cu}_{0.75}$ alloy.



Element	Wt %	At %	K-Ratio	Z	A	F
SiK	3.36	7.01	0.0154	1.1299	0.4034	1.0034
NbL	13.93	8.77	0.0916	0.9241	0.7117	1.0000
FeK	39.74	41.64	0.3970	1.0151	0.9829	1.0011
CoK	41.75	41.46	0.4123	0.9959	0.9899	1.0016
CuK	1.21	1.12	0.0108	0.9857	0.8986	1.0000
Total	100.00	100.00				

Element	Net Inte.	Bkgd Inte.	Inte. Error	P/B
SiK	40.31	12.18	3.04	3.31
NbL	95.50	14.54	1.78	6.57
FeK	308.18	8.52	0.89	36.17
CoK	271.55	7.34	0.95	37.00
CuK	4.95	5.72	12.43	0.87

Figure A.9 EDS analysis of the dendrites for $(\text{Fe}_{36}\text{Co}_{36}\text{B}_{19.2}\text{Si}_{4.8}\text{Nb}_4)_{99.25}\text{Cu}_{0.75}$ alloy annealed isothermally at 535 °C.



Element	Wt %	At %	K-Ratio	Z	A	F
SiK	3.99	8.13	0.0179	1.1261	0.3976	1.0026
NbL	9.95	6.13	0.0641	0.9202	0.7004	1.0000
FeK	42.38	43.41	0.4232	1.0110	0.9868	1.0009
CoK	42.68	41.43	0.4208	0.9918	0.9930	1.0013
CuK	1.00	0.90	0.0088	0.9814	0.8962	1.0000
Total	100.00	100.00				

Element	Net Inte.	Bkgd Inte.	Inte. Error	P/B
SiK	47.13	13.48	2.38	3.50
NbL	67.08	15.30	1.92	4.38
FeK	329.59	9.27	0.74	35.57
CoK	278.08	7.99	0.80	34.80
CuK	4.06	6.17	13.00	0.66

Figure A.10 EDS analysis of the surroundings of the dendrites for $(\text{Fe}_{36}\text{Co}_{36}\text{B}_{19.2}\text{Si}_{4.8}\text{Nb}_4)_{99.25}\text{Cu}_{0.75}$ alloy annealed isothermally at 535 °C.

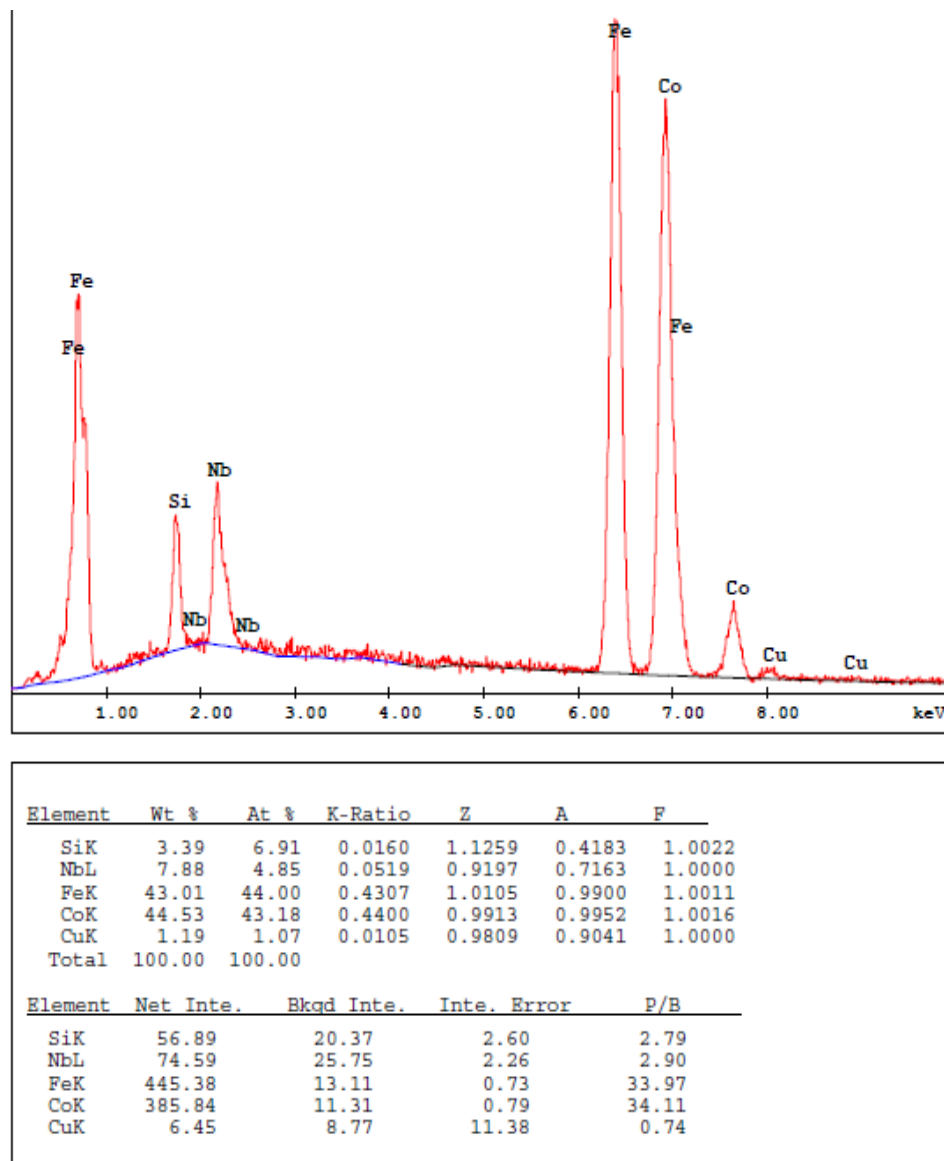
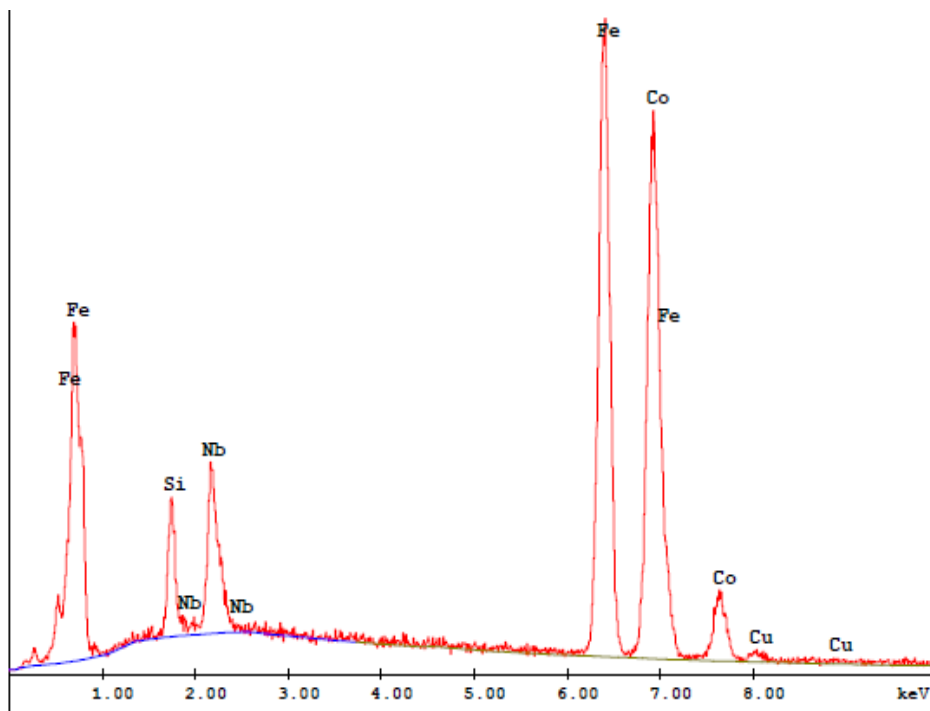


Figure A.11 EDS analysis of the dendrites for $(\text{Fe}_{36}\text{Co}_{36}\text{B}_{19.2}\text{Si}_{4.8}\text{Nb}_4)_{99.25}\text{Cu}_{0.75}$ alloy annealed isothermally at 585 °C.



Element	Wt %	At %	K-Ratio	Z	A	F
SiK	3.55	7.24	0.0169	1.1261	0.4205	1.0024
NbL	8.69	5.35	0.0574	0.9200	0.7178	1.0000
FeK	42.86	43.91	0.4291	1.0108	0.9893	1.0013
CoK	43.57	42.30	0.4305	0.9916	0.9946	1.0018
CuK	1.33	1.20	0.0118	0.9812	0.9050	1.0000
Total	100.00	100.00				

Element	Net Inte.	Bkqd Inte.	Inte. Error	P/B
SiK	59.14	17.99	2.46	3.29
NbL	81.46	21.90	2.05	3.72
FeK	438.26	11.69	0.73	37.48
CoK	372.87	9.89	0.79	37.69
CuK	7.14	7.36	9.77	0.97

Figure A.12 EDS analysis of the surroundings of the dendrites for $(\text{Fe}_{36}\text{Co}_{36}\text{B}_{19.2}\text{Si}_{4.8}\text{Nb}_4)_{99.25}\text{Cu}_{0.75}$ alloy annealed isothermally at 585 °C.

APPENDIX B

PHASE DIAGRAMS

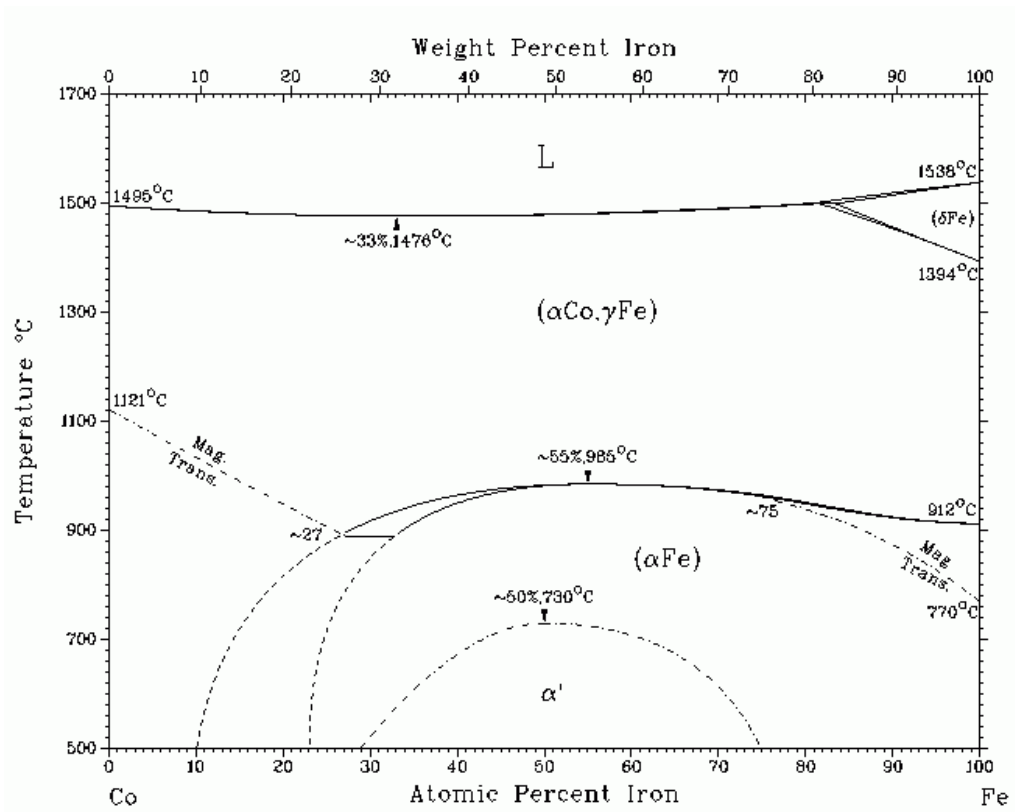


Figure B.1 Co-Fe Phase Diagram [99].

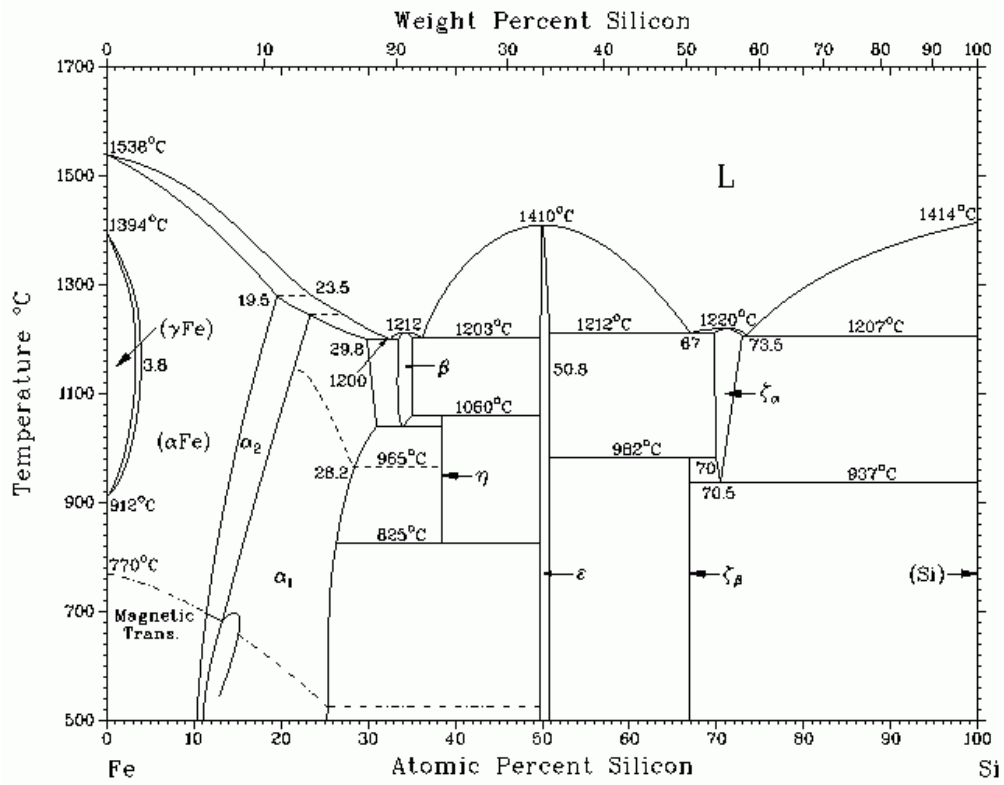


Figure B.2 Fe-Si Phase Diagram [99].

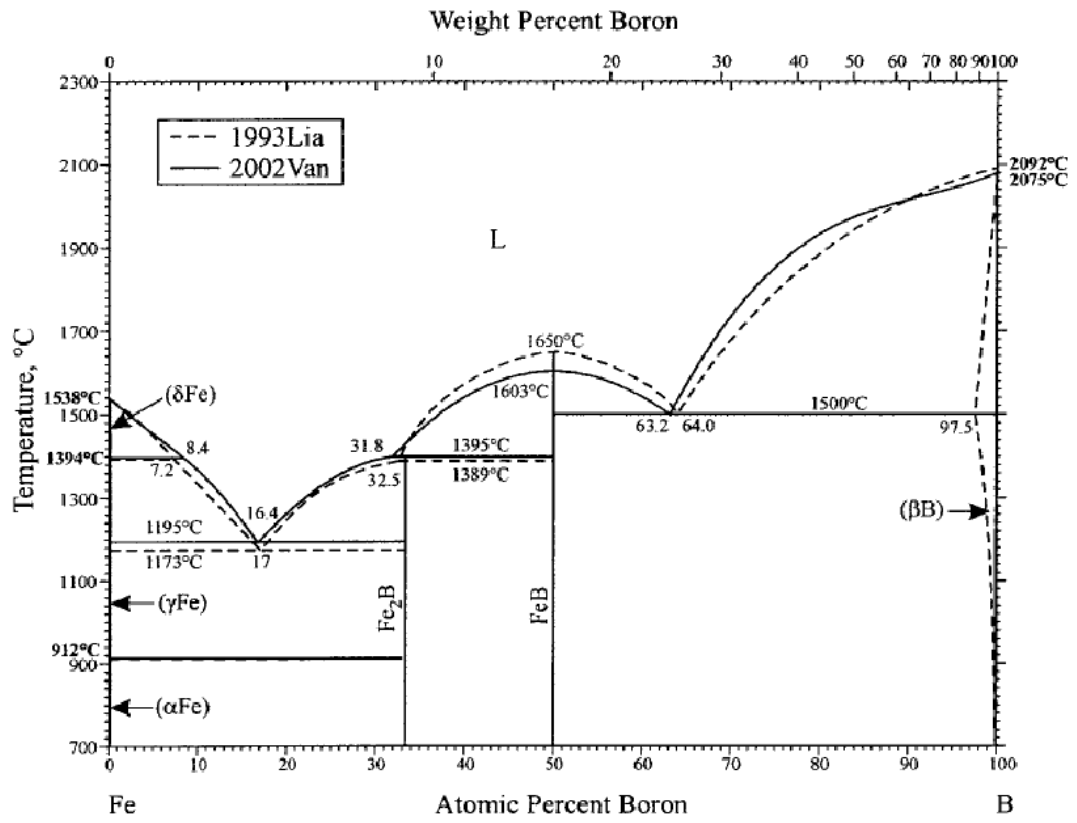


Figure B.3 Fe-B Phase Diagram [100].

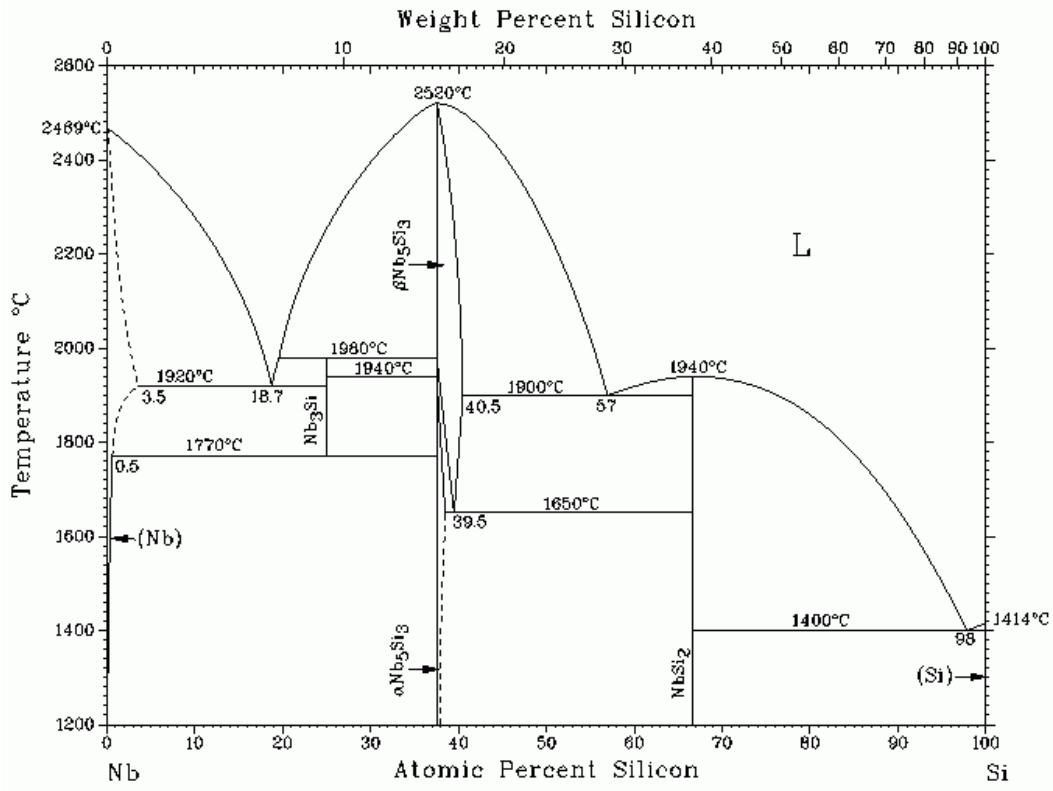


Figure B.4 Nb-Si Phase Diagram [99].

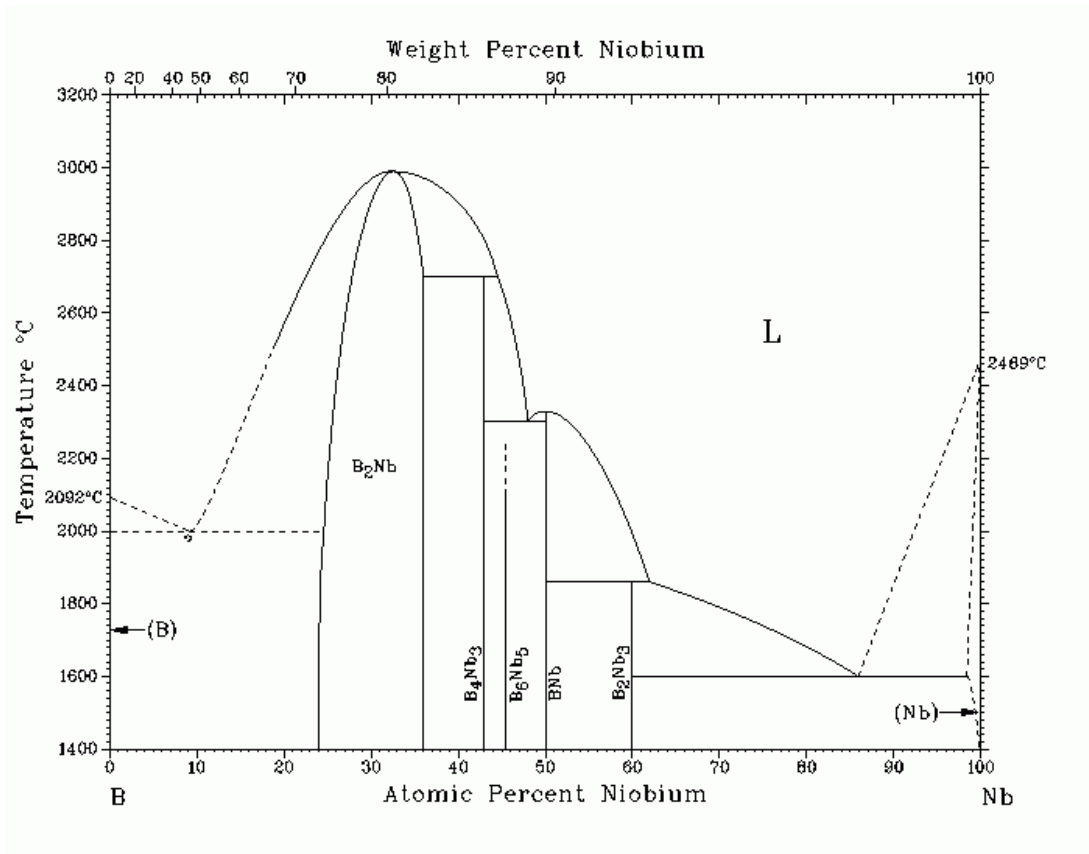


Figure B.5 B-Nb Phase Diagram [99].

APPENDIX C

OPTICAL MICROSCOPE IMAGES



Figure C.1 Optic microscope image of the $(\text{Fe}_{36}\text{Co}_{36}\text{B}_{19.2}\text{Si}_{4.8}\text{Nb}_4)_{99.25}\text{Cu}_{0.75}$ alloy annealed isothermally at 535 °C.

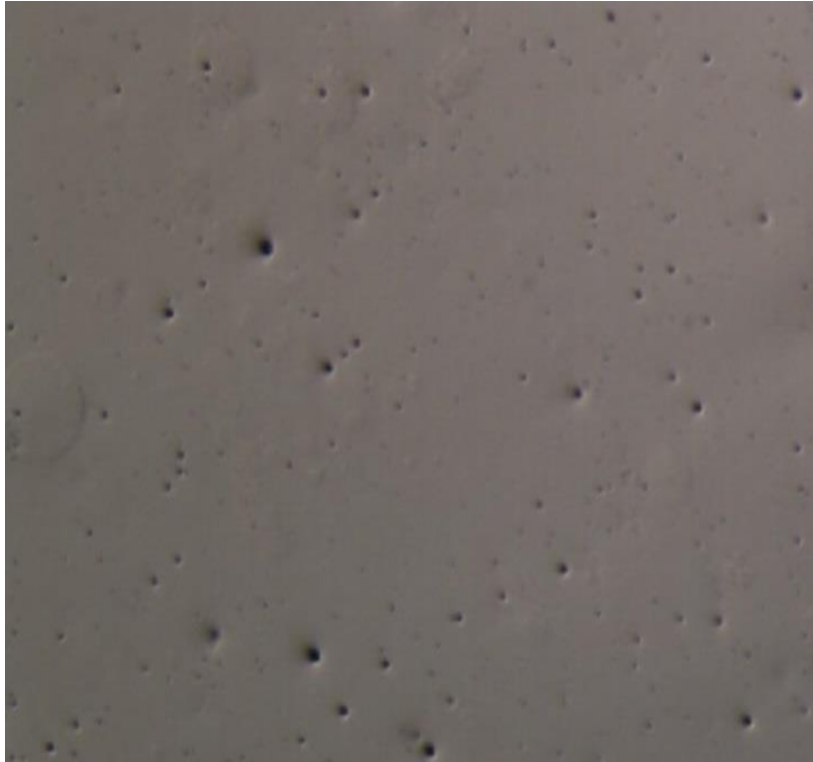


Figure C.2 Optic microscope image of the $(\text{Fe}_{36}\text{Co}_{36}\text{B}_{19.2}\text{Si}_{4.8}\text{Nb}_4)_{99.25}\text{Cu}_{0.75}$ alloy annealed isothermally at 585 °C.

APPENDIX D

SEM IMAGES AND MAPPING MICROGRAPHS

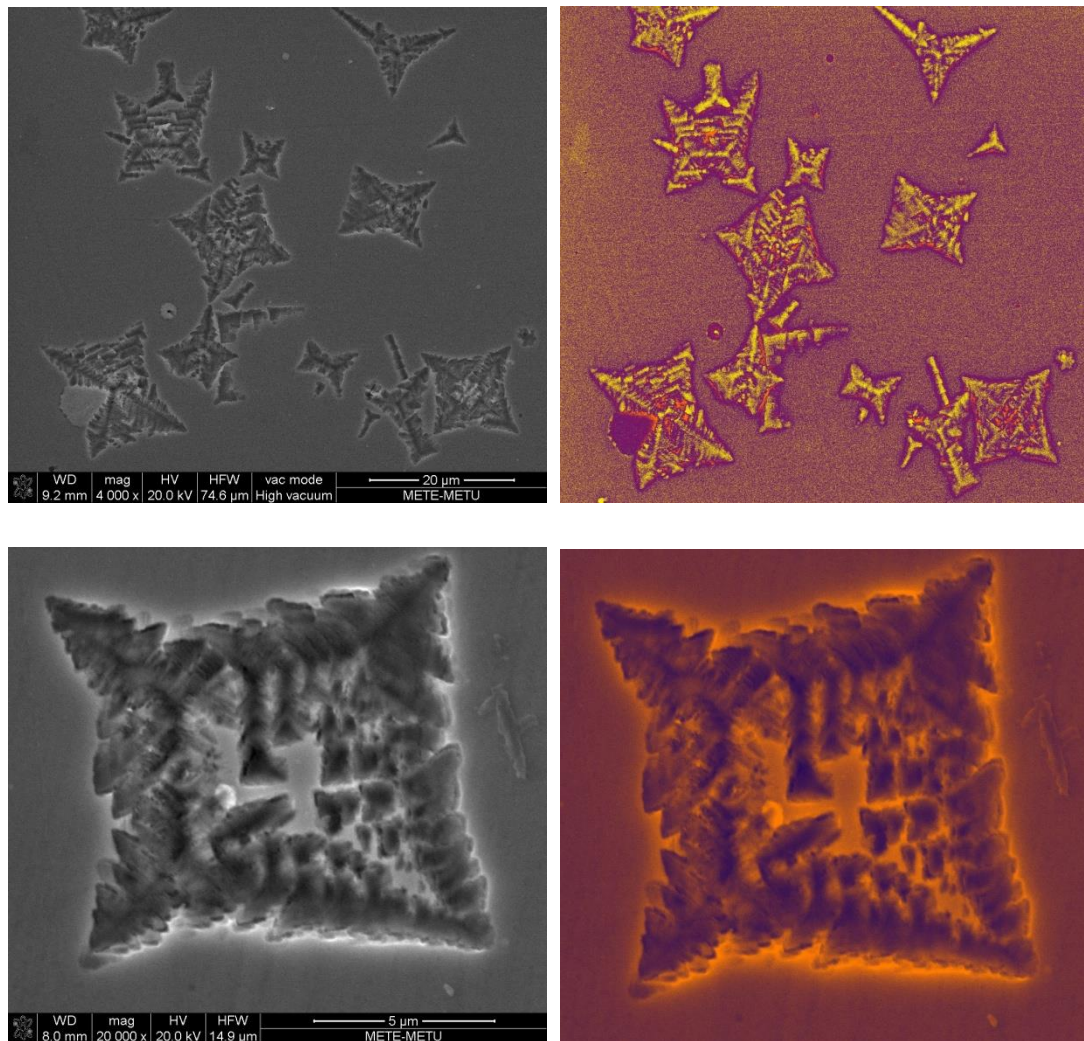


Figure D.1 SEM images and mapping micrographs of the annealed $(\text{Fe}_{36}\text{Co}_{36}\text{B}_{19.2}\text{Si}_{4.8}\text{Nb}_4)_{99.25}\text{Cu}_{0.75}$ alloy at 535 °C.

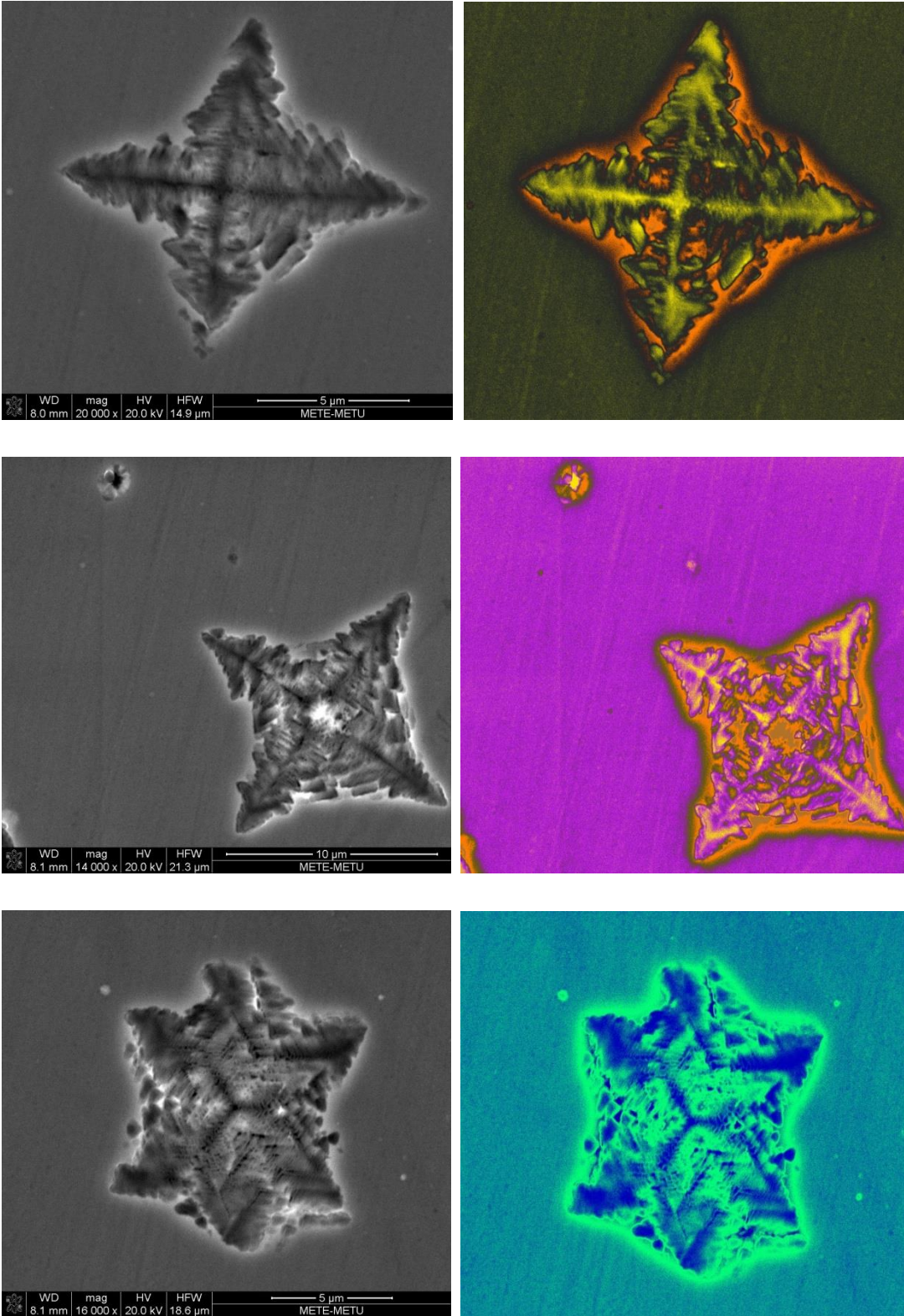


Figure D.2 SEM images and mapping micrographs of the annealed $(\text{Fe}_{36}\text{Co}_{36}\text{B}_{19.2}\text{Si}_{4.8}\text{Nb}_4)_{99.25}\text{Cu}_{0.75}$ alloy at $535\text{ }^\circ\text{C}$.

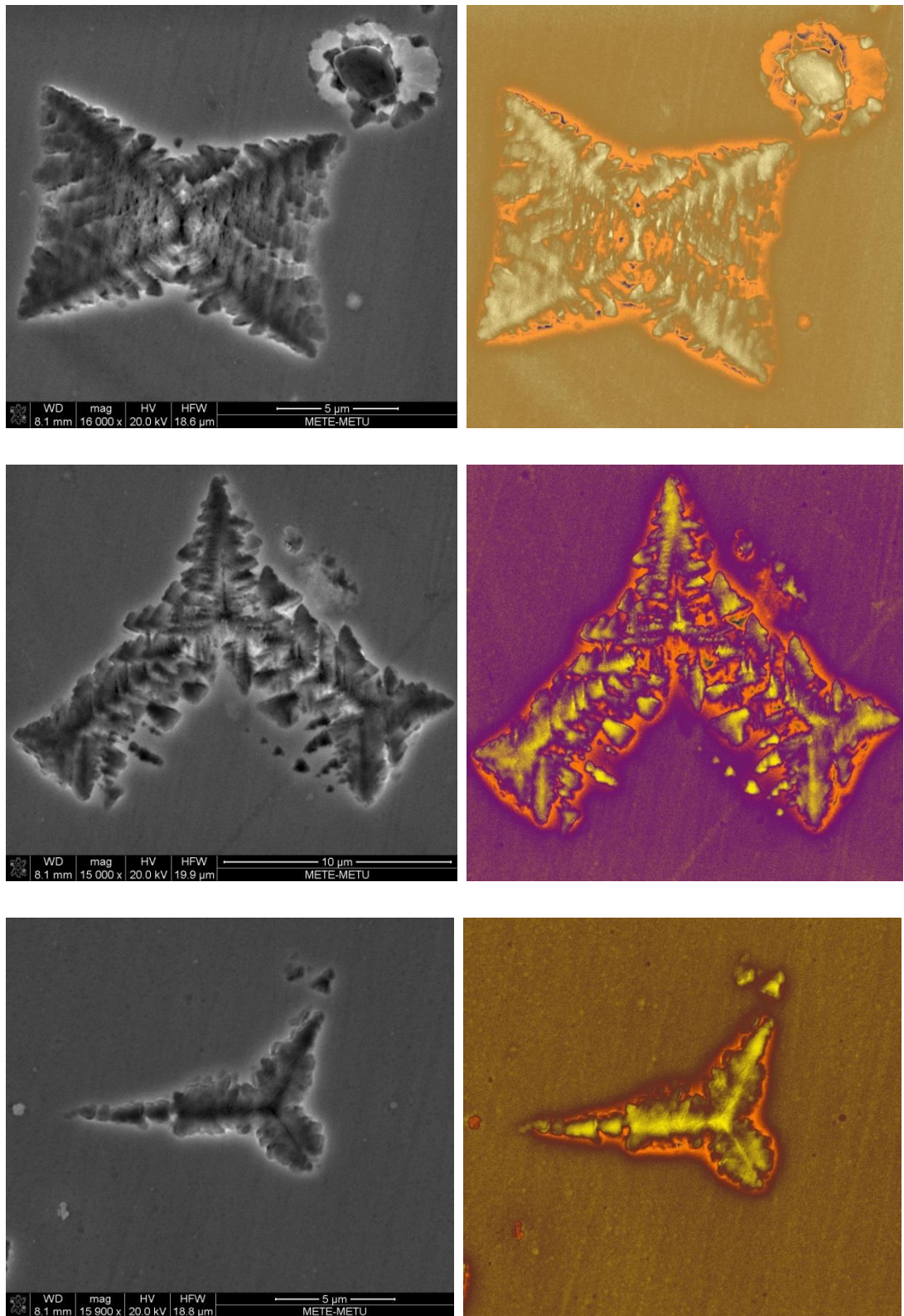


Figure D.3 SEM images and mapping micrographs of the annealed $(\text{Fe}_{36}\text{Co}_{36}\text{B}_{19.2}\text{Si}_{4.8}\text{Nb}_4)_{99.25}\text{Cu}_{0.75}$ alloy at $535\text{ }^\circ\text{C}$.

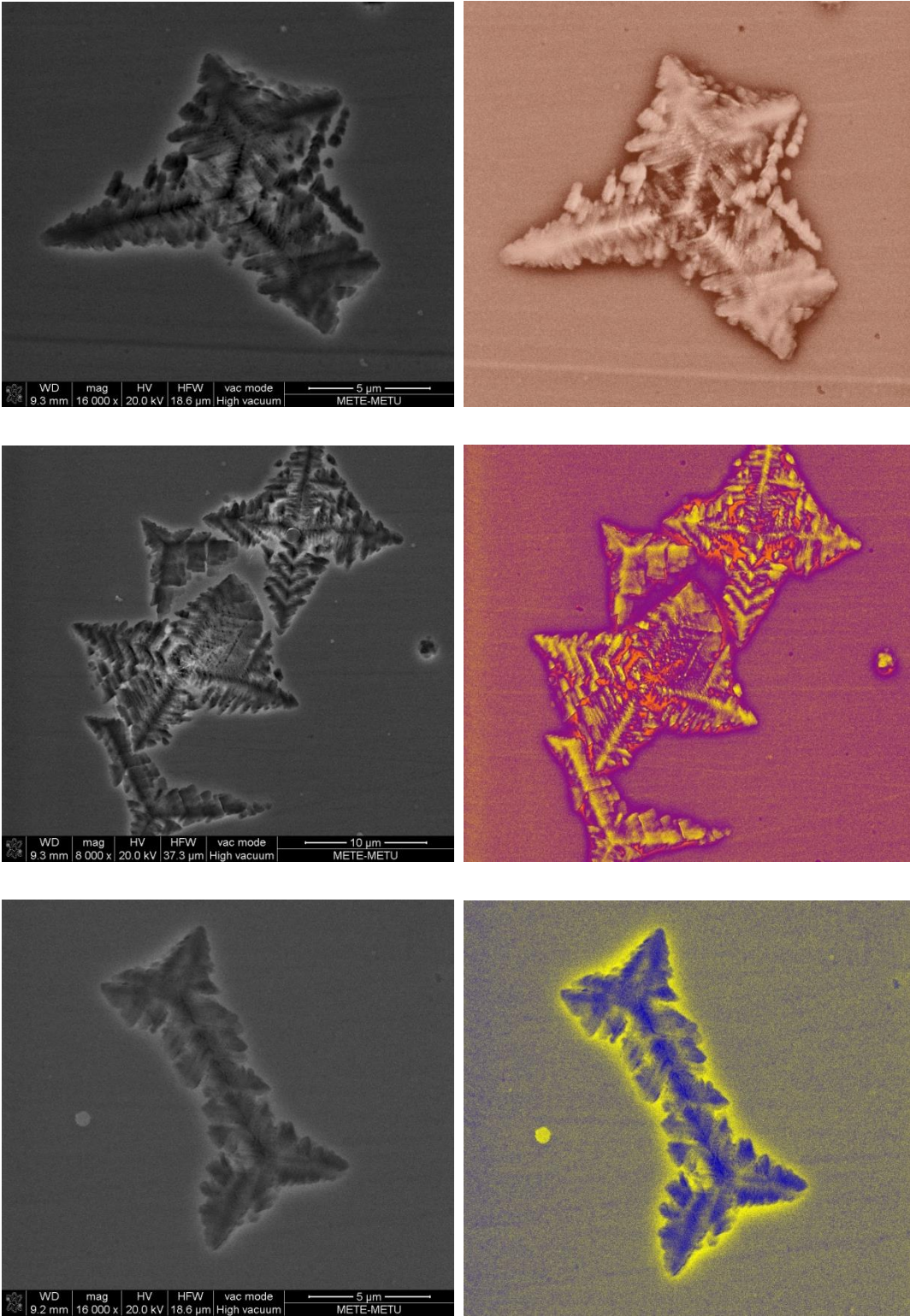


Figure D.4 SEM images and mapping micrographs of the annealed $(\text{Fe}_{36}\text{Co}_{36}\text{B}_{19.2}\text{Si}_{4.8}\text{Nb}_4)_{99.25}\text{Cu}_{0.75}$ alloy at 535 °C.

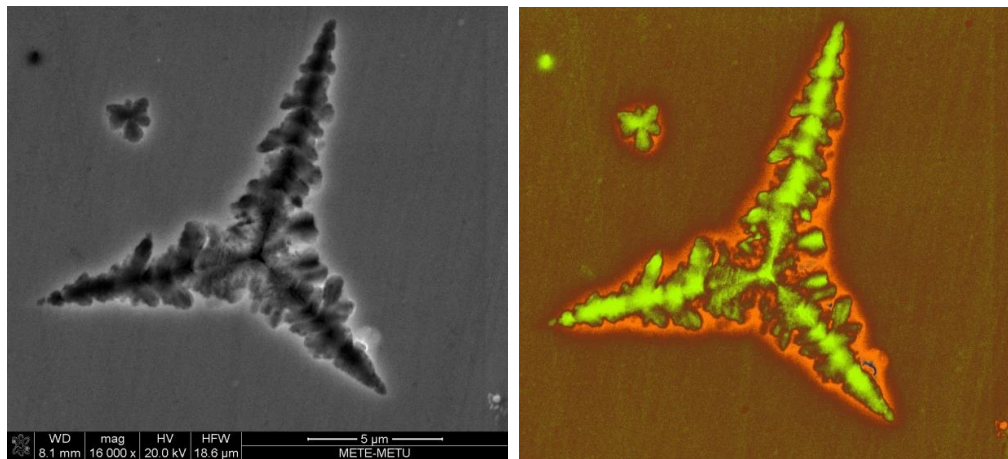


Figure D.5 SEM images and mapping micrographs of the annealed $(\text{Fe}_{36}\text{Co}_{36}\text{B}_{19.2}\text{Si}_{4.8}\text{Nb}_4)_{99.25}\text{Cu}_{0.75}$ alloy at 535 °C.

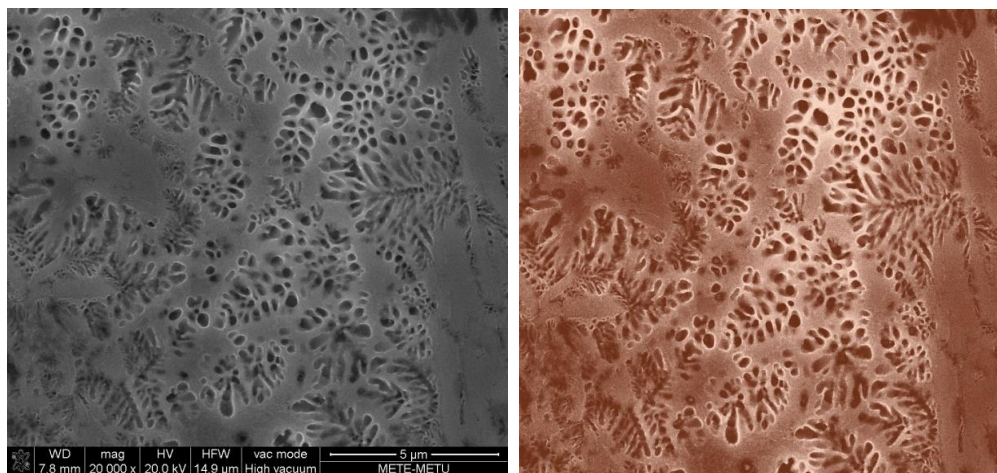
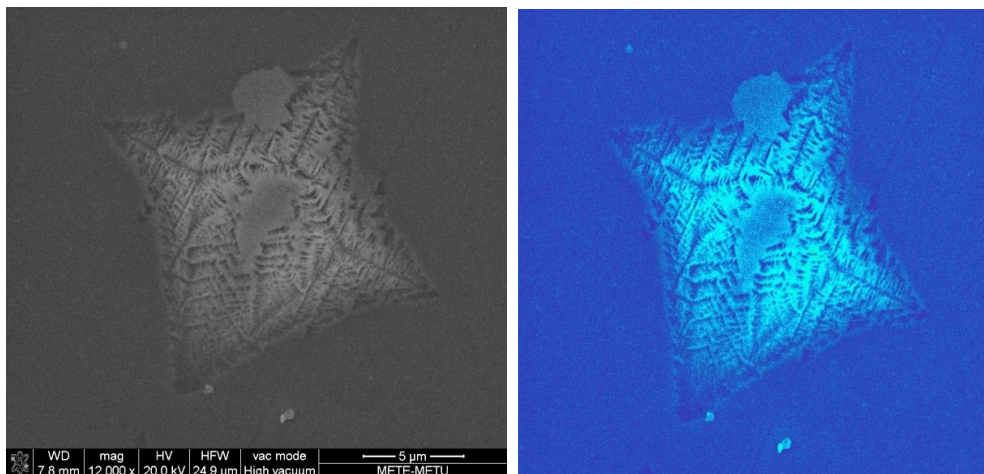


Figure D.6 SEM images and mapping micrographs of the annealed $(\text{Fe}_{36}\text{Co}_{36}\text{B}_{19.2}\text{Si}_{4.8}\text{Nb}_4)_{99.25}\text{Cu}_{0.75}$ alloy at 585 °C.

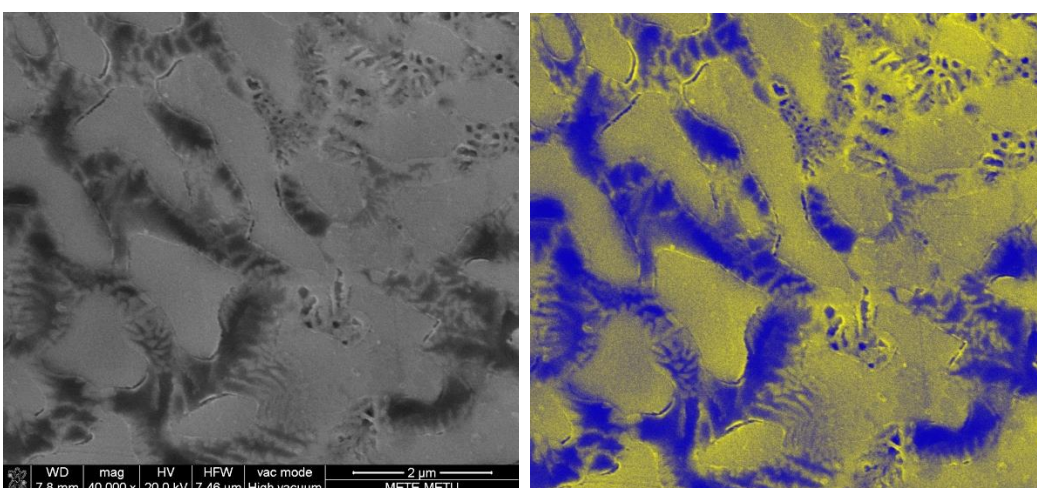
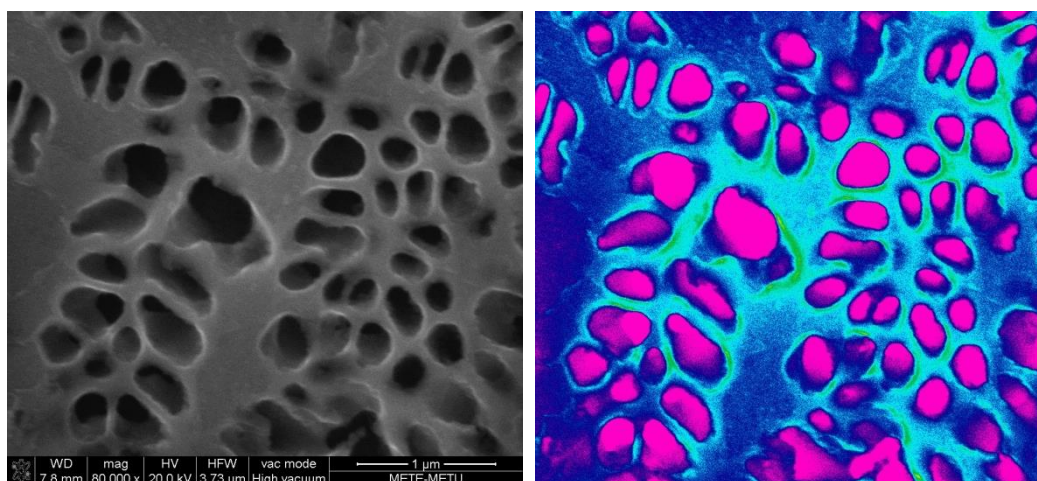
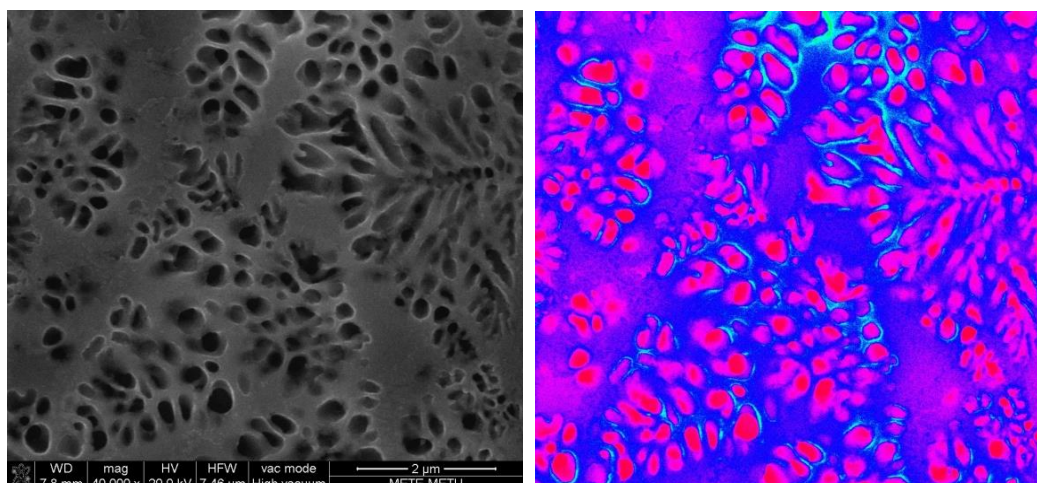


Figure D.7 SEM images and mapping micrographs of the annealed $(\text{Fe}_{36}\text{Co}_{36}\text{B}_{19.2}\text{Si}_{4.8}\text{Nb}_4)_{99.25}\text{Cu}_{0.75}$ alloy at 585 °C.

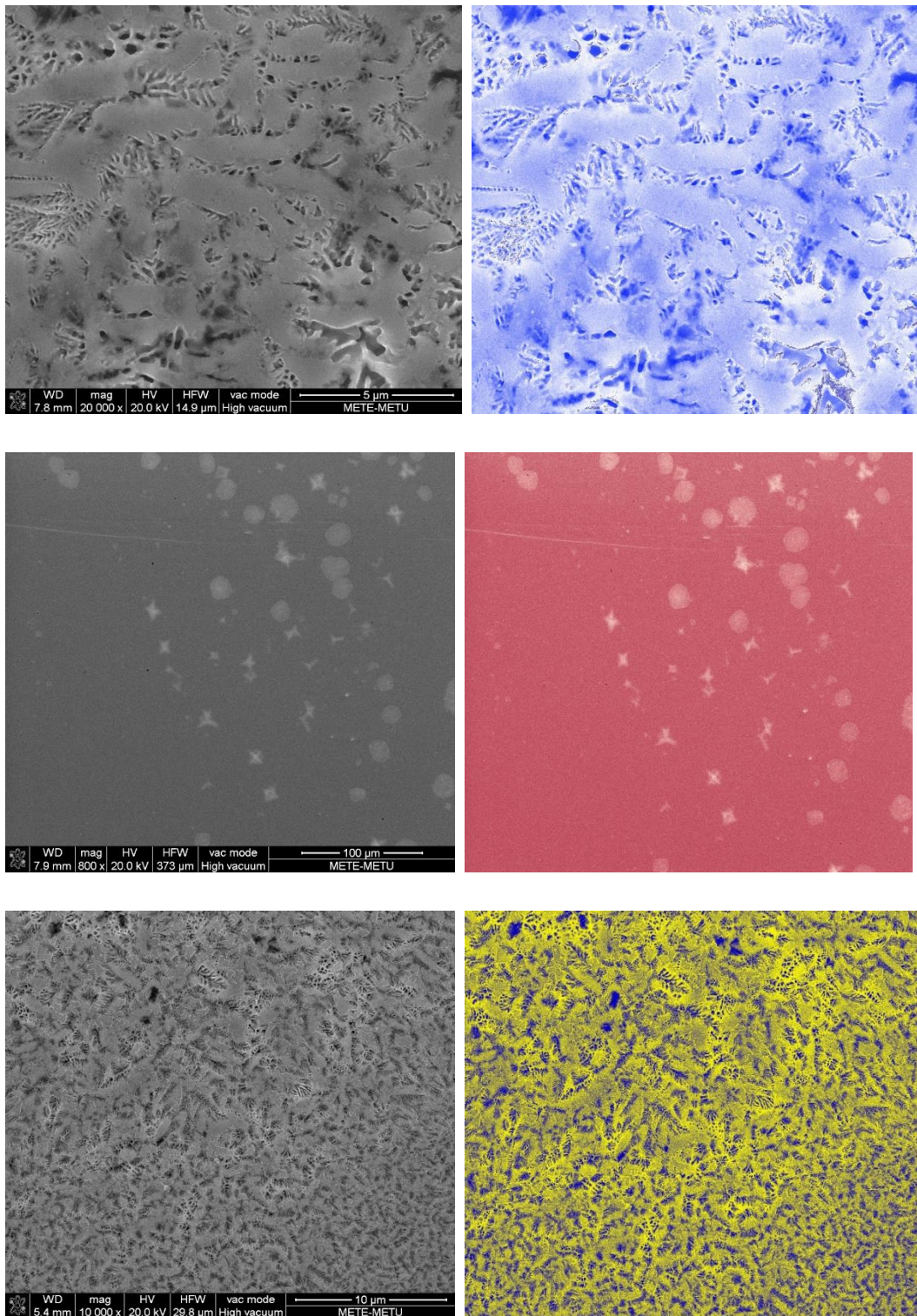


Figure D.8 SEM images and mapping micrographs of the annealed $(\text{Fe}_{36}\text{Co}_{36}\text{B}_{19.2}\text{Si}_{4.8}\text{Nb}_4)_{99.25}\text{Cu}_{0.75}$ alloy at 585 °C.

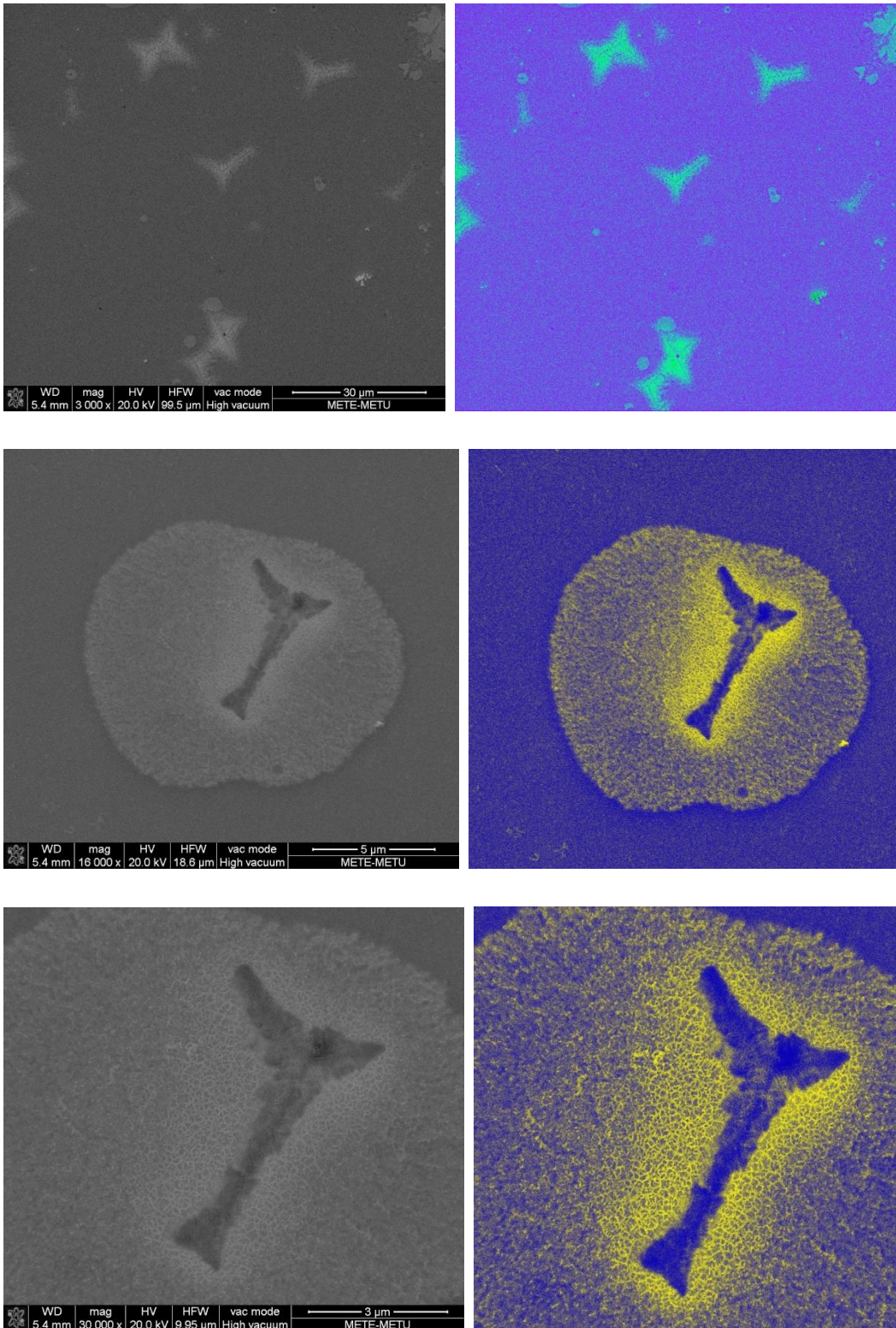


Figure D.9 SEM images and mapping micrographs of the annealed $(\text{Fe}_{36}\text{Co}_{36}\text{B}_{19.2}\text{Si}_{14.8}\text{Nb}_4)_{99.25}\text{Cu}_{0.75}$ alloy at 585 °C.

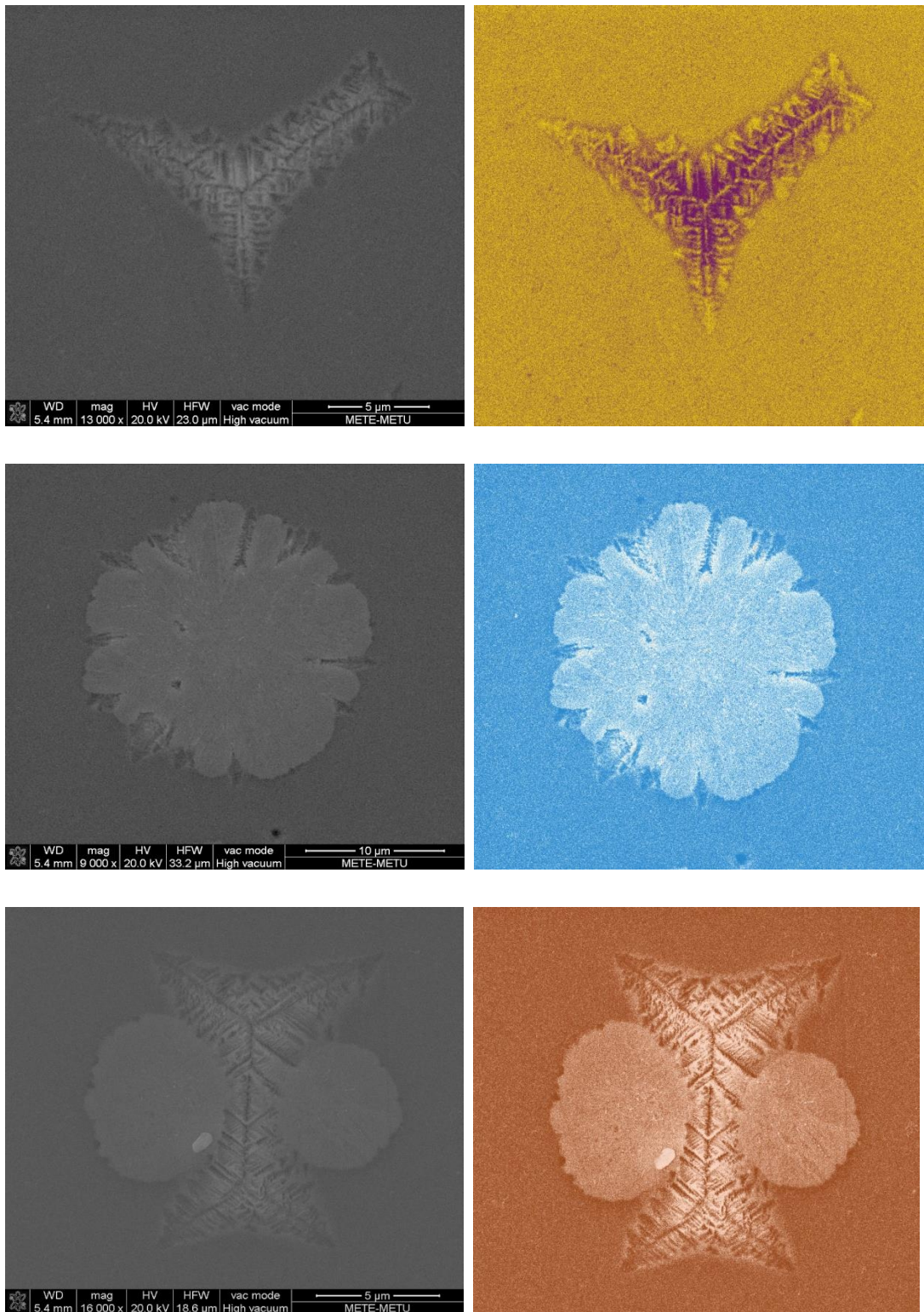


Figure D.10 SEM images and mapping micrographs of the annealed $(\text{Fe}_{36}\text{Co}_{36}\text{B}_{19.2}\text{Si}_{4.8}\text{Nb}_4)_{99.25}\text{Cu}_{0.75}$ alloy at 585 °C.

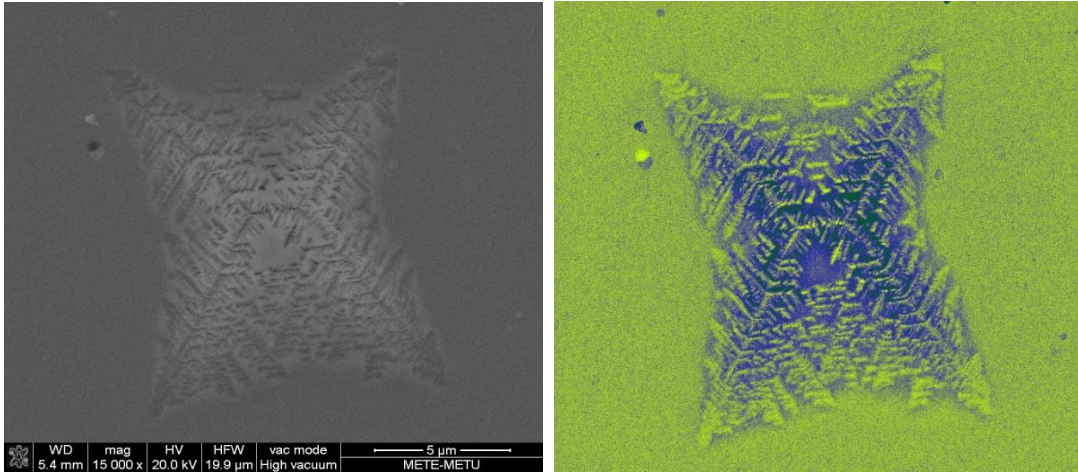


Figure D.11 SEM images and mapping micrographs of the annealed $(\text{Fe}_{36}\text{Co}_{36}\text{B}_{19.2}\text{Si}_{4.8}\text{Nb}_4)_{99.25}\text{Cu}_{0.75}$ alloy at 585 °C.